

REGULATING STIMULUS RESPONSES OF FUNCTIONAL MATERIALS

by

Hamilton Lee



APPROVED BY SUPERVISORY COMMITTEE:

Jeremiah J. Gassensmith, Chair

Paul Pantano

Ronald A. Smaldone

Mihaela C. Stefan

Copyright 2019

Hamilton Lee

All Rights Reserved

DIMITTE MIHI, QUONIAM EGO ASCENDI. EGO AMPLIUS NON TETIGIT PER LUCEM,
AUT TENEBRIS.

REGULATING STIMULUS RESPONSES OF FUNCTIONAL MATERIALS

by

HAMILTON LEE, BS

DISSERTATION

Presented to the Faculty of

The University of Texas at Dallas

in Partial Fulfillment

of the Requirements

for the Degree of

DOCTOR OF PHILOSOPHY IN

CHEMISTRY

THE UNIVERSITY OF TEXAS AT DALLAS

August 2019

ACKNOWLEDGMENTS

Often lauded are the heroes of science, philosophy, and the arts. They need not be named here for they linger among the minds of many and the throes of history. But while they accomplished what many could not, understanding key aspects of this physical world and building civilization as we know it today—sometimes in the face of great doubt and persecution—they did not do so alone. They could not do so alone. I do not consider myself a hero by any means, but I have accomplished something concrete during my short existence and I did not do so alone. There were many who helped me along my pursuit to understand myself and the world around me, a pursuit that continues in the present and will continue in any future I can imagine. Listed below are the names of those whom I have had the great fortune of encountering and to whom I owe the very opportunity to write these words:

Ahn, Jung-Mo (Expertise); Batchelor, Benjamin (Expertise); Benjamin, Candace (O.G. Crew, Bootleg, I am the actual No. 5!); Berry, Danielle (Perspectives); Bleris, Leonidas (Expertise); Brohlin, Olivia (Spice=bad); Castaneda, Maria (Expertise); Castro, Fabian (Juggernaut spawn); Chan, Julia (Origins); Chapman, Cody and Cullen (Kindness, Shelter); Chen, Zhuo (Foundations, Deadpan);

Coffer, Jeff and Mary (Kindness, Shelter); Coffer, Matthew and Michael (Kindness, Shelter); Coffer, Meagan (Love, Chicken tenders); D'Arcy, Sheena (Expertise); Dent, Lakeisha (Perspectives); Dharmarwardana, Madushani (Foundations, Tacos); Douthey, Mark (Charity); Faisal, Tahmid (Growth); Firouzi, Hamid (Hyper); Gassensmith, Jeremiah (The BEST, Perseverance); Gassensmith, Katie (Guard);

Green, Lance (Perspectives); Hoang, David (Charity); Jackson, Emily (Expertise); Kang, Peiyuan (Alvin) (Expertise); Kassees, Kara (Charity); Layne, Winston (Expertise); Lee, Harrison (Bruh); Lee, Jiyong (Charity); Lewis, Kelli (Expertise); Li, Shaobo (Foundations, Detergents); Lumata, Jenica (U [Joules]); Lumata, Lloyd (Expertise); Luzuriaga, Michael (O.G. Crew, Positive cynicism); Maldonado, Betty (Iron Man); McDonald, George (Kinko's Ultra); Murray, Kyle (Plat, Rock); Nguyen, Hien (SOS); Nielsen, Steven (Open ears, Models); Nowak, Chance (Do the brew); Ong, Whitney (Charity); Pantano, Paul (System importance); Papadimitratos, Alexios (Expertise); Parish, Christopher (Expertise); Payne, Ethan (Life, Logic); Shahrivarkevishahi, Arezoo (Bigger picture, Tangled system); Silva, Alejandra (Charity); Smaldone, Ron (Hand-waving=danger); Smith, Tristan (Charity); Sra, Amandeep (Finals be precious); Stefan, Mihaela (Open ears, Cats); Sternod, Jacob (Bruh); Thompson, Christina (Synthesis consultant); Tuong, Lana (Life, #008000); Urbach, Adam (Origins); Welch, Raymond (Foundations, Mech).

June 2019

REGULATING STIMULUS RESPONSES OF FUNCTIONAL MATERIALS

Hamilton Lee, PhD
The University of Texas at Dallas, 2019

Supervising Professor: Jeremiah J. Gassensmith

Functional materials are materials that are responsive to external stimuli. They appear in natural and synthetic forms and are crucial to the operation of many physical, chemical, and biological systems. An improved understanding and ability to regulate the stimulus responses of functional materials would unleash many insights on the development of novel functional materials and the optimization and application of existing ones. Materials responding to changes in pH and redox conditions are of particular interest to clinical applications owing to the ubiquity with which pH and redox regulation is found in biological systems. We report the development of a pH-responsive virus-like particle (VLP) to better understand the mechanisms behind cellular uptake. The uptake of this pH-responsive VLP by certain cell lines is inhibited by the presence of terminal carboxylic acid moieties attached onto the surface of the VLP. Exposure of the VLP to acidic conditions causes hydrolysis of a linker between the carboxylic acid moieties and the VLP, releasing the carboxylic acid moieties and allowing uptake of the VLP by cells. We also report the development of aminoxyl-based ORCAs for MRI that are able to resist reduction by ascorbate. These ORCAs rely on a macrocycle to encage the aminoxyl radical, shielding the radical from reduction by ascorbate while still allowing the H₂O exchange necessary for contrast enhancement. The

optimization of these aminoxyl-based ORCAs may someday lead to ORCA designs that can replace gadolinium and other metal-based contrast agents that currently find mainstream clinical usage.

TABLE OF CONTENTS

ACKNOWLEDGMENTS	v
ABSTRACT.....	vii
LIST OF FIGURES	xi
LIST OF TABLES	xv
CHAPTER 1 INTRODUCTION	1
1.1 Introduction to Regulating Stimulus Responses of Functional Materials	1
1.2 pH-Responsive Materials.....	2
1.3 Redox-Responsive Materials	4
1.4 Virus-Like Particles and Viral Nanoparticles	8
1.5 Summary	11
CHAPTER 2 REGULATING THE UPTAKE OF VIRAL NANOPARTICLES IN MACROPHAGE AND CANCER CELLS VIA A PH SWITCH.....	12
2.1 Introduction.....	13
2.2 Results and Discussion	15
2.3 Conclusions.....	26
CHAPTER 3 ENHANCING THE SURVIVABILITY OF AMINOXYL ORCAS VIA SHIELDING WITH CUCURBIT[8]URIL.....	27
3.1 Introduction.....	27
3.2 Results and Discussion	30
3.3 Conclusions.....	44
CHAPTER 4 PERSISTENT AMINOXYL ORCAS UTILIZING A ROTAXANE ARCHITECTURE FOR SHIELDING	45
4.1 Introduction.....	45
4.2 Results and Discussion	47
4.3 Conclusions.....	50
CHAPTER 5 SUMMARY OF FINDINGS AND FUTURE DIRECTIONS	51
5.1 SUMMARY OF FINDINGS	51

5.2 FUTURE DIRECTIONS	52
APPENDIX A SUPPORTING INFORMATION FOR CHAPTER 2	53
APPENDIX B SUPPORTING INFORMATION FOR CHAPTER 3	82
APPENDIX C SUPPORTING INFORMATION FOR CHAPTER 4	96
REFERENCES	103
BIOGRAPHICAL SKETCH	116
CURRICULUM VITAE	117

LIST OF FIGURES

Figure 1.1. Examples of pH-responsive functional groups.....	2
Figure 1.2. Examples of redox-responsive functional groups.	5
Figure 1.3. The oxidized and reduced forms of aminoxyl radicals.	6
Figure 1.4. Crystallographically obtained structures of common VLPs Q β , MS2, Cowpea Mosaic Virus (CPMV), Cowpea Chlorotic Mosaic Virus (CCMV), and Tobacco Mosaic Virus (TMV). TMV is not illustrated to scale.....	9
Figure 2.1. (A) Structure of Q β^a and (B) Synthesis of Both Conjugates Q β -6X and Q β -Trim ^b	16
Figure 2.2. (A) TEM image of Q β -6X. (B) Native agarose gel electrophoresis of Q β , Q β -6X, and Q β -Trim. The greater mobility toward the positive electrode (bottom) suggests an increase in negative charge. (C) Dynamic light scattering data of Q β -6X. (D) MALDI-TOF mass spectra of Q β and Q β -6X showing observed masses. ESI-TOF mass spectrum of Q β -Trim showing one, two, and three functionalized residues per coat protein.....	18
Figure 2.3. Representative histogram from flow cytometry studies corresponding to RAW 264.7 macrophages incubated with their respective Q $\beta_{(GFP)}$ samples at 40 μ M. All cells were incubated with the Q β conjugates for 4 h at 37 $^{\circ}$ C.....	19
Figure 2.4. Synthesis of Q β -Z Conjugates ^a	20
Figure 2.5. (A) TEM micrograph of the Q $\beta_{(GFP)}$ -ZX conjugate. (B) Native agarose gel electrophoresis showing Q β , Q β conjugates, and the hydrolyzed product Q β -ZX-Hyd. (C) DLS measurement of the Q $\beta_{(GFP)}$ -ZX conjugate showing a uniform size distribution.	21
Figure 2.6. (A) Q β -ZFITC was used for the kinetics studies. (B) Release profiles of FITC from Q β -ZFITC at pH 7.4 (KP buffer, 0.1 M, 25 $^{\circ}$ C), pH 6.0 (MES buffer, 0.1 M, 25 $^{\circ}$ C), and pH 5.0 (MES buffer, 0.1 M, 25 $^{\circ}$ C).	22
Figure 2.7. Representative histograms from flow cytometry studies corresponding to (A) RAW 264.7 macrophages and (B) HeLa cells incubated with their respective Q β samples. Epifluorescence microscope images of (C) RAW 264.7 macrophages and (D) HeLa cells incubated with their respective Q β samples (50 μ M).	25
Figure 3.1. (A) Structure of TMV highlighting the solvent exposed amino acid residues of a single coat protein. (B) Installation of alkyne functionality on Y139 via diazonium coupling followed by the conjugation of 6-HCl via CuAAC.....	31
Figure 3.2. Synthesis of 6	32

Figure 3.3. ITC data for 6 at 25 °C in 10 mM sodium phosphate (pH 7.0). 6 (250 µM) was titrated into a solution of CB[8] (50 µM).....	33
Figure 3.4. Characterization of TMV after bioconjugation reactions. (A) TEM image of TMV- 6 . (B) Bioconjugation of the TEMPO radical to TMV was confirmed via ESI-MS. The peak at 17534 m/Z corresponds to native TMV. The peak at 17662 m/Z corresponds to TMV-Aky. The peak at 17958 m/Z corresponds to TMV- 6 . The spectrum corresponding to TMV- 6 confirms complete conversion of TMV-Aky to TMV- 6 . (C) The integrity of the TMV rods after modification was confirmed by SEC. The single peak in the chromatograms (@260 nm) of the modified TMV samples demonstrates that the bioconjugation reactions did not compromise the morphology of the TMV rods. (D) X-band EPR spectra of 6 and TMV- 6	35
Figure 3.5. Fluorescence titration data for TMV- 6 . TMV- 6 (0-20 µM in terms of TEMPO) was titrated into solutions of CB[8]⊃PF (0.2 µM). The K_d value for the CB[8]⊃TMV- 6 complex was determined to be $3.8 \pm 0.5 \times 10^{-7}$ M.	39
Figure 3.6. Plots of (A) $1/T_1$ (s ⁻¹) and (B) $1/T_2$ (s ⁻¹) versus [TEMPO] (mM) for TMV- 6 and TEMPO-NH ₂ in the absence and presence of CB[8] at 43 MHz in KP buffer (0.1 M, pH 7.4) @ 310 K.....	41
Figure 3.7. EPR spectra for the reduction of TMV- 6 (2.6 mg/mL) with sodium ascorbate (10 equivalents per TEMPO moiety) in the (A) presence (10 equivalents per TEMPO moiety) and (B) absence of CB[8].	43
Figure 4.1. Synthesis of PXR	48
Figure 4.2. Synthesis of 7	49
Figure A1. ¹ H NMR spectrum of 6-azidohexanoic acid.	54
Figure A2. ¹ H NMR spectrum of 2,5-dioxopyrrolidin-1-yl 6-azidohexanoate.....	56
Figure A3. ¹ H NMR spectrum of 6-(prop-2-yn-1-yloxy)hexanoic acid.	57
Figure A4. ¹ H NMR spectrum of tris(2,5-dioxopyrrolidin-1-yl) benzene-1,3,5-tricarboxylate. ...	58
Figure A5. ¹ H NMR spectrum of 6-hydrazinonicotinic acid.	59
Figure A6. ¹ H NMR spectrum of 1-azidopropan-2-one.....	60
Figure A7. ¹ H NMR spectrum of 2,5-dioxopyrrolodin-1-yl 6-(2-(1-azidopropan-2-ylidene)hydrazinyl)nicotinate.	61
Figure A8. ¹³ C NMR spectrum of 2,5-dioxopyrrolodin-1-yl 6-(2-(1-azidopropan-2-ylidene)hydrazinyl)nicotinate.	62

Figure A9. ¹ H NMR spectrum of 5-azidopentan-2-one.	63
Figure A10. ¹ H NMR spectrum of 2,5-dioxopyrrolodin-1-yl 6-(2-(5-azidopentan-2-ylidene)hydrazinyl)nicotinate.	64
Figure A11. ¹³ C NMR spectrum of 2,5-dioxopyrrolodin-1-yl 6-(2-(5-azidopentan-2-ylidene)hydrazinyl)nicotinate.	65
Figure A12. MALDI-TOF MS spectrum of native Q β coat protein.	69
Figure A13. MALDI-TOF MS spectrum of Q β -6X coat protein.	70
Figure A14. MALDI-TOF MS spectrum of Q β -ZX coat protein.	71
Figure A15. MALDI-TOF MS spectrum of Q β -ZX2 coat protein.	72
Figure A16. ESI-TOF MS spectrum of Q β -ZX-Hyd coat protein.	73
Figure A17. ESI-TOF MS spectrum of Q β -ZX2-Hyd coat protein.	74
Figure A18. ESI-TOF MS spectrum of Q β -Trim coat protein.	75
Figure A19. TEM images of A) Native Q β , B) Q β -6X, C) Q β -ZX, D) Q β -ZX-Hyd, E) Q β -ZX2, F) Q β -ZX2-Hyd.	76
Figure A20. DLS data of A) Native Q β , B) Q β -6X, C) Q β -ZX, D) Q β -ZX-Hyd, E) Q β -ZX2, F) Q β -ZX2-Hyd, G) Q β -Trim.	77
Figure A21. Native agarose gel electrophoresis of Q β , Q β -ZX2, and Q β -ZX2-Hyd.	78
Figure A22. Epifluorescence microscope images of A) RAW 264.7 macrophages and B) HeLa cells incubated with their respective Q β samples (50 μ M). Blue: DAPI, Red: WGA-AlexaFluor 555, and Green: GFP. Scale bar represents 50 μ m.	79
Figure A23. Representative histograms from flow cytometry studies corresponding to A) RAW 264.7 macrophages and B) HeLa cells incubated with PBS buffer and Q β _(GFP)	80
Figure A24. Representative histograms from flow cytometry studies corresponding to A) RAW 264.7 macrophages and B) HeLa cells incubated with their respective Q β samples.	81
Figure B1. ¹ H NMR spectrum of imidazole-1-sulfonyl azide hydrogen sulfate.	84
Figure B2. ¹³ C NMR spectrum of imidazole-1-sulfonyl azide hydrogen sulfate.	84
Figure B3. ¹ H NMR spectrum of 2	85

Figure B4. ^1H NMR spectrum of 3	86
Figure B5. ^1H NMR spectrum of 4	87
Figure B6. ^{13}C NMR spectrum of 4	88
Figure B7. ^1H NMR spectrum of 6	90
Figure B8. ^{13}C NMR spectrum of 6	90
Figure B9. Fluorescence titration data for nTMV and CB[8]⊃PF. nTMV (0-20 μM in terms of TMV coat protein) was titrated into solutions of CB[8]⊃PF (0.2 μM).	94
Figure B10. Fluorescence titration data for TMV-6 and PF. TMV-6 (0-20 μM in terms of TEMPO) was titrated into solutions of PF (0.2 μM).	94
Figure C1. ^1H NMR spectrum of 2	97
Figure C2. ^{13}C NMR spectrum of 2	98
Figure C3. ^1H NMR spectrum of 3	99
Figure C4. ^{13}C NMR spectrum of 3	99
Figure C5. ^1H NMR spectrum of 4	100
Figure C6. ^1H NMR spectrum of 5	101
Figure C7. ^{13}C NMR spectrum of 5	102

LIST OF TABLES

Table 3.1. Comparison of relaxivity values between contrast agents.....	41
-------------------------------------------------------------------------	----

CHAPTER 1

INTRODUCTION

1.1 Introduction to Regulating Stimulus Responses of Functional Materials

Functional materials describe a class of materials possessing one or more properties (e.g., size, morphology, charge, color, fluorescence, etc.) that are responsive to external stimuli (e.g., thermal, mechanical, photic, pH, etc.).¹⁻⁵ These materials are the foundation of many applications that require predictable and tractable changes in properties.⁶⁻⁷ Sensors,^{5, 8} artificial muscles,⁹⁻¹⁰ drug delivery systems,¹⁰⁻¹² and data storage⁸ systems are prominent examples of industrially and commercially relevant applications that rely on functional materials to perform their primary duties. Due to their universal appeal, massive efforts have been, are being, and will continue to be directed at the development of novel functional materials.

Of the myriad functional materials that currently exist or are known, many have the desired functionality for an intended application, but are not utilized due to the lack of control of the stimulus response of the material or the incompatibility of the material with its intended environment.^{5, 10} The regulation or optimization of the stimulus responses of these materials would establish their viability not only for their intended applications, but many emergent applications and environments. In addition, the knowledge gained from regulating the stimulus responses would benefit the development of novel materials with similar functionalities.

Many efforts to regulate a wide array of stimulus responses across an even wider range of materials have been made. An attempt to sufficiently discuss all of these efforts is beyond the

scope of this dissertation. As such, the discussions in this dissertation will be limited to specific examples of pH- and redox-responsive materials.

1.2 pH-Responsive Materials

Currently, external stimuli can be differentiated by three main classes—physical, chemical, and biological.⁵ Physical stimuli describe the most fundamental interactions between matter and include temperature, motion, light, and magnetism. Chemical stimuli describe changes in the elemental composition of a sample of matter and include pH, ionic strength, oxidation state, and intermolecular interactions. Biological stimuli describe combinations of higher-order physical and chemical stimuli as applied to living systems and include receptor-specific complexation, changes in protein and nucleic acid structures, and ion gradients. Of stimuli mentioned above, materials featuring pH-responsive functionality are of particular interest due to the role of pH in many biological systems.³

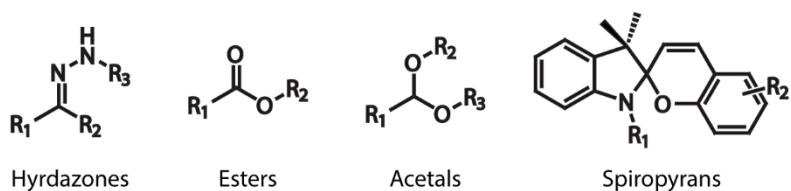


Figure 1.1. Examples of pH-responsive functional groups.

pH is defined as the negative base 10 logarithm of the hydrogen ion activity (often generalized to hydrogen ion concentration) in aqueous solutions and is used as a measure of acidity. It is one among many chemical properties that determine the organization and function of

biological systems. The significance of pH is well understood across many biological systems from bacterial flagella¹³ to acid-based digestion¹⁴ to blood buffering.¹⁵⁻¹⁶ The ubiquity of pH regulated systems in biological contexts means that functional materials able to effectively respond to pH stimuli hold great potential for therapeutics with applications ranging from cancer treatment to diabetes. However, two major issues currently limit⁴ both the variety and therapeutic applications of pH-responsive functional materials: (i) the specific mechanisms and pathways behind how pH is regulated is limited in many systems and (ii) the design of pH-responsive functional materials is difficult due to fundamental drug design issues of potency, selectivity, and stability. Issue (i) is of particular importance in the design of pH-responsive functional materials because although the significance of pH in many biological systems is well understood, detailed knowledge about the regulation of pH in both the target system and the surrounding connected systems is required before the design of functional materials can even begin. Changes in pH in one part of an organism can potentially cause wide-reaching pH changes across other parts of the organism. Isolating the pathways that regulate pH in the target system of an organism are therefore required to understand where, when, and how functional materials should interact with the target system to achieve the desired outcome in the organism without causing unintended effects. Unfortunately, achieving this comprehensive understanding of pH regulation is difficult since many biological systems within organisms are closely connected and interdependent.¹² Nevertheless, significant progress has been made in understanding local pH regulation in several mammalian cell systems. One notable example is the significance and regulation of pH in tumor microenvironments. It has long been known that some tumor microenvironments are acidic, but only relatively recently have the mechanisms behind the acidic conditions and the reasons for why tumors would support such

conditions been elucidated.¹⁷⁻²⁰ Upon realizing the metabolic processes that result in acidic tumor environments and the role acidic conditions play in the sustenance and recruitment of certain tumors, many groups have designed functional materials that rely on pH-responsiveness to target or disrupt certain pathways that support tumor growth.²¹⁻²⁵ Although no specific material has provided either comprehensive understanding or treatment of cancer, the underlying designs behind these pH-responsive materials show promise in advancing cancer therapeutics.

Another area in which the significance and regulation of pH is becoming increasingly understood is wound healing. Similar to the case with tumor microenvironments, wounds can become acidic during the healing process and the mechanisms and reasons for such changes in pH are being investigated.²⁶⁻²⁸ While pH-responsive materials that focus on wound healing are not common relative to materials that focus on cancer therapeutics, they can still be useful in improving understanding of the mechanisms behind how cells traffic food, drug, or waste particles. Understanding and modulating cellular uptake would provide tools needed to design materials for the treatment of both cancer and wounds.

1.3 Redox-Responsive Materials

Reduction-oxidation, or redox, reactions involve the transfer of electrons such that a chemical species gains electrons (reduction) while another loses electrons (oxidation). Redox reactions are similar to pH in that both perform significant roles across many biological systems. Aerobic respiration,²⁹⁻³¹ nitrogen fixation,³² and photosynthesis³³⁻³⁴ are only a few examples of biological processes of which redox reactions are critical components. As in the case with pH, the ubiquity

of redox reactions in biological contexts provides many opportunities to utilize redox-responsive functional materials for therapeutic applications. Many small molecule prodrugs already rely on redox stimuli for activation and the development of redox-responsive materials for chemotherapy has exploded these past few years. Although much work has been focused on the use of redox-responsive materials for drug design and drug delivery, medical imaging, specifically the development of organic radical contrast agents (ORCAs) for magnetic resonance imaging (MRI), is one area in which redox-responsive materials could contribute immensely to.

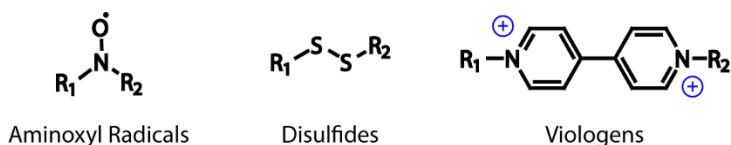


Figure 1.2. Examples of redox-responsive functional groups.

1.3.1 Organic Radical Contrast Agents (ORCAs)

ORCAs have gained attention as potential replacements for metal-based contrast agents. ORCAs would offer reduced toxicity and increased tunability relative to their metal-based counterparts.³⁵ ORCAs featuring aminoxy radicals are among the most well studied ORCAs due to their stability under ambient conditions, compatibility with existing clinical imaging equipment, and biocompatibility. Aminoxy radicals specifically refer to molecules containing the R₂N-O· functional group, with the single unpaired electron conferring paramagnetism on molecules containing aminoxy functionality.³⁶ Like other radicals, aminoxy radicals can be highly reactive.

However, many stable aminoxyl radicals like TEMPO or PROXYL feature bulky substituents on the nitrogen atom along with the absence of α -hydrogen atoms.³⁶ The bulky substituents sterically hinder the aminoxyl radical from dimerization and reduces its reactivity with other molecules. The absence of α -hydrogen atoms eliminates the possibility of reactions involving hydrogen abstraction. Aminoxyl radicals have been used for several decades as spin labels and spin traps,³⁷⁻³⁸ but only relatively recently have they been investigated as serious candidates for the development of ORCAs.

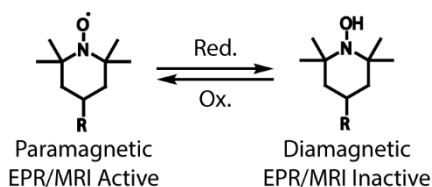


Figure 1.3. The oxidized and reduced forms of aminoxyl radicals.

As previously mentioned, the stability and low propensity of aminoxyl radicals to trigger toxic side effects are extremely desirable properties, but two major issues have prevented aminoxyl-based ORCAs from being utilized for mainstream clinical applications. One major issue stems from the single unpaired electron of the aminoxyl group. Relative to many contrast agents (with more unpaired electrons) currently used in clinical settings, the aminoxyl moiety provides weaker contrast.³⁹⁻⁴⁰ This issue has been investigated extensively and a common solution has been to graft multiple aminoxyl moieties onto a scaffold in order to increase the local concentration of aminoxyl radicals.⁴¹⁻⁴⁴ Scaffolds have included polymers, “hard” nanoparticles such as those based on silica, and more recently, virus-like particles (VLPs). This strategy of increasing the local

concentration of aminoxyl radicals has so far proven to be effective under some clinically relevant conditions and continues to be pursued as an option to enhance the contrast of aminoxyl-based ORCAs.

The other issue concerns the redox susceptibility of aminoxyl radicals. While aminoxyl radicals, especially sterically hindered examples like TEMPO or PROXYL, are far more stable under ambient conditions than many other radical compounds, they are not inert. Physiologically relevant reducing agents like ascorbate can still react with the aminoxyl moiety via a one-electron, one-proton transfer, thereby converting the aminoxyl radical into a hydroxylamine.^{36, 45-46} Hydroxylamines no longer possess any unpaired electrons and are essentially a diamagnetic species, meaning that they do not function as effective MRI contrast agents. Since ascorbate and other reducing agents are normally present in blood, existing aminoxyl-based ORCAs are only effective as contrast agents for a few minutes before they are reduced to MRI-silent diamagnetic species. This rapid rate of reduction presents a problem for clinical applications because typical clinical MRI experiments occur over a longer timeframe.⁴⁷ Efforts to mitigate the reduction of aminoxyl radicals have largely focused on further increasing the bulk of the substituents on the nitrogen atom and/or incorporating many aminoxyl radicals into polymeric or macromolecular systems in such a way that the resulting structure shields the aminoxyl radicals from reducing agents.^{41-44, 47-49} While these efforts have made progress in extending the lifetime of aminoxyl radicals in the presence of reducing agents, persistent aminoxyl-based ORCAs that possess circulation lifetimes suitable for clinical applications have yet to be seen.

1.4 Virus-Like Particles and Viral Nanoparticles

Among the available scaffolds upon which functional nanoparticles can be built, virus-like particles (VLPs) and viral nanoparticles (VNPs) have recently gained attention in the fields of biotechnology and biomedicine.⁵⁰⁻⁵⁹ VLPs are macromolecular structures composed of self-assembled protein subunits and/or nucleic acid strands. VNPs are similar to VLPs in that they are also self-assembled macromolecular structures composed of protein and/or nucleic acid but differ in that they are based on whole viruses instead of recombinant or mutant non-replicating assemblies. Since many VNPs relevant to human clinical applications are plant-based and unable to replicate in mammals, VNPs will be considered functionally identical to VLPs and labeled as such for the purposes of this discussion. Relative to silica, polymeric, or metallic nanoparticles, VLPs offer the advantages of being monodisperse, highly functionalizable, and biodegradable.⁵⁰⁻⁵⁹ Relative to many other proteins that serve as the basis for functional materials, VLPs are resilient against heat and organic solvents. The unique features of VLPs make them an attractive option for the fabrication of clinically relevant functional materials.⁴ This dissertation will discuss the use of two VLPs, Q β and tobacco mosaic virus (TMV), for the fabrication of pH-responsive and redox-responsive materials, respectively.

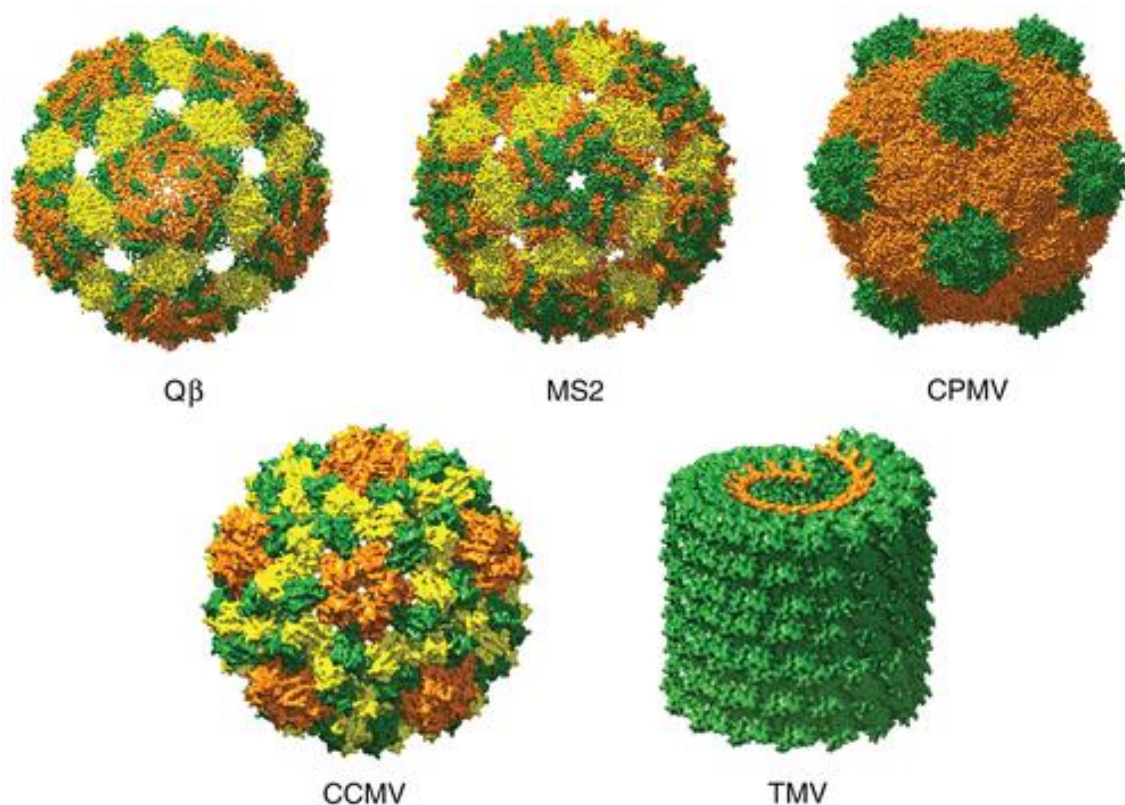


Figure 1.4. Crystallographically obtained structures of common VLPs Q β , MS2, Cowpea Mosaic Virus (CPMV), Cowpea Chlorotic Mosaic Virus (CCMV), and Tobacco Mosaic Virus (TMV). TMV is not illustrated to scale. Reproduced from Chen, Z.; Li, N.; Li, S.; Dharmarwardana, M.; Schlimme, A.; Gassensmith, J. J. *WIREs Nanomed. Nanobiotechnol.* **2016**, 8, 512–534. with permission from John Wiley and Sons.

Q β is a 28 nm icosahedral recombinant VLP based on bacteriophage Q β . It is composed of 180 identical coat protein subunits are self-assembled around ssRNA and are linked to each other via the C74 and C80 residues of each coat protein.^{50, 60} Each 14.1 kDa protein subunit contains six solvent exposed residues for functionalization. Two of these residues are the previously mentioned cysteine residues that feature functionalizable thiols (when reduced) while the other four residues are the N-terminus A1, K2, K13, and K46.^{50, 60} The latter four residues feature primary amines for functionalization. The ease in functionalizing the solvent exposed residues of Q β has been

demonstrated on many occasions and stems in part from the wide array of mild and orthogonal reactions that these functional handles allow. The high thermal and organic solvent stability of the Q β capsid also contribute to its ease of functionalization. The functionalizability and resiliency of Q β explain its emergence as a versatile workhorse in VLP technology for the design of functional materials.¹¹

TMV was the first virus to be discovered and is one of the most widely studied plant viruses in plant pathology. TMV is a 300×18 nm hollow, rod-shaped virus composed of 2130 identical coat protein subunits self-assembled around ssRNA.⁶¹⁻⁶³ Each 17.5 kDa protein subunit contains three solvent exposed residues (E97, E106, and Y139) available for functionalization.⁶⁴⁻⁶⁷ When the coat proteins are assembled in the native TMV rod morphology, the glutamate residues line the surface of the interior pore (4 nm diameter) while the tyrosine residues line the exterior surface of the TMV rod.^{63, 65} The facile synthetic modification opportunities these solvent exposed residues offer, along with the ability to tolerate wide ranges of temperatures, organic solvents, and pH values, have allowed TMV to also rise in prominence as a versatile platform in VLP technology for the design of functional materials.

1.5 Summary

Functional materials encompass a vast array of materials and their respective responses to various external stimuli. Proper regulation of these stimulus responses is essential in establishing the viability of these materials for their intended applications along with emergent applications and environments. In the context of biological systems, improved understanding of how to regulate pH- and redox-responsive systems will advance greatly not only the design of therapeutics directly relevant to these stimuli, but therapeutics in general. The emphasis on pH- and redox-responsive systems is owing to the significance and ubiquity of these two stimuli in the proper function of biological systems. If effectively designed and utilized, pH- and redox-responsive materials can detect the state of and/or alter a multitude of key biochemical pathways.

The current chapter, Chapter 1, of this dissertation introduces the concept of functional materials and broadly, the regulation of their stimulus responses. Regulation of the two external stimuli of focus in this dissertation, pH and redox, are also briefly introduced. Finally, VLPs, which are the platforms upon which the pH- and redox-responsive materials discussed in this dissertation are built, are introduced. Chapter 2 will focus on the design and utilization of pH-responsive materials to enhance the understanding and regulation of cellular uptake. Chapters 3 and 4 concern the design of redox-responsive materials for use as MRI contrast agents. The final chapter, Chapter 5, will discuss the future directions and final thoughts on the sum of the work covered in this dissertation and its impact on the role of functional materials in society.

CHAPTER 2
REGULATING THE UPTAKE OF VIRAL NANOPARTICLES IN MACROPHAGE
AND CANCER CELLS VIA A PH SWITCH⁽¹⁾

Authors – Hamilton Lee, Candace E. Benjamin, Chance M. Nowak, Lana H. Tuong, Raymond P. Welch, Zhuo Chen, Madushani Dharmarwardana, Kyle W. Murray, Leonidis Bleris, Sheena D’Arcy, Jeremiah J. Gassensmith*

The Department of Chemistry and Biochemistry, BSB 13.102

The University of Texas at Dallas

800 West Campbell Road

Richardson, Texas 75080-3021

⁽¹⁾Portions reprinted with permission from Hamilton Lee, Candace E. Benjamin, Chance M. Nowak, Lana H. Tuong, Raymond P. Welch, Zhuo Chen, Madushani Dharmarwardana, Kyle W. Murray, Leonidas Bleris, Sheena D’Arcy, and Jeremiah J. Gassensmith
Molecular Pharmaceutics **2018** 15 (8), 2984-2990. Copyright 2018 American Chemical Society.

2.1 Introduction

Nanoparticles have played a key role in various fields of biomedical research in the last few decades for a wide array of applications.⁶⁸⁻⁷² While the amount of research in this area has been significant, the specific mechanisms behind the cellular uptake of nanoparticles and the particular parameters required to modulate uptake are still not fully understood.⁷³⁻⁷⁵ It has been widely demonstrated^{73-74, 76-82} that factors, including the size, shape, charge, and hydrophobicity of nanoparticles, significantly affect the uptake of nanoparticles by cells. Specifically, the surface charge of nanoparticles has been considered a critical factor for applications involving imaging and drug delivery.⁷⁴

The surface charge of nanoparticles has been shown to affect nanoparticle uptake by cells largely, but not solely, through nonspecific electrostatic interactions between the charged moieties on the nanoparticle and phospholipid head groups or protein domains on the membrane of the cell.^{76, 78, 83-84} The implication of this view is that nanoparticles with positive surface charges are more favored for uptake by cells, while nanoparticles with negative surface charges are less favored for uptake. This fact has been exploited elegantly by a number of researchers to alter cell uptake in a variety of mammalian cell types.^{78, 84-89} Although different cell lines react to surface charges of nanoparticles in varying degrees, the previous statement generally holds true across cell types with the exception of phagocytes. Macrophages have been shown to favor the uptake of negatively charged nanoparticles to that of positively charged particles.⁹⁰⁻⁹¹ This observation has been explained by fact that macrophages are known to phagocytose negatively charged cells, such as bacteria, and are thus expected to favor the uptake of negatively charged particles.⁹²

Consequently, reports on controlling the uptake of nanoparticles in macrophages are rare and would be of considerable value for researchers. Macrophages are a type of phagocytic cell that is responsible for clearing foreign materials from the body by shunting them into the organs of the mononuclear phagocyte system, like the liver and kidneys for excretion. Consequently, this recognition and disposal system can potentially reduce the circulatory half-life of nanotherapeutics preventing them from reaching their targets. On the other hand, selective stimulation of the immune system in the context of vaccine development, wound treatment, or targeting infections by controlling when and where the innate immune system is active would be of significant therapeutic interest for researchers in areas from wound treatment to cancer immunotherapy.

Modulating the uptake ability of nanoparticles by switching the surface charge from negative to positive has been an approach to controlling their uptake until a specific stimulus is triggered.^{85-86, 93} This charge inversion strategy holds potential for increasing the safety and efficacy of existing payload delivery systems by increasing the selectivity of nanoparticle uptake by the intended cells. We set out to utilize this strategy using the virus-like particle (VLP) Q β as a scaffold for which charged small molecules could be conjugated to reversibly modify cell uptake properties in macrophage models. Our charge inversion strategy relies on acidic environments as a trigger, but we are not pursuing the use of this system in tumor microenvironments, which are not sufficiently acidic. Instead, we are focusing on tissue injuries, where the extracellular pH can be as low as 4.²⁶⁻²⁸

In this article, we highlight our investigations regarding the uptake of our Q β conjugates by RAW 264.7 macrophages and HeLa cells. We show that we can reversibly alter the uptake

properties relative to unfunctionalized Q β when the terminal moiety is hexanoic acid. We also demonstrate that the hydrazone linker in our hydrazone-based Q β conjugates hydrolyze when incubated in acidic conditions, allowing for the pH-mediated cell uptake of those conjugates. Our findings suggest that when the size and shape of Q β nanoparticles are controlled for, the conjugation of a negatively charged terminal hexanoic acid moiety onto the surface of Q β significantly affects its uptake characteristics by both macrophages and cancer cells.

2.2 Results and Discussion

VLPs offer the advantages of being monodisperse, highly functionalizable, and biodegradable when compared to silica, polymeric, or metallic nanoparticles.^{50-51, 53-56, 94} VLPs are self-assembled macromolecular structures composed of tens to thousands of individual protein subunits.⁵⁷ The particular VLP utilized in this article is bacteriophage Q β , a 28 nm icosahedral protein nanoparticle with a capsid composed of 180 identical coat proteins. These coat proteins self-assemble around ssRNA and are linked together via disulfide bonds between the Cys74 and Cys80 residues of each coat protein. Each 14.1 kDa coat protein is composed of 132 amino acids, with four of these residues, the N-terminus Ala1, Lys2, Lys13, and Lys46, being solvent exposed and featuring primary amines available for functionalization (**Figure 2.1**).^{50, 60} The ease of synthetic modification and its resilience against heat and solvent have allowed Q β to emerge as a workhorse in VLP nanotechnology as a promising candidate in vaccine and immunotherapeutic applications, making it an excellent model for our study.^{11, 50, 58-59}

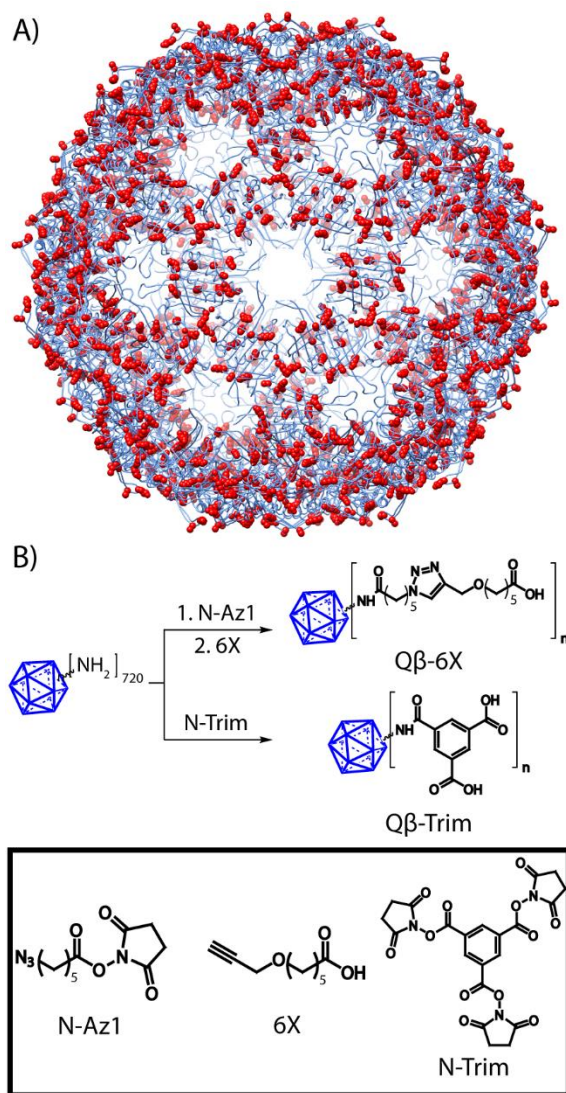


Figure 2.1. (A) Structure of Qβ^a and (B) Synthesis of Both Conjugates Qβ-6X and Qβ-Trim^b.

^aRed spheres correspond to primary amines.

^bBlue icosahedron represents Qβ.

The exposed primary amines were utilized for the conjugation of terminal carboxylate moieties to provide a negative charge to the surface of Qβ. To keep our analysis simple, we started with a hexanoic acid derivative. To that end, 6-(prop-2-yn-1-yloxy)hexanoic acid (6X) was conjugated to the solvent exposed lysine residues on the surface of Qβ. We also prepared a trimesic

acid (Trim) derivative under the assumption that two negative charges should be more effective than one, and both syntheses are illustrated in **Figure 2.1B**. These two conjugates were characterized by MALDI-TOF mass spectrometry, transmission electron microscopy (TEM), and dynamic light scattering (DLS) and were found to have retained the characteristic morphology of the underlying VLP (**Figure 2.2**). MALDI-TOF revealed that an average of two modifications per coat protein occurred with both derivatives. Native agarose gel electrophoresis showed a clear band shift of the conjugates toward the positive electrode despite being modestly larger, suggesting that the overall charge of the VLP had become more negative for both conjugates.

We prepared conjugates using Q β internally loaded with green fluorescent protein (Q β _(GFP)) to provide a fluorescent tag⁹⁵ for imaging studies. Both conjugates were incubated in the presence of animal serum with HeLa and RAW 264.7 macrophage cells. To our surprise, the conjugates behaved quite differently. According to flow cytometry analysis, shown in **Figure 2.3**, the cellular uptake of Q β _(GFP)-6X was inhibited while the uptake of Q β _(GFP)-Trim was not, despite trimesic acid having an additional negative charge. To our knowledge, hexanoic acid does not have a specific receptor that mediates the uptake of nanoparticles by cells, though a review of the literature⁹⁶ done after our experiment suggested that derivatives of benzoic acid, which we believe our conjugate most closely resembles, do.

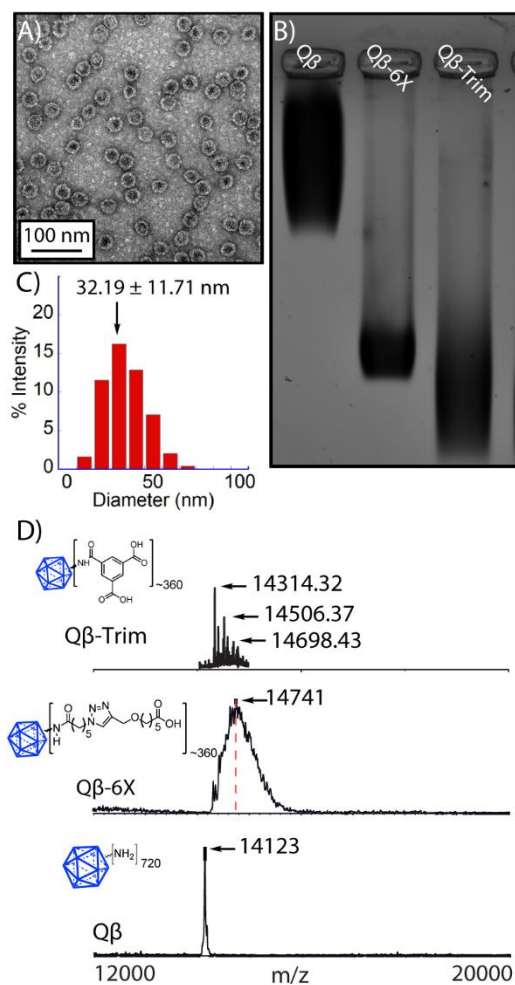


Figure 2.2. (A) TEM image of Qβ-6X. (B) Native agarose gel electrophoresis of Qβ, Qβ-6X, and Qβ-Trim. The greater mobility toward the positive electrode (bottom) suggests an increase in negative charge. (C) Dynamic light scattering data of Qβ-6X. (D) MALDI-TOF mass spectra of Qβ and Qβ-6X showing observed masses. ESI-TOF mass spectrum of Qβ-Trim showing one, two, and three functionalized residues per coat protein.

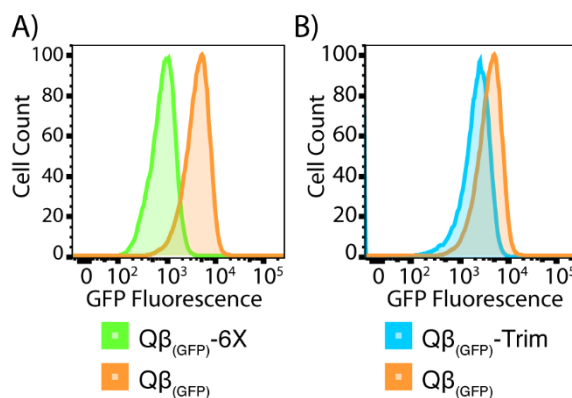


Figure 2.3. Representative histogram from flow cytometry studies corresponding to RAW 264.7 macrophages incubated with their respective Qβ_(GFP) samples at 40 μM. All cells were incubated with the Qβ conjugates for 4 h at 37 °C.

With these results in hand, we next sought to introduce a stimuli responsive switch between the capsid and the hexanoic acid moiety. This would accomplish two objectives: (1) it would demonstrate that the linkage between the hexanoic acid and the VLP is amenable to modification without altering the structure–property relationship, and (2) it would provide a proof-of-principle example of using “charge flipping” to alter uptake behavior. To that end, we designed a hydrazone linkage, which is cleavable under the acidic pH typically found in the skin or in wounds, where immune activation by a vaccine adjuvant would likely be most efficacious.²⁶⁻²⁸ Hydrazones have been frequently used for their ability to hydrolyze in mildly acidic conditions and, in particular, for cargo release from nanoparticles inside endosomes.^{50, 97-99} These pH ranges are compatible with the Qβ VLP.¹⁰⁰ In addition, the resulting terminal hydrazine moiety, after the cleavage of the hydrazone bond, should form a cationic hydrazinium ion following protonation in water.

We thus created two hydrazone analogues of hexanoic acid to test their efficacy as a pH-mediated switch. Conjugation of the hydrazone switch is shown in **Figure 2.4**. We varied the

hydrazone linker length by using both 1-chloropropan-2-one and 1-chloropentanone. Briefly, an NHS-ester containing hydrazone and azide functionalities was attached to 6X in situ via a copper catalyzed azide–alkyne cycloaddition (CuAAC). A solution of Q β was added and after completion of the reaction, the resulting conjugate was purified via centrifuge filtration. As shown in **Figures 2.5A,C and A19**, the resulting conjugates maintain their spherical morphology.

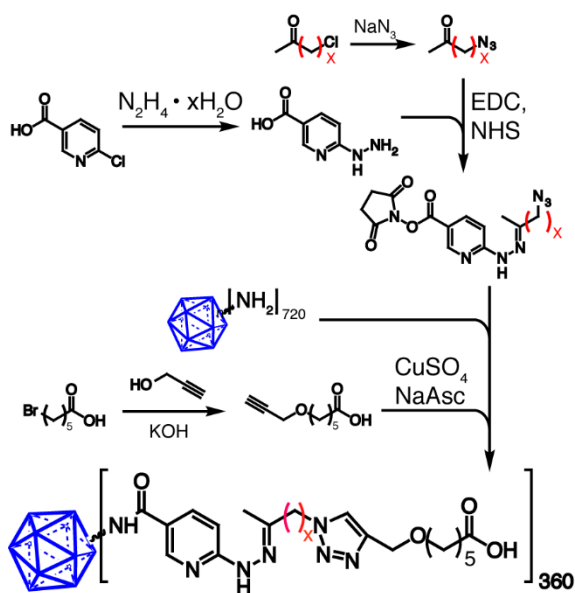


Figure 2.4. Synthesis of Q β -Z Conjugates^a.

^aThe use of 1-chloropropan-2-one ($X = 1$) as a starting material results in Q β -ZX. The use of 5-chloropentan-2-one ($X = 3$) results in Q β -ZX2.

The electrophoretic mobility of proteins can be used to approximate their relative surface charge given that their size and morphologies are similar. The effect of the terminal carboxylic acid moieties on the surface charge of the Q β conjugates was evaluated via native agarose gel electrophoresis. A representative gel comparing the electrophoretic mobility of unfunctionalized Q β to Q β conjugates, including both the hexanoic acid-terminated hydrazone (ZX) as well as the

hydrolyzed version of the same (ZX-Hyd), is shown in **Figure 2.5B**. Unsurprisingly, all the anionic conjugates show greater electrophoretic mobility than the unfunctionalized Q β sample. To test the efficacy of the hydrazone switch, the Q β -Z conjugates were incubated in MES buffer (0.1 M, pH 5.0) for 48 h. The electrophoretic mobilities of the Q β -ZX-Hyd conjugates were reduced relative to the Q β -Z conjugates that had not undergone incubation in acidic conditions. It is not clear why the putatively protonated hydrolyzed hydrazine conjugates did not retreat to approximately the same position as the unfunctionalized Q β . ESI-TOF data (**Figure A16**) show the predicted mass of the hydrolyzed product.

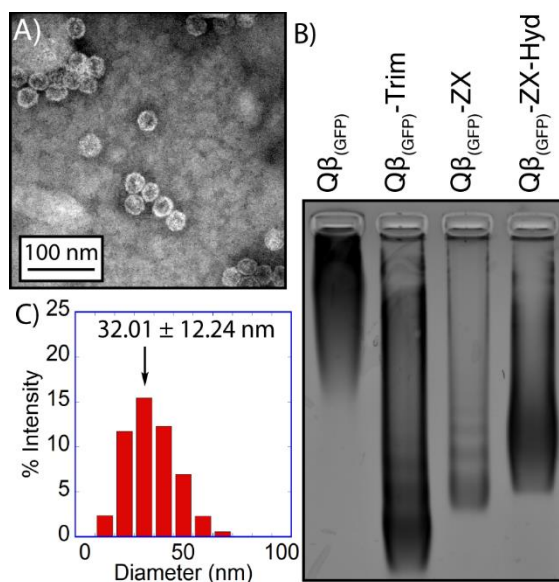


Figure 2.5. (A) TEM micrograph of the Q β (GFP)-ZX conjugate. (B) Native agarose gel electrophoresis showing Q β , Q β conjugates, and the hydrolyzed product Q β -ZX-Hyd. (C) DLS measurement of the Q β (GFP)-ZX conjugate showing a uniform size distribution. The measurements were taken in KP buffer (0.1 M, pH 7.4, 25 °C) at concentrations of \sim 1 mg/mL.

The kinetics of the hydrazone hydrolysis were investigated using fluorescence spectroscopy, since the Q β conjugates may hold potential for therapeutic applications involving the delivery of payloads to specific targets. Although hydrazones reliably hydrolyze in mildly acidic conditions, the local chemical environment may affect the rate of hydrolysis. Q β -ZFITC (**Figure 2.6A**), a Q β conjugate containing a terminal FITC moiety and a hydrazone linker, was synthesized for this study.

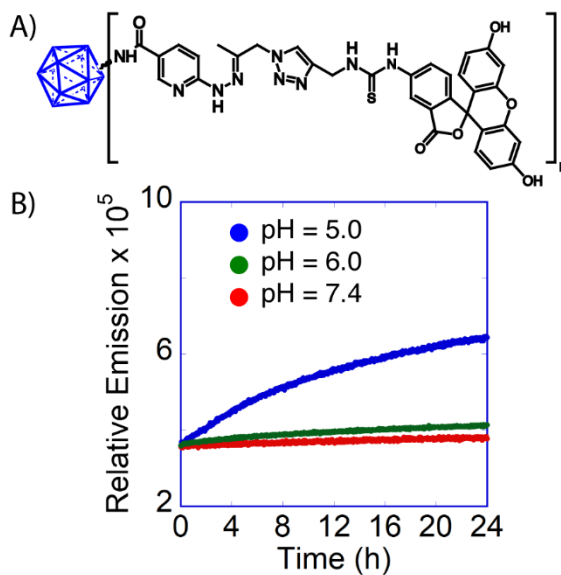


Figure 2.6. (A) Q β -ZFITC was used for the kinetics studies. (B) Release profiles of FITC from Q β -ZFITC at pH 7.4 (KP buffer, 0.1 M, 25 °C), pH 6.0 (MES buffer, 0.1 M, 25 °C), and pH 5.0 (MES buffer, 0.1 M, 25 °C).

The fluorescence of FITC ($\lambda_{\text{Ex}} = 450 \text{ nm}$; $\lambda_{\text{Em}} = 520 \text{ nm}$) and other fluorescein derivatives are known to self-quench at high local concentrations¹⁰¹⁻¹⁰² while conjugated to the capsid. As the hydrolysis proceeds, releasing FITC into the solution, the increase in fluorescence can be monitored over time. We tracked the release of FITC from the VLP into solutions at a pH of 7.4,

6.0, and 5.0. The maximum fluorescence was seen after 24 h at pH 5.0, while very small increases in fluorescence were observed over the same time period for the conjugates incubated at pH 7.4 and 6.0 (**Figure 2.6B**). When the fluorescence values were fit to a pseudo-first-order reaction model, the half-lives of hydrazone hydrolysis at pH 7.4, 6.0, and 5.0 were 21.3, 9.6, and 6.4 h, respectively. The observed kinetics results are consistent with the expected hydrolysis properties of the hydrazone linker. While these half-lives are likely too long for therapeutic use, we have confirmed the chemistry works. The question of the extent of hydrolysis is still pending, but it is obvious that hydrolysis is occurring by the change in fluorescence, the identification of the predicted mass by MALDI-TOF, and the difference in electrophoretic mobility.

Finally, we turned to in vitro studies to determine the efficacy of our strategy. Flow cytometry and fluorescence microscopy were used to evaluate the cell uptake efficiency of the Q β conjugates. Phagocytic cells have been shown to favor the uptake of negatively charged nanoparticles, so their use in probing the uptake characteristics of the different Q β conjugates could advance the understanding of the mechanisms behind the uptake selectivity of phagocytic cells. RAW 264.7 macrophages and HeLa cells were incubated in cell media containing 10% serum with their respective Q β conjugates for 4 h. The concentrations of the Q β conjugates ranged from 10 to 50 μ M relative to the coat protein. A comparison of the cell uptake efficiency by flow cytometry of the Q β -ZX conjugate and its hydrolyzed form, Q β -ZX-Hyd, is shown in **Figure 2.7A,B**. When both cell lines were incubated with the Q β conjugates at 10 μ M, no significant changes in the fluorescence intensities of the cells were observed, even for the unfunctionalized Q $\beta_{(GFP)}$ positive control. This result suggests that the concentration of Q β conjugates used for incubation were too

low for the detection of fluorescence. When both cell lines were incubated with the Q β conjugates at 50 μ M, significant differences in the fluorescence intensities of cell populations were observed. The RAW 264.7 macrophages incubated with 50 μ M Q β -ZX-Hyd displayed a noticeable increase in fluorescence intensity, while the macrophages incubated with 50 μ M Q β -ZX did not. This suggests that the macrophages have internalized the positively charged Q β -ZX-Hyd conjugate. We wanted to see if these results were specific to the macrophages, so we tested them on HeLa cells, which were incubated with Q β conjugates at 50 μ M. Although HeLa cells incubated with 50 μ M Q β -ZX-Hyd displayed a clear increase in fluorescence intensity while the cells incubated with 50 μ M Q β -ZX did not, the magnitude of the increase in fluorescence intensity is far lower than what is observed for the RAW 264.7 macrophages. This is expected because macrophages are commonly known to internalize a wide array of foreign materials due to their role as phagocytes.^{74, 76, 78, 103-104} These results are further illustrated in **Figure 2.7C,D** by fluorescence imaging, showing the internalization of the Q β -ZX-Hyd conjugates yet zero internal fluorescence of Q β -ZX. We repeated these tests on the Q β -ZX2 conjugate, which has a longer linker between the VLP and the hexanoic acid (see **Figure 2.4**), and found the same results from flow cytometry. This result also corroborates our hypothesis that the linker between the VLP and the hexanoic acid moiety can be altered without changing the structure–function properties. We anticipate that other linker designs, for instance, ones that are cleavable by enzymatic activity or light, are likely also able to be tolerated and, as such, expand on the generalizability of this approach.

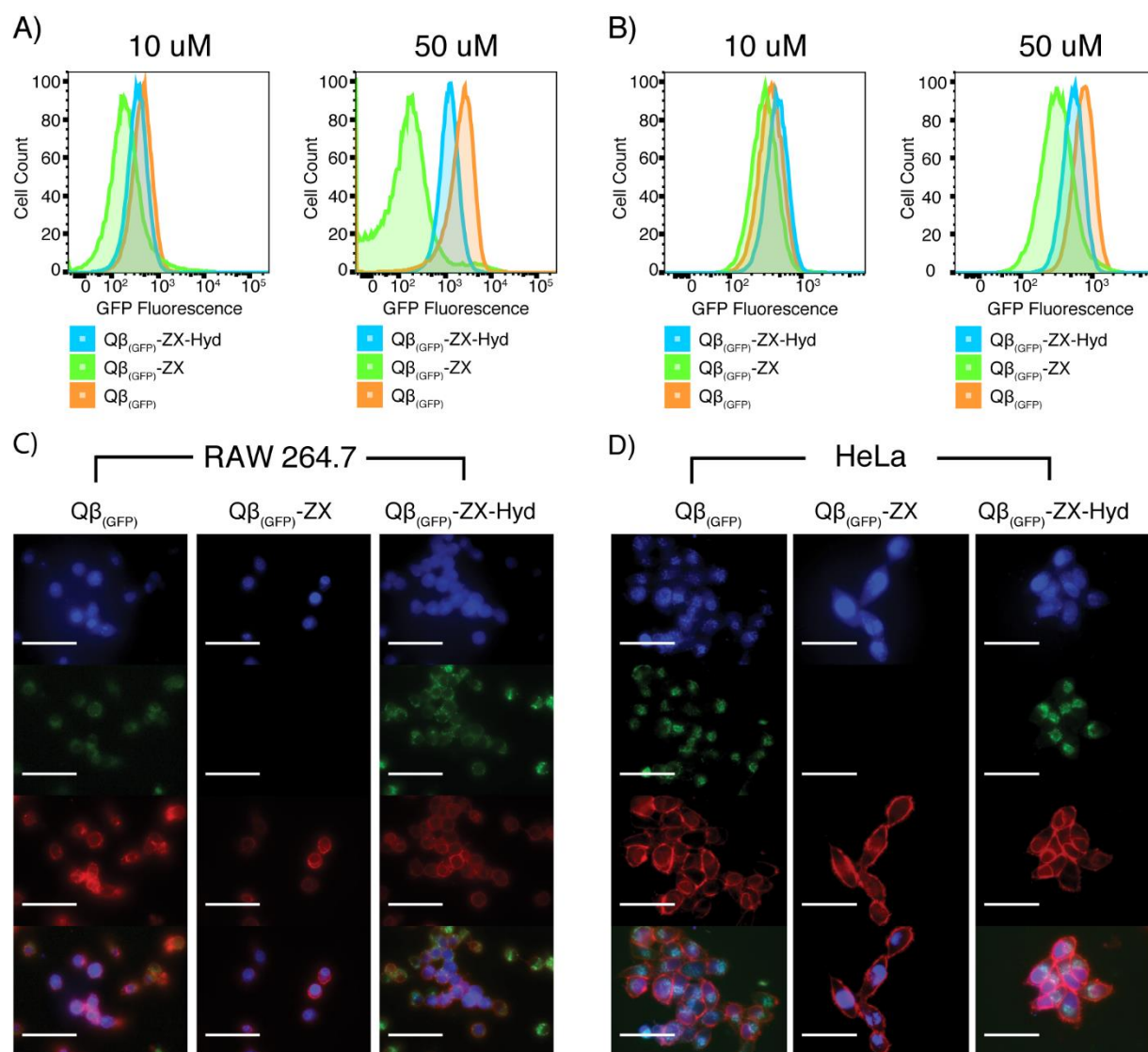


Figure 2.7. Representative histograms from flow cytometry studies corresponding to (A) RAW 264.7 macrophages and (B) HeLa cells incubated with their respective Q β samples. Epifluorescence microscope images of (C) RAW 264.7 macrophages and (D) HeLa cells incubated with their respective Q β samples (50 μ M). Blue: DAPI; red: WGA-AlexaFluor 555; and green: GFP. Scale bar represents 50 μ m. All cells were incubated with the QB conjugates for 4 h at 37 $^{\circ}$ C.

2.3 Conclusions

We have shown that conjugating terminal hexanoic acid moieties onto the surface of VLP Q β inhibits the uptake of the conjugate by RAW 264.7 macrophages and HeLa cells. Installing hydrazone linkers between the surface of Q β and the terminal alkyl carboxylate moieties results in a pH-responsive conjugate that, in acidic conditions, can release the terminal hexanoic acid moiety and allow for the uptake of the Q β nanoparticle. Importantly, the installation of the “pH switch” did not change the structure–function properties of the hexanoic acid linker. Collectively, these findings are a helpful reminder that, even when the size and shape of nanoparticles are controlled for, charge alone does not always account for its uptake characteristics by both macrophages and HeLa cells. In addition, these findings highlight the need for further studies to advance the understanding of the requirements necessary to design effective nanoparticle-based systems for the delivery of payloads into cells.

Materials, instrumentation, experimental methods, and supporting information can be found in **Appendix A**.

CHAPTER 3

ENHANCING THE SURVIVABILITY OF AMINOXYL ORCAS VIA SHIELDING WITH CUCURBIT[8]URIL

3.1 Introduction

Of the many spatially resolved biomedical imaging techniques available, magnetic resonance imaging (MRI) is of particular importance in modern medicine owing to its non-invasive nature, potential for high spatial resolution, tissue penetration, and lack of non-ionizing radiation.³⁵ MRI relies on detecting the energy released over time by water protons returning to magnetic equilibrium after a radio frequency (RF) pulse has been applied. The process of protons returning to magnetic equilibrium is referred to as relaxation. Differences in the chemical environment of water molecules (e.g., water in one type of tissue versus water in another type of tissue) affect the relaxation time of water protons. These differences in relaxation time are used to map the boundaries of different types of tissue and construct a visually interpretable image of the body. Since water intrinsically possesses low sensitivity to magnetic fields, contrast agents are usually required to increase the contrast between different features in the final image. Contrast agents increase MR contrast by interacting with the dipole moments of nearby water molecules such that the relaxation times of water protons are reduced.¹⁰⁵⁻¹⁰⁷ The majority of modern MRI contrast agents are based on gadolinium (Gd), or more specifically, Gd^{3+} complexes. This is due to the excellent paramagnetic properties and high stability of Gd in conditions relevant for MRI.^{39-40, 108} Although Gd has performed¹⁰⁹⁻¹¹¹ remarkably in clinical settings (MRI contrast can be enhanced by several orders of magnitude), concerns about its toxicity,¹¹²⁻¹¹⁶ especially for patients with

impaired renal functionality, have catalyzed efforts to design alternatives to Gd and other metal-based MRI contrast agents.

While several types of metal-free contrast agents have been investigated,¹¹⁷⁻¹²⁴ organic radical contrast agents (ORCAs) based on paramagnetic aminoxyl moieties, show significant promise in eventually becoming the primary compounds for which MRI contrast agents are based. Aminoxyl ORCAs are distinguished by their compatibility with existing MRI techniques, enabling facile implementation in current clinical settings. Aminoxyl ORCAs also display low cytotoxicity and high biodegradability, reducing the potential for side effects.⁴⁷⁻⁴⁸ However, two major issues prevent aminoxyl-based ORCAs from replacing traditional contrast agents based on Gd: *(i)* their single unpaired electron provides weaker contrast compared to the seven unpaired electrons of Gd and *(ii)* they are reduced rapidly to MRI-silent hydroxylamines in physiological conditions by compounds including ascorbate, saccharides, and cysteine-rich proteins.⁴⁷ Issue *(i)* has been addressed by many groups and a common motif among ORCA designs attempting to increase the MRI contrast of aminoxyl-based molecules is the chaining together of multiple aminoxyl-containing molecules to polymer systems, resulting in high local concentrations of aminoxyl moieties. Chaining together aminoxyl radicals in this fashion increases the relaxivity (relaxation rate as a function of concentration) of the ORCA by utilizing not only local concentration effects, but also molecular motion. The increased size and mass and decreased rotation and diffusion rates of the ORCA means that the number of aligned water molecules that interact with an aminoxyl moiety at any given time is increased. Our group has demonstrated an alternative approach that relies on the conjugation of aminoxyl-containing molecules to proteins derived from the tobacco

mosaic virus (TMV), which self-assemble into highly anisotropic rigid nanorods.¹²⁵ The resulting conjugate was shown to have relaxivity values an order of magnitude higher than the free aminoxyl radical. The observed enhancement of relaxivity is attributed not only to increased local concentrations of aminoxyl moieties, but the reduced tumbling of the nanorod in solution.¹²⁶⁻¹³⁹ Issue (ii) has also been widely addressed with strategies primarily focused on mitigating reduction by: (1) installing sterically hindered moieties around the aminoxyl radical and (2) incorporating many aminoxyl-containing molecules into polymeric or other macromolecular systems with resulting conformations that shield the aminoxyl radical.⁴⁹ While these strategies have managed to reduce the reduction rate of aminoxyl radicals, circulation lifetimes still fall short of requirements for clinical viability. We have pursued the strategy of using a kinetically trapped macrocycle to sterically shield aminoxyl radicals from reduction. Several studies have shown¹⁴⁰⁻¹⁴⁴ that the macrocycle cucurbit[8]uril (CB[8]) can encage the aminoxyl radical TEMPO, leaving enough room for exchange of water, which is critical for MRI contrast, but preventing the entry of physiologically relevant reducing agents like ascorbate. By conjugating a TEMPO derivative onto the exterior surface of TMV, CB[8] can be bound to the TEMPO moiety via hydrophobic and ion-dipole interactions to form a pseudorotaxane.

In the following sections of this chapter, we highlight our investigations regarding the enhancement of the survivability of our aminoxyl ORCA via shielding with CB[8]. We demonstrate the fabrication of an ORCA that is essentially a pseudorotaxane using a VLP template. This pseudorotaxane is composed of CB[8] molecules bound to TEMPO moieties that have been conjugated onto the exterior surface of TMV. We also show that the pseudorotaxane architecture

of our ORCA is effective at shielding the aminoxyl radical from reduction by ascorbate while still allowing for the exchange of water. This selective shielding results in a substantial increase of the lifetime of our ORCA in the presence of ascorbate. Our observations suggest that the shielding of aminoxyl radicals with macrocycles is a promising strategy to utilize in the pursuit of a persistent ORCA viable for clinical applications.

3.2 Results and Discussion

Many types of nanomaterials have been investigated for their potential as platforms for aminoxyl-based MRI contrast agents. Relative to silica, synthetic polymer, or metallic nanoparticles, virus-like particles (VLPs) offer the advantages of monodispersity, high functionalizability, and high biodegradability.^{50-51, 53-56, 94} VLPs are self-assembled macromolecular structures composed of tens to thousands of individual protein subunits. The particular VLP utilized in this article is tobacco mosaic virus (TMV), a 300×18 nm rod-shaped plant virus with a protein capsid composed of 2130 identical coat proteins (**Figure 3.1**).⁶¹⁻⁶³ These coat proteins self-assemble around ssRNA. Each 17.5 kDa coat protein is composed of 158 amino acids, with three of these residues, E97, E106, and Y139, being solvent exposed and available for functionalization.⁶⁴⁻⁶⁷ The TMV rod contains a 4 nm pore along its axis of symmetry and is essentially the interior surface of TMV.^{63, 65} The glutamic acid residues line this interior surface and are electronically inaccessible to the exterior surface.⁶⁵⁻⁶⁷ The tyrosine residues line the exterior surface of TMV. The ease of synthetic modification and its resilience under a wide range of temperatures, solvents, and pH values have allowed TMV to function as a versatile platform in VLP technology for applications involving biomedicine and stimulus-responsive materials.

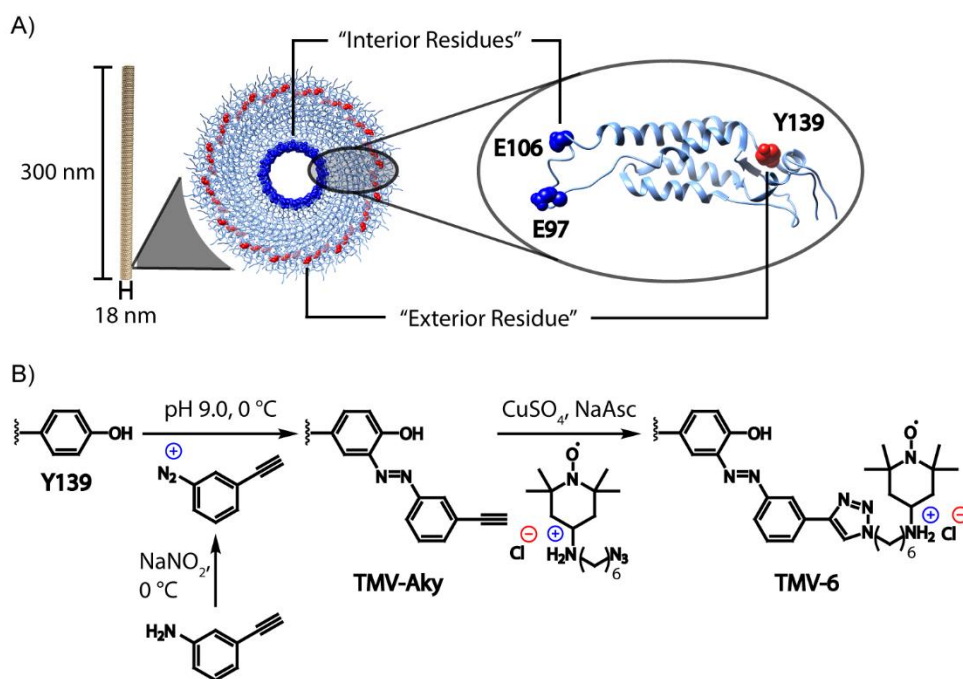


Figure 3.1. (A) Structure of TMV highlighting the solvent exposed amino acid residues of a single coat protein. (B) Installation of alkyne functionality on Y139 via diazonium coupling followed by the conjugation of **6-HCl** via CuAAC.

The exposed tyrosine residues on the exterior surface of TMV were utilized for the conjugation of aminoxyl moieties owing to their greater access to bulk water relative to the interior glutamic acid residues. We designed a derivative of the aminoxyl radical TEMPO, deemed **6**, (**Figure 3.2**) featuring an ammonium (upon protonation of the amine) for enhanced binding of cucurbit[8]uril (CB[8]). Various derivatives of TEMPO have been shown¹⁴⁰⁻¹⁴⁴ to bind CB[8] and the installation of the amine in **6** was predicted to offer enhanced binding through an extra ion-dipole interaction. Prior to the conjugation of **6-HCl** to TMV, the binding of **6-HCl** to CB[8] was probed via isothermal titration calorimetry (ITC) (**Figure 3.3**). The K_d value for the CB[8]⊃**6** complex was determined to be $1.5 \pm 0.1 \times 10^{-8}$ M, meaning that a reasonable fraction of a **6** and CB[8] mixture would exist as a complex under concentrations relevant for MRI contrast agents.

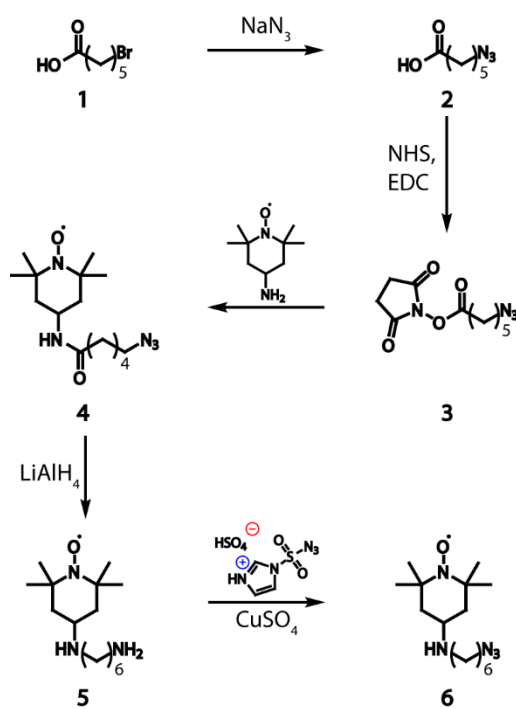


Figure 3.2. Synthesis of **6**.

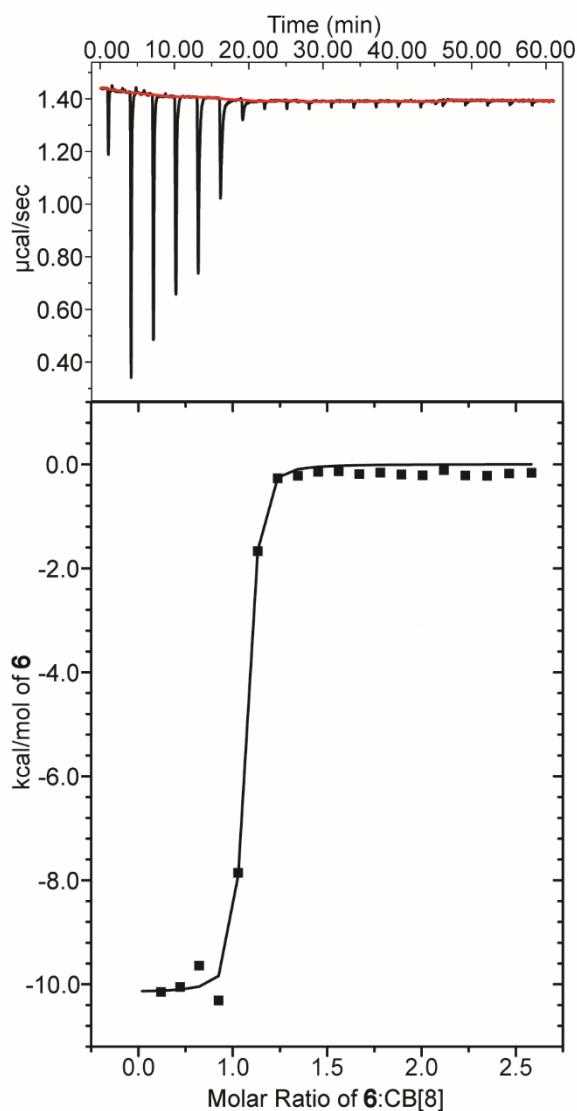


Figure 3.3. ITC data for **6** at 25 °C in 10 mM sodium phosphate (pH 7.0). **6** (250 μM) was titrated into a solution of CB[8] (50 μM). The top portion of the figure is a plot of power versus time. The bottom portion of the figure are integrated enthalpy values versus the molar ratio of **6**:CB[8]. The K_d value for the CB[8]⊃**6** complex was determined to be $1.5 \pm 0.1 \times 10^{-8}$ M. These data were fit to a sequential binding model using Origin 8.0 software.

Compound **6** was attached to TMV-Aky (**Figure 3.1**) via a copper-catalyzed azide-alkyne cycloaddition (CuAAC), yielding TMV-**6**. The conjugates TMV-Aky and TMV-**6** were confirmed and characterized (**Figure 3.4**) via transmission electron microscopy (TEM), electron spray ionization mass spectroscopy (ESI-MS), and size exclusion chromatography (SEC). ESI-MS confirmed quantitative conversions of the TMV coat proteins while TEM and SEC confirmed that the size and morphology of the TMV rods were effectively unaltered. Finally, the paramagnetism of the TMV-**6** conjugate was confirmed (**Figure 3.4**) via EPR spectroscopy. A triplet centered at a g -value of 2.007 and corresponding to ^{14}N ($I = 1$; $A \sim 45$ MHz) was observed for both the **6** small molecule and the TMV-**6** conjugate. The spectrum of **6** contains sharp peaks and isotropic g/A values that are characteristic of the rotational averaging found in small molecules. The spectrum of TMV-**6** contains broad peaks, anisotropic g/A values, and a lower S/N ratio relative to the spectrum of **6**. These differences between the spectra are attributed to the reduction of rotational and translational mobility upon attachment of **6** to the TMV rod. The high density of aminoxyl radicals on the surface of TMV can also allow for dipole spin exchange, which also results in peak broadening.

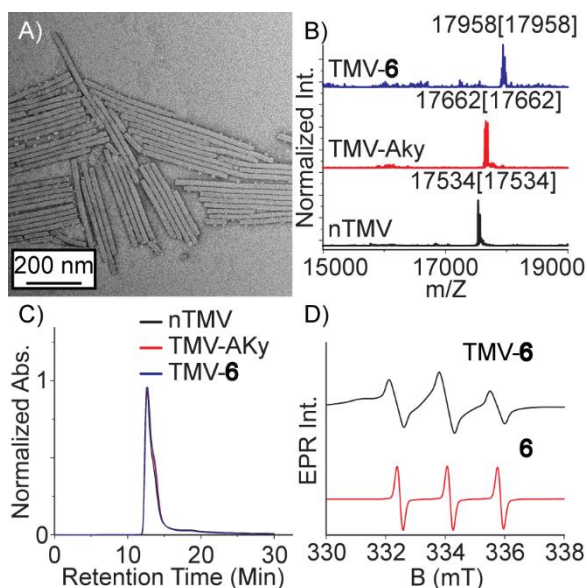


Figure 3.4. Characterization of TMV after bioconjugation reactions. (A) TEM image of TMV-6. (B) Bioconjugation of the TEMPO radical to TMV was confirmed via ESI-MS. The peak at 17534 m/z corresponds to native TMV. The peak at 17662 m/z corresponds to TMV-Aky. The peak at 17958 m/z corresponds to TMV-6. The spectrum corresponding to TMV-6 confirms complete conversion of TMV-Aky to TMV-6. (C) The integrity of the TMV rods after modification was confirmed by SEC. The single peak in the chromatograms (@260 nm) of the modified TMV samples demonstrates that the bioconjugation reactions did not compromise the morphology of the TMV rods. (D) X-band EPR spectra of **6** and TMV-6. The samples were prepared in capillary tubes to minimize interactions between high dielectric aqueous solvent and the electric field of the incident microwave radiation.

Since the properties of small molecules can change upon conjugation to proteins, we investigated the binding of CB[8] to TMV-6 following the confirmation of the TMV-6 conjugate. Since the solutions of TMV-6 at concentrations required for ITC characterization were subject to viscosity and adhesion issues, a fluorescence titration was used instead to determine a dissociation constant. In this case, neither TMV-6 nor CB[8] contain fluorophores, so a competitive binding strategy incorporating a fluorophore was implemented. Acridine-3,6-diamine, or Proflavin (PF), is an acridine derivative that is fluorescent as a free molecule in aqueous solutions, but its fluorescence becomes quenched¹⁴⁵⁻¹⁴⁶ upon binding inside the cavity of CB[8]. PF has been

reported¹⁴⁵ to bind CB[8] in a mostly 1:1 ratio with a K_d value of 5.3×10^{-8} M in aqueous solutions. These binding properties allow PF to feature as an appropriate fluorophore in a competitive binding fluorescence titration, assuming that **6** binds CB[8] with a similar motif and affinity even after conjugation to TMV.

A fluorescence titration featuring increasing concentrations of TMV-**6** (0-20 μ M in terms of TEMPO moieties) titrated into solutions with a constant concentration of the CB[8] \supset PF (0.2 μ M) complex was performed. The fluorescence of PF was induced with an excitation wavelength of 400 nm and measured at an emission wavelength of 510 nm. Upon the addition of increasing concentrations of TMV-**6**, the observed fluorescence of PF increased (**Figure 3.5**). This result is consistent with the fraction of PF in the solution bound to CB[8] decreasing due to the replacement of PF with TEMPO moieties. Since the fluorescence of the free PF molecules are no longer quenched by CB[8], observed fluorescence of PF will increase. Since no other significant interactions between TMV, **6**, CB[8], and PF were observed (**Figure B1**) and assuming the conservation of mass, the relationship and equilibria of the titration components can be described by the following equation:



Therefore, the two dissociation constants, K_a for the complex consisting of CB[8] and PF and K_b for the complex consisting of CB[8] and **6** can be represented by the following equations:

$$K_a = \frac{[\text{CB}[8]][\text{PF}]}{[\text{CB}[8] \cdot \text{PF}]} \quad (\text{Eq. 2})$$

$$K_b = \frac{[\text{CB}[8]][\text{6}]}{[\text{CB}[8] \cdot \text{6}]} \quad (\text{Eq. 3})$$

Equations 1-3 can then be combined to form the following cubic equation:

$$[\text{CB}[8]]^3 + a \cdot [\text{CB}[8]]^2 + b \cdot [\text{CB}[8]] + c = 0 \quad (\text{Eq. 4})$$

where

$$a = K_a + K_b + [\text{PF}]_0 + [\text{6}]_0 - [\text{CB}[8]]_0 \quad (\text{Eq. 5})$$

$$b = K_b([\text{PF}]_0 - [\text{CB}[8]]_0) + K_a([\text{6}]_0 - [\text{CB}[8]]_0) + K_a K_b \quad (\text{Eq. 6})$$

$$c = -K_a K_b [\text{CB}[8]]_0 \quad (\text{Eq. 7})$$

and $[\text{PF}]_0$, $[\text{6}]_0$, and $[\text{CB}[8]]_0$ denote the total concentration of each respective compound. The change in the observed fluorescence intensity can be directly linked to the binding constants K_a

and K_b by solving Equation 4 for the real root. The relationship between the observed fluorescence intensities and the binding constants are described by the equation:

$$F = F_{\text{Min}} + (F_{\text{Max}} - F_{\text{Min}}) \cdot \frac{2 \cdot \sqrt{(a^2 - 3b)} \cdot \cos \frac{\theta}{3} - a}{3K_a + \left[2 \cdot \sqrt{(a^2 - 3b)} \cdot \cos \frac{\theta}{3} - a \right]} \quad (\text{Eq. 8})$$

where

$$\theta = \cos^{-1} \frac{-2a^3 + 9ab - 27c}{2 \cdot \sqrt{(a^2 - 3b)}^3} \quad (\text{Eq. 9})$$

and F , F_{Min} , and F_{Max} denote the observed fluorescence intensity at any given point in the titration, the minimum observed fluorescence intensity during the titration, and the maximum observed fluorescence intensity during the titration, respectively. Upon fitting Equation 8 to the observed fluorescence intensities, the K_d value for the CB[8]⊃TMV-**6** complex was determined to be $3.8 \pm 0.5 \times 10^{-7}$ M. The reasons for the decreased binding affinity of the CB[8]⊃TMV-**6** complex relative to the CB[8]⊃**6** complex is not yet fully known, but several possible factors may explain this observation. One possible factor is the decreased access of CB[8] to conjugated TEMPO moieties owing to the fact that CB[8] can only approach conjugated TEMPO moieties from one direction versus the two directions of free TEMPO moieties. Another possibility is the presence of non-specific binding interactions between the exterior of CB[8] and the surfaces of TMV. A third possible factor is that CB[8] molecules can be temporarily trapped within the pore of TMV,

limiting their access to TEMPO moieties. Despite the binding affinity of the CB[8]⊃TMV-6 complex being lower than that of the CB[8]⊃6 complex, it is still high enough to be relevant for the purposes of the ORCA design. Taken as a whole, the fluorescence titration experiments suggest that CB[8] molecules can bind to the TEMPO moieties conjugated onto the exterior surface of TMV to form a pseudorotaxane.

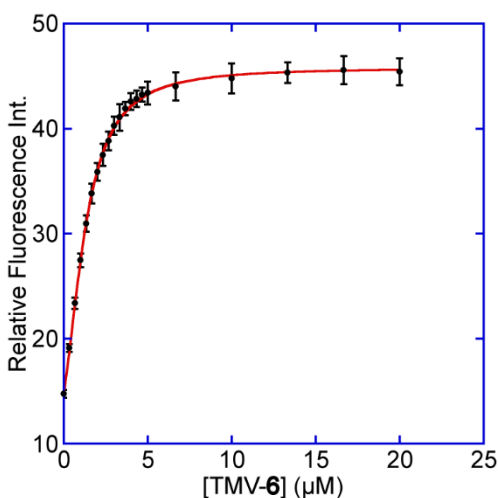


Figure 3.5. Fluorescence titration data for TMV-6. TMV-6 (0-20 μM in terms of TEMPO) was titrated into solutions of CB[8]⊃PF (0.2 μM). The K_d value for the CB[8]⊃TMV-6 complex was determined to be $3.8 \pm 0.5 \times 10^{-7}$ M.

After establishing that CB[8] can effectively bind to TMV-6 to form a pseudorotaxane, the relaxation behavior of the TEMPO moieties were characterized to determine the suitability of the pseudorotaxane as an ORCA, provided that the reduction of aminoxyl radicals does not occur. Relaxation behavior is dependent on several factors, with magnetic field strength and solvent exchange being major examples. Similar to metal-based contrast agents, aminoxyl radicals typically bind to at least one water molecule. The inner sphere of water molecules that interact

with the aminoxyl radicals provide major contributions to the overall proton relaxation behavior while the outer sphere water molecules provide only minor contributions. While maintaining a constant magnetic field strength of 1 T, longitudinal (T_1) and transverse (T_2) relaxation values were obtained for varying concentrations of TMV-**6** in the presence and absence of CB[8] (**Figure 3.6**). Relaxivity values (r_1 and r_2) were derived from a linear fit of the inverse relaxation data (**Table 3.1**). When compared to the small molecule TEMPO control, the TMV-**6** conjugate exhibits higher r_1 and r_2 relaxivity values. This trend is observed for the comparison between TMV-**6** in the presence of CB[8] and TEMPO-NH₂ in the presence of CB[8]. These observations are expected and explained by the limited molecular motion provided by the attachment of TEMPO moieties to TMV. Upon the addition of CB[8], a reduction in r_1 and r_2 relaxivity values is observed for both TMV-**6** and TEMPO-NH₂. This reduction in relaxivity values concurs with the understanding that the binding of CB[8] to a TEMPO moiety reduces solvent exchange by limiting the access of the aminoxyl radical by water molecules. The relaxivity values obtained by our experiments—which correlate with contrast strength—demonstrate that our pseudorotaxane can provide the contrast required to function as an ORCA. And although our pseudorotaxane provides inferior contrast compared to existing Gd-based contrast agents,¹³⁴ it is still far superior to small molecule aminoxyl radicals.

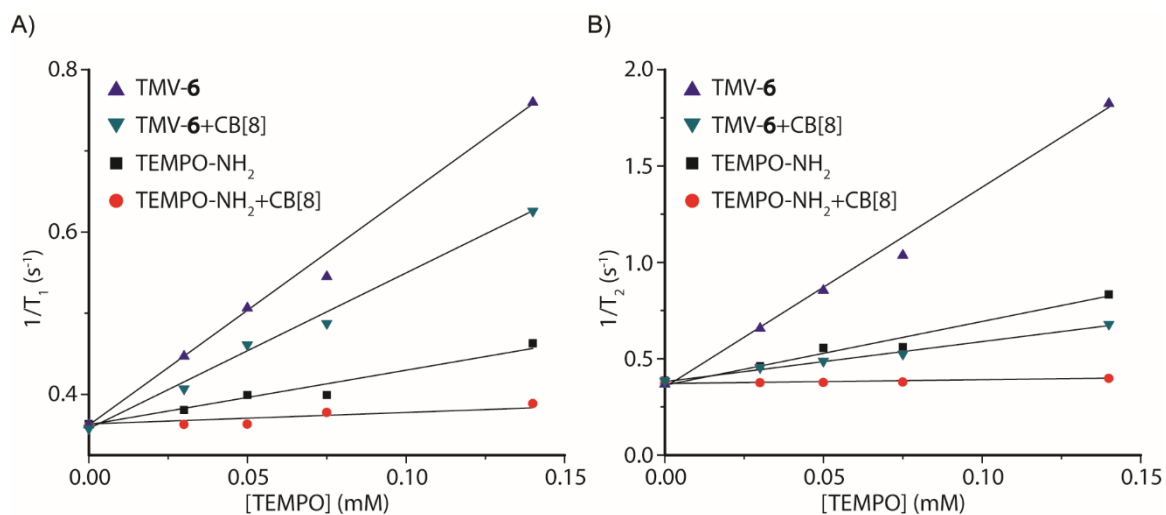


Figure 3.6. Plots of (A) $1/T_1$ (s^{-1}) and (B) $1/T_2$ (s^{-1}) versus [TEMPO] (mM) for TMV-6 and TEMPO-NH₂ in the absence and presence of CB[8] at 43 MHz in KP buffer (0.1 M, pH 7.4) @ 310 K.

Table 3.1. Comparison of relaxivity values between contrast agents.

Contrast Agent (CA)	CA per Particle	r_1 per CA ($mM^{-1} \cdot s^{-1}$)	r_2 per CA ($mM^{-1} \cdot s^{-1}$)	r_1 per Particle ($mM^{-1} \cdot s^{-1}$)	r_2 per Particle ($mM^{-1} \cdot s^{-1}$)	r_2 / r_1	Field (T)
TMV-6	~2130	2.8 ± 0.1	10.3 ± 0.1	~5964	~21939	3.7	1
TMV-6+CB[8]	~2130	1.9 ± 0.1	3.1 ± 0.1	~4047	~6603	1.6	1
TEMPO-NH ₂	1	0.6 ± 0.1	2.0 ± 0.1	0.6 ± 0.1	2.0 ± 0.1	3.3	1
TEMPO-NH ₂ +CB[8]	1	0.2 ± 0.1	0.2 ± 0.1	0.2 ± 0.1	0.2 ± 0.1	1	1
Gd-DOTA ¹³⁴	1	3.0	5.0	3.0	5.0	1.7	1.5

Having characterized the NMR relaxation properties of the pseudorotaxane and establishing its ability to function as an ORCA, we sought to investigate the shielding performance of the pseudorotaxane architecture. The rapid reduction of aminoxyl radicals to hydroxylamines in the presence of physiologically relevant reducing agents is well known. Ascorbate is one example of these reducing agents and is commonly utilized for reduction experiments due to its ubiquity in the human body and its extensively studied redox properties. Upon the addition of a sodium ascorbate (10 equivalents per TEMPO moiety) solution in KP buffer (0.1 M, pH 7.4) to solutions of TMV-**6** in the presence and absence of CB[8] (10 equivalents per TEMPO moiety), EPR spectra of the TMV conjugates were collected over 2 h (**Figure 3.7**). EPR intensities were fitted under pseudo-first-order conditions. The pseudo-first-order rate constant for the reduction of TEMPO, k' , was determined to be $2.0 \pm 0.1 \times 10^{-5} \text{ s}^{-1}$ for TMV-**6** in the presence of CB[8] and $16 \pm 0.1 \times 10^{-4} \text{ s}^{-1}$ for TMV-**6** in the absence of CB[8]. The rate of reduction of the pseudorotaxane is far lower than that of not only the unshielded TMV-**6**, but all aminoxyl-based ORCAs we currently know of. The substantial decrease in the reduction rate of TEMPO suggests strongly that the CB[8] in the pseudorotaxane architecture effectively shields the aminoxyl radical from ascorbate.

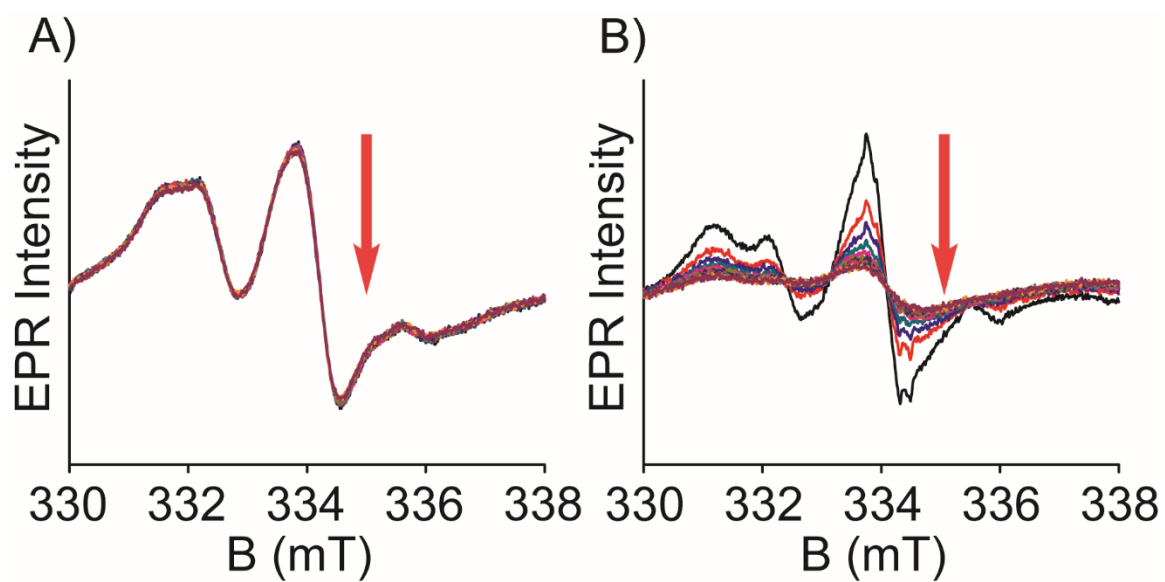


Figure 3.7. EPR spectra for the reduction of TMV-6 (2.6 mg/mL) with sodium ascorbate (10 equivalents per TEMPO moiety) in the (A) presence (10 equivalents per TEMPO moiety) and (B) absence of CB[8]. Data were collected at 10 min intervals over 2 h.

3.3 Conclusions

We have demonstrated the enhancement of the survivability of aminoxyl radicals in the presence of ascorbate via shielding with CB[8]. The attachment of TEMPO derivatives onto the exterior surface of TMV results in a conjugate that provides enhanced T_1 and T_2 relaxation properties relative to small molecule aminoxyl radicals. The addition of CB[8] to the TMV conjugate forms a pseudorotaxane ORCA where the TEMPO moieties are encaged by CB[8]. The CB[8] can sterically shield the aminoxyl radical from reduction by ascorbate while still allowing for the exchange of water. Although the CB[8] also reduces the contrast strength of the ORCA compared to its unshielded form, the contrast strength is still higher than that of small molecule aminoxyl radicals. Most importantly, the ORCA can survive for greatly extended periods of time compared to all other aminoxyl-based ORCAs we currently know of. Our results show that aminoxyl-based ORCAs still have plenty of room for improvement. They also show that utilizing macrocycles for the steric shielding of aminoxyl radicals is a highly promising strategy for extending the lifetime of aminoxyl-based ORCAs to clinically viable values.

Materials, instrumentation, experimental methods, and supporting information can be found in **Appendix B**.

CHAPTER 4

PERSISTENT AMINOXYL ORCAS UTILIZING A ROTAXANE ARCHITECTURE FOR SHIELDING

4.1 Introduction

The previous chapter explained the clinical significance of magnetic resonance imaging (MRI), the importance of gadolinium (Gd) in MRI contrast agents, and the need for metal-free contrast agents. The difficulties in designing clinically viable versions of such contrast agents were also discussed. To summarize, organic radical contrast agents (ORCA) based on paramagnetic aminoxyl moieties, show significant promise in eventually replacing Gd-based contrast agents. However, two major issues prevent aminoxyl-based ORCAs from replacing traditional contrast agents based on Gd: *(i)* their single unpaired electron provides weaker contrast compared to the seven unpaired electrons of Gd and *(ii)* they are easily reduced to MRI-silent hydroxylamines in physiological conditions by compounds including ascorbate, saccharides, and cysteine-rich proteins. In an attempt to address these issues, we designed an ORCA composed of the following: *(i)* TEMPO derivatives conjugated to the exterior surface of tobacco mosaic virus (TMV) and *(ii)* the macrocycle cucurbit[8]uril (CB[8]), which encaged the TEMPO moieties to form a pseudorotaxane. The ORCA provided enhanced relaxivity values relative to small molecule aminoxyl radicals and the pseudorotaxane architecture proved to be extremely effective at shielding the aminoxyl radical from reduction by ascorbate. Kinetics experiments measuring the reduction rate of our ORCA in the presence of ascorbate demonstrated that this shielding and enhanced survivability of aminoxyl radicals resulted in lifetimes that were clinically viable.

While the ORCA described above appears to successfully address the issues plaguing the design of clinically viable aminoxyl-based ORCAs, one glaring issue eliminates the possibility of that ORCA from becoming clinically viable: the ORCA utilizes a pseudorotaxane architecture for shielding. By definition, pseudorotaxanes are not mechanically interlocked molecular architectures.¹⁴⁷⁻¹⁴⁸ This means that CB[8] can slide off the TEMPO moiety, resulting in a situation where CB[8], the TMV-TEMPO conjugate, and the complex between CB[8] and TMV-TEMPO are in equilibrium with each other. Unless CB[8] constantly exists in the body at a concentration such that all TEMPO moieties are bound to CB[8], the pseudorotaxane will quickly dissociate, leaving behind an unshielded ORCA. One solution to this issue is to utilize a true rotaxane to shield the aminoxyl radical. An aminoxyl-based ORCA utilizing a true rotaxane for shielding is a mechanically interlocked molecular architecture, and the relevant macrocycle would not be able to dissociate from the aminoxyl radical without breaking covalent bonds. We have decided to pursue the strategy of utilizing a rotaxane architecture in hopes of creating a persistent ORCA based on aminoxyl radicals.

The following sections of this chapter will describe our efforts to design and fabricate an aminoxyl ORCA utilizing a rotaxane architecture to shield the aminoxyl radical. The characterization plans following the synthesis of the rotaxane ORCA will also be discussed.

4.2 Results and Discussion

The design of our rotaxane ORCA consists of a thread that contains the aminoxyl radical, a macrocycle to encage the aminoxyl radical, and stoppers that prevent dissociation of the macrocycle from the thread. The aminoxyl radical TEMPO utilized in the previous chapter was considered for use in the thread of the rotaxane, but was not chosen. This is because of the difficulty in establishing a synthetic route that would allow the installation of the functionality required to complete the thread such that CB[8] could still bind to the TEMPO moiety. Examination of other stable aminoxyl radicals that were available revealed that PROXYL, a pyrrolidine version of TEMPO, was small enough to be encaged by CB[8] while still fulfilling the other requirements of the thread (**Figure 4.1**). Having chosen PROXYL as the base aminoxyl radical for the thread and CB[8] as the macrocycle, it was determined that the presence of cationic ammonium moieties on both sides of the PROXYL moiety would be beneficial in directing CB[8] around the thread during the assembly of the rotaxane. The ends of the thread required functionality that would allow for the installation of the stopper molecules. The azide functionality was chosen for this purpose owing to the versatility and reliability of the copper-catalyzed azide-alkyne cycloaddition (CuAAC) reaction. The thread also needed to be long enough such that steric occlusion would not prevent the installation of the stopper molecules. Finally, the stopper molecules would need to be large and rigid such that they prevent the possibility of CB[8] sliding past them without breaking covalent bonds. A derivative of the fluorescent dye Texas Red (TXR) was chosen owing to its ability to fulfill the requirements as a stopper molecule and its alkyne functionality, not its spectroscopic properties.

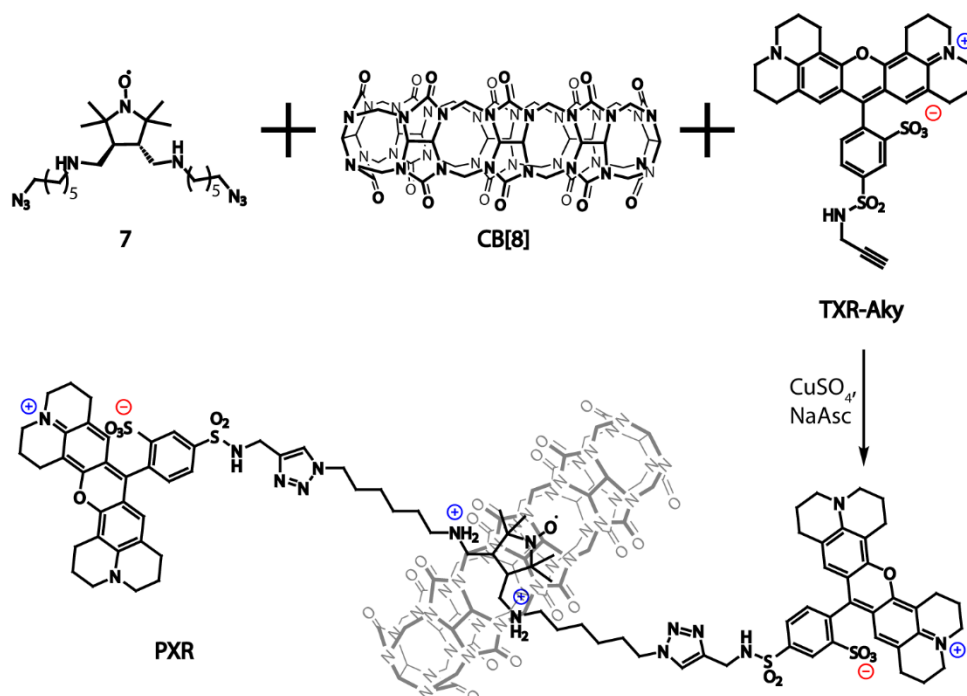


Figure 4.1. Synthesis of **PXR**.

Analysis of the available PROXYL derivatives led to the construction of the synthesis route shown in **Figure 4.2** and characterization of the products along each step of the synthesis can be found in **Appendix C**. Synthesis of the final PROXYL thread has not been completed at the time of this writing. A major issue encountered while working towards the synthesis of **7** was the difficulty in obtaining high yields of **5** and **6**. Access of the carbonyl moieties introduced in **4** was much more difficult than originally anticipated. The geometry of the five-membered ring of PROXYL combined with the fact that the carbonyl groups are adjacent to each other resulted in a highly sterically hindered system. Different reaction conditions are still being investigated to optimize the synthesis of **5** and **6**.

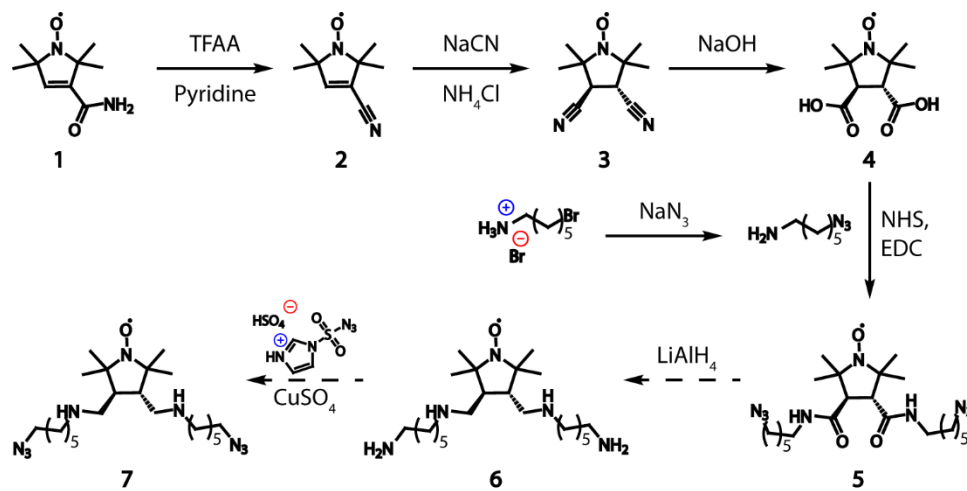


Figure 4.2. Synthesis of 7.

Upon the synthesis and isolation of **PXR**, its paramagnetic properties and effectiveness as an ORCA will need to be characterized. The paramagnetic properties of **PXR** will be characterized by obtaining its EPR spectrum. If distinctive the peak patterns of aminoxyl radicals at 334 mT are observed, then the paramagnetic activity of **PXR** can be confirmed. NMR relaxation experiments will be used to characterize the T_1 and T_2 relaxation properties, the resulting relaxivity values of **PXR**, and the ability of **PXR** to function as a contrast agent. If **PXR** is found to be able to function as a contrast agent, a solution of sodium ascorbate (10 equivalents per PROXYL moiety) solution in KP buffer (0.1 M, pH 7.4) will be added to a solution of **PXR** and its EPR spectra will be collected over 2 h. The EPR intensities will be fitted under pseudo-first-order conditions to determine the pseudo-first-order rate constant for the reduction of PROXYL, k' . The results of the reduction kinetics experiments will determine if the rotaxane architecture is effective at shielding aminoxyl radicals and if **PXR** can function as a persistent aminoxyl ORCA.

4.3 Conclusions

Although the rotaxane **PXR** has not yet been obtained, progress is being made towards its synthesis. Characterization of **PXR** to determine its suitability as a persistent aminoxyl ORCA will follow its isolation.

Materials, instrumentation, experimental methods, and supporting information can be found in **Appendix C**.

CHAPTER 5

SUMMARY OF FINDINGS AND FUTURE DIRECTIONS

5.1 SUMMARY OF FINDINGS

Functional materials are essential to modern life as we know it. Countless applications rely on functional materials to respond to the many external stimuli that stem from the mere existence of this world. To study all the currently known functional materials and the regulation of their stimulus responses in this lifetime would be impossible. However, I am fortunate enough to have been able to contribute to humanity's struggle to better understand and improve the world around us. My findings thus far have been distilled into this dissertation. The work discussed in this dissertation is focused on understanding, designing, and regulating pH- and redox-responsive materials. Chapter 2 of this dissertation discussed the development of a pH-responsive VLP that was able to be internalized by certain cell lines only when exposure to acidic conditions had released the moieties present on the surface of the VLP that were inhibiting its uptake. Chapters 3 and 4 of this dissertation discussed the development of aminoxyl-based ORCAs for MRI that resisted reduction by ascorbate. Experimental results obtained during the course of developing these pH- and redox-responsive materials revealed that although none of the developed materials are ready for their intended applications, new understanding had been gained that could spur the progress of their respective fields.

5.2 FUTURE DIRECTIONS

While the ultimate goal of both the pH- and redox-responsive materials covered in Chapters 2-4 of this dissertation involve clinical applications, there is a long way to go before this goal is achieved. Whether this goal is eventually achieved or not, there is still much to learn about the pH- and redox-responsive materials that have been discussed in the previous chapters. Concerning the pH-responsive VLP from Chapter 2, there are many other linker designs that could be built between the surface of Q β and the terminal carboxylate moieties and investigating the effects of these different linkers would provide a more comprehensive understanding of the mechanisms behind cell uptake. Attaching the existing linkers and terminal carboxylate moieties on different scaffolds would also elucidate whether the observations described in Chapter 2 only apply to nanoparticles using VLPs, or even specifically Q β as a scaffold. Concerning the aminoxyl-based ORCAs from Chapters 3 and 4, the use of different aminoxyl radicals or macrocycles in the construction of a rotaxane-based shielding system would be worth investigating. The use of different rotaxane components would allow the tuning of synthetic feasibility, immune response, relaxivity, organ targeting, and many more important factors that are considered when designing ORCAs in general.

APPENDIX A

SUPPORTING INFORMATION FOR CHAPTER 2

MATERIALS

All chemicals were purchased from Sigma-Aldrich (St. Louis, MO), ThermoFisher Scientific (Pittsburgh, PA), Alfa Aesar (Ward Hill, MA), or TCI America (Portland, OR) and used without further purification.

INSTRUMENTATION

^1H and ^{13}C NMR spectra were obtained using a 600 MHz Bruker Avance NMR spectrometer with residual solvent peaks as a reference for all NMR spectra. MALDI-TOF MS were acquired using a Shimadzu AXIMA Confidence MALDI-TOF MS. ESI-MS were acquired using a Waters M-class UPLC with a RP C4 BEH column for separation and a Waters Synapt G2-Si for detection. Dynamic light scattering (DLS) was conducted using a Malvern Zetasizer Nano ZS molecular size analyzer. Transmission electron microscopy (TEM) was conducted using a JEOL JEM-1400Plus transmission electron microscope. Fluorescence data were obtained using a Horiba Fluorolog-3 steady state spectrofluorometer with a Horiba iHR320 imaging spectrometer. Epifluorescence microscopy was performed using a Life Technologies EVOS FL Auto Epifluorescence microscope. Flow cytometry was performed using a BD LSRFortessa™ flow cytometer.

SYNTHESIS

Synthesis of 6-Azidohexanoic acid

6-Bromohexanoic acid (5.0 g, 25.6 mmol), and NaN_3 (4.998 g, 76.9 mmol) were stirred in DMF (20 mL) at 85 °C overnight. Upon cooling the reaction to RT, DCM (40 mL) was added to the reaction mixture and stirred. The reaction mixture was then washed with aqueous HCl (0.1 M, 3×20 mL) and dried with MgSO_4 . The organic fraction was isolated and the solvent was removed under reduced pressure to yield the product as a clear pale yellow oil. ^1H NMR (600 MHz, CDCl_3) δ ppm 1.43 (quint, $J = 7.2$ Hz, 2 H) 1.61 (quint, $J = 7.2$ Hz, 2 H) 1.67 (t, $J = 7.2$ Hz, 2H) 2.37 (quint, $J = 7.2$ Hz, 2H) 3.27 (t, $J = 6.4$ Hz, 2 H).

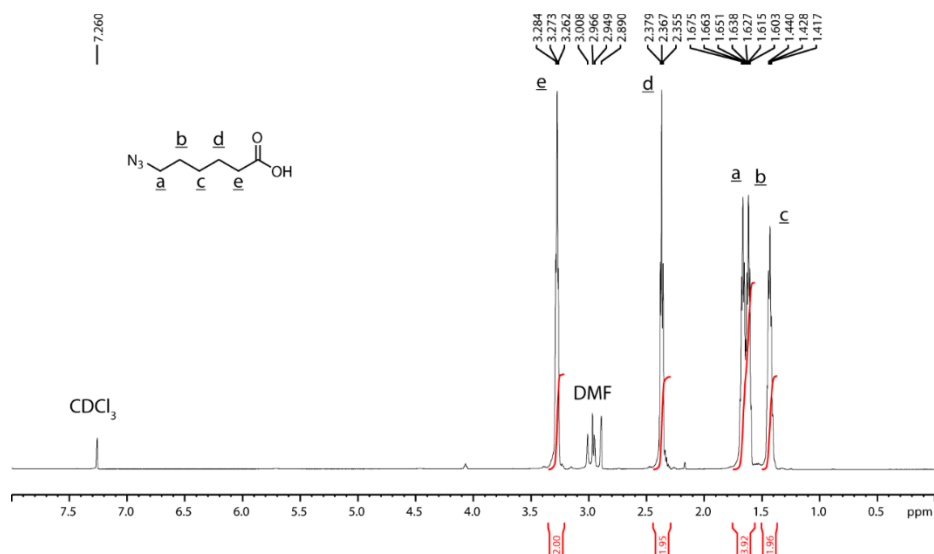


Figure A1. ^1H NMR spectrum of 6-azidohexanoic acid.

Synthesis of 2,5-Dioxopyrrolidin-1-yl 6-azidohexanoate

6-Azidohexanoic acid (2.0 g, 12.7 mmol), *N*-hydroxysuccinimide (NHS) (4.395 g, 38.2 mmol), and 1-ethyl-3-(3-dimethylaminopropyl)carbodiimide (EDC) (5.929 g, 38.2 mmol) were dissolved in DMF (15 mL) and stirred at RT, 48 h. DMF was then removed under reduced pressure. The remaining residue was dissolved in ethyl acetate (EtOAc) (25 mL). The organic layer was washed with H₂O (3×40 mL), saturated brine (3×40 mL), and dried with MgSO₄. The solvent was removed under reduced pressure to yield the crude product. The crude product was further purified via column chromatography (silica gel) with Hexanes:EtOAc (100:0-0:100). The fractions corresponding to the product were combined and the solvent was removed under reduced pressure to yield the product as a clear pale yellow oil. ¹H NMR (600 MHz, CDCl₃) δ ppm 1.49 (quint, J = 6.8 Hz, 2 H) 1.63 (quint, J = 7.1 Hz, 2 H) 1.77 (t, J = 7.0 Hz, 2 H) 2.61 (quint, J = 7.1 Hz, 2 H) 2.82 (s, 4 H) 3.28 (t, J = 6.4 Hz, 2 H).

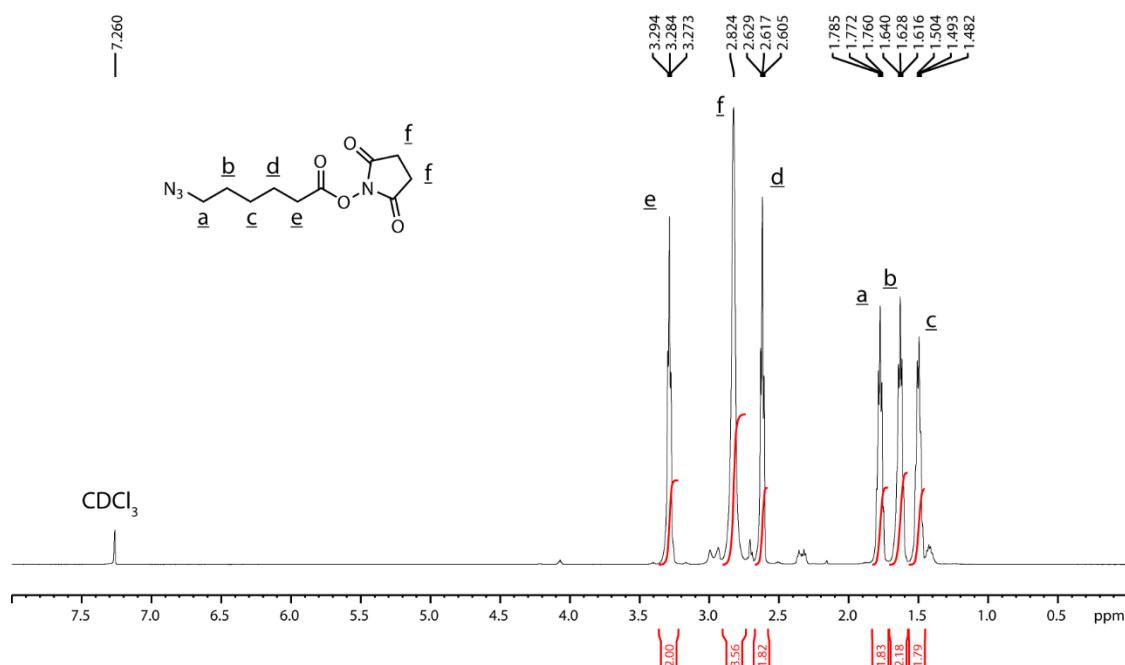


Figure A2. ¹H NMR spectrum of 2,5-dioxopyrrolidin-1-yl 6-azidohexanoate.

Synthesis of 6-(Prop-2-yn-1-yloxy)hexanoic acid

6-Bromohexanoic acid (2.0 g, 10.3 mmol), propargyl alcohol (11.492 g, 205 mmol), and KOH (1.725 g, 16.4 mmol) were mixed and stirred at 65 °C, 48 h. Upon cooling the reaction to RT, propargyl alcohol was removed under reduced pressure. Aqueous HCl (6 M, 40 mL) was added to the remaining residue and mixed. The reaction product was then extracted with DCM (3×20 mL) and the solvent removed under reduced pressure to yield the product as a clear pale yellow oil. ¹H NMR (600 MHz, CDCl₃) δ ppm 1.46 (quint, J = 7.8 Hz, 2 H) 1.65 (quint, J = 7.8 Hz, 2 H) 1.70 (quint, J = 7.8 Hz, 2 H) 2.40 (t, J = 7.2 Hz, 2 H) 2.45 (d, J = 2.4 Hz, 1 H) 3.56 (t, J = 6.4 Hz, 2 H) 4.17 (d, J = 1.9 Hz, 2 H).

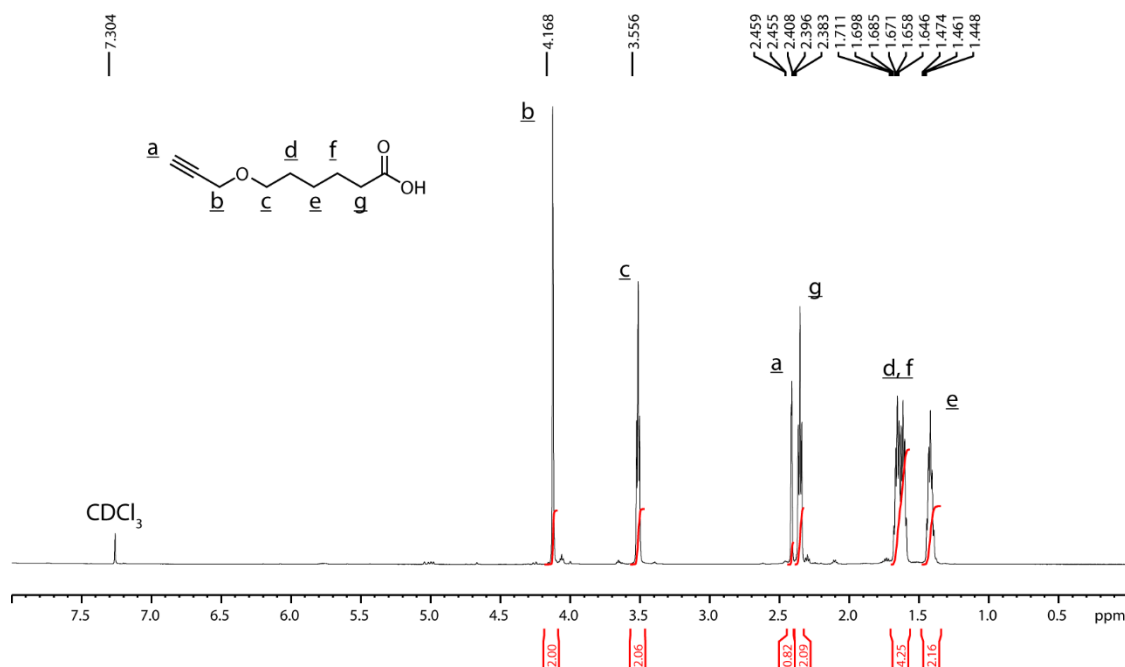


Figure A3. ¹H NMR spectrum of 6-(prop-2-yn-1-yloxy)hexanoic acid.

Synthesis of Tris(2,5-dioxopyrrolidin-1-yl) benzene-1,3,5-tricarboxylate

Trimesic acid (0.5 g, 4.759 mmol), NHS (1.642 g, 14.277 mmol), and EDC (2.216 g, 14.277 mmol) were stirred in DMF (10 mL) at RT overnight. The solvent was removed under reduced pressure to yield a thick golden residue. The residue was dissolved in acetone (15 mL). The resulting solution was added to an aqueous solution of HCl (1 M, 200 mL). A white solid precipitated out of the solution. The solid was filtered, washed with H₂O (50 mL), and hot 2-propanol (50 mL). The resulting white solid was dried under high vacuum at RT overnight. ¹H NMR (600 MHz, CDCl₃) δ ppm 2.94 (s, 12 H) 9.14 (s, 3 H).

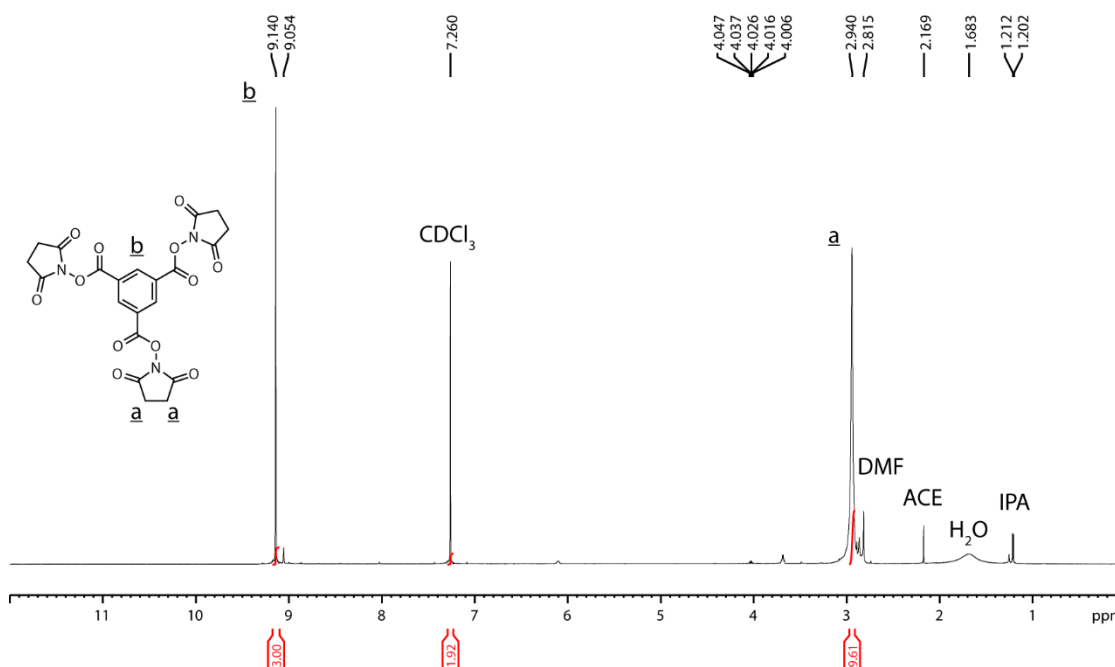


Figure A4. ^1H NMR spectrum of tris(2,5-dioxopyrrolidin-1-yl) benzene-1,3,5-tricarboxylate.

Synthesis of 6-Hydrazinonicotinic acid

6-Chloronicotinic acid (2.0 g, 12.7 mmol) was dissolved in hydrazine hydrate (12.2 g, 190.5 mmol, 11.8 mL) and stirred at 100 °C, 5 h. HCl (2 mL) was added to the reaction mixture to quench the reaction. The solvent was removed under reduced pressure. The remaining residue was dissolved in H₂O (50 mL). HCl was added until the mixture reached pH 5. The precipitate was isolated via vacuum filtration and the feed was washed with cold 2-propanol. The feed was left to dry until a pale yellow solid remained. ^1H NMR (600 MHz, DMSO) δ ppm 6.70 (d, J = 8.5 Hz, 1 H) 7.85 (d, J = 8.8 Hz, 1 H) 8.28 (s, 1 H) 8.52 (s, 1 H).

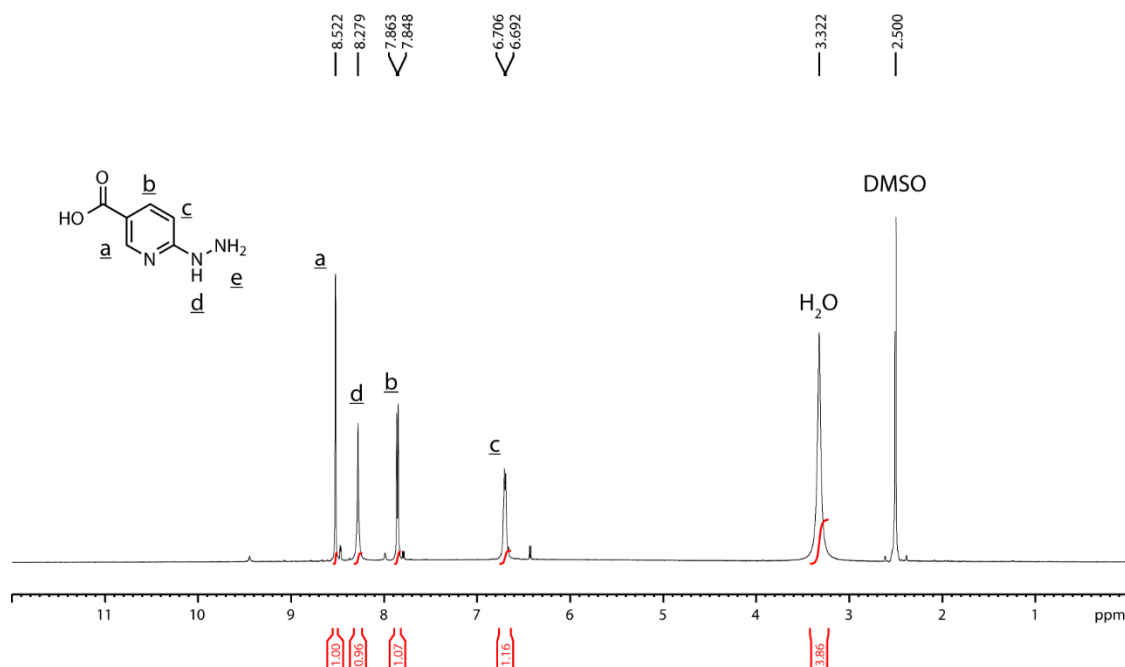


Figure A5. ¹H NMR spectrum of 6-hydrazinonicotinic acid.

Synthesis of 1-Azidopropan-2-one

Chloroacetone (2.0 g, 21.6 mmol), and NaN₃ (4.216 g, 64.8 mmol) were stirred in acetone (50 mL) at RT, 24 h. The reaction mixture was then filtered and the filtrate was isolated. The feed was washed with acetone and the filtrate from the wash was isolated. The filtrate fractions were combined and the solvent was removed under reduced pressure. The resulting oil was diluted with diethyl ether (50 mL) and washed with H₂O (2×15 mL). The organic fraction was isolated and dried with MgSO₄. The solvent was removed under reduced pressure to obtain the product as a clear pale yellow liquid. ¹H NMR (600 MHz, CDCl₃) δ ppm 2.18 (s, 3 H) 3.94 (s, 2 H).

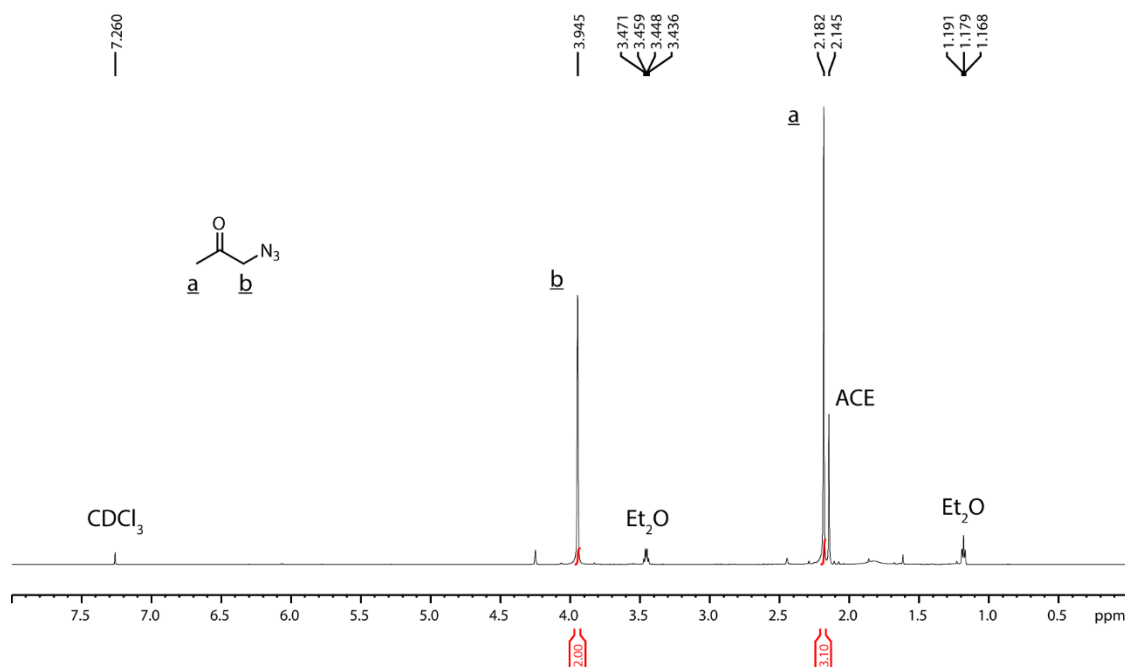


Figure A6. ¹H NMR spectrum of 1-azidopropan-2-one.

Synthesis of 2,5-Dioxopyrrolodin-1-yl 6-(2-(1-azidopropan-2-ylidene)hydrazinyl)nicotinate

6-Hydrazinyl nicotinic acid HCl (0.5 g, 2.6 mmol), 1-azidopropan-2-one (4 g, 68.9 mmol), and TEA (0.25 g, 2.5 mmol) were dissolved in dry DMF (10 mL). Potassium carbonate (0.729 g, 5.3 mmol) was added and the mixture was stirred at RT overnight. NHS (0.910 g, 7.9 mmol) and EDC (1.228 g, 7.9 mmol) were dissolved in the reaction mixture and the mixture was stirred at RT overnight. Some of the solvent was removed under reduced pressure. CHCl₃ (30 mL) was added and the reaction mixture was washed with H₂O (3×25 mL). The aqueous layer was extracted with CHCl₃ (2×25 mL) and the organic layers were combined. The organic layer was washed with H₂O (3×20 mL), saturated brine (3×20 mL), and dried with MgSO₄. The solvent was removed under reduced pressure to yield the crude product. The crude product was further purified via column chromatography (silica gel) with DCM:MeOH (100:0-90:10). The fractions corresponding to the

product were combined and the solvent was removed under reduced pressure. The resulting product was redissolved in DCM (30 mL), washed with saturated brine (3×20 mL), and dried with MgSO₄. The solvent was removed under reduced pressure to yield the product as a brown solid.

¹H NMR (600 MHz, DMSO) δ ppm 2.02 (s, 3 H) 2.88 (s, 4 H) 4.07 (s, 2 H) 7.26 (d, J = 8.8 Hz, 1 H) 8.20 (d, J = 8.9 Hz, 1 H) 8.82 (s, 1 H) 10.72 (s, 1 H). ¹³C NMR (150 MHz, DMSO) δ ppm 14.85, 25.51, 55.25, 106.32, 110.97, 139.15, 148.33, 151.50, 160.87, 161.13, 170.48.

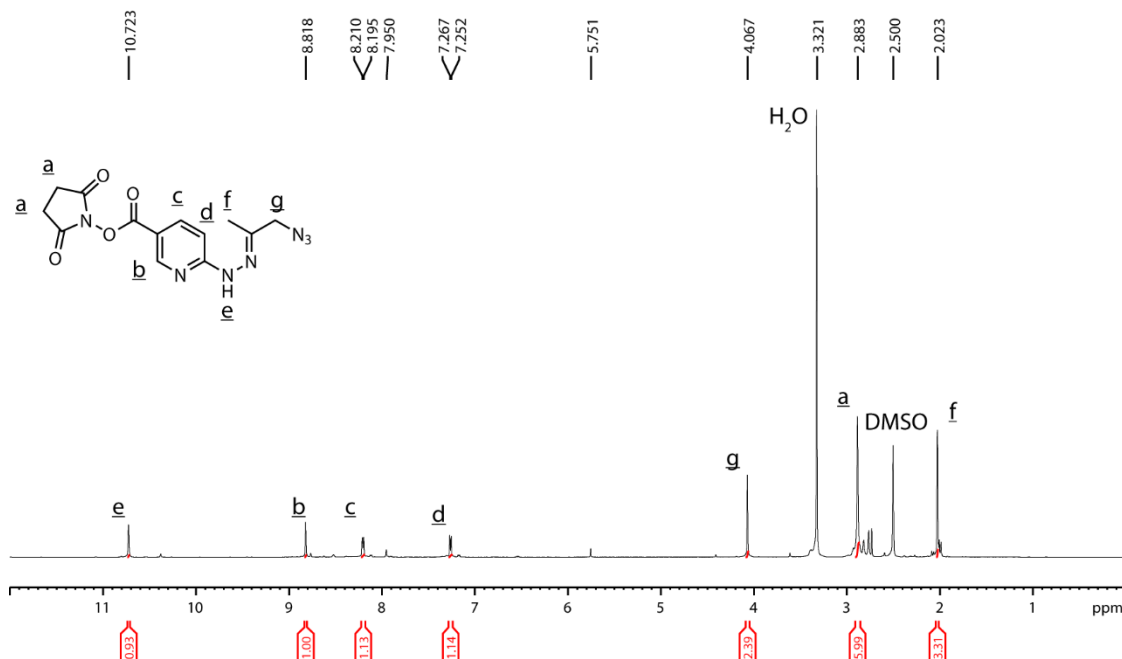


Figure A7. ¹H NMR spectrum of 2,5-dioxopyrrolodin-1-yl 6-(2-(1-azidopropan-2-ylidene)hydrazinyl)nicotinate.

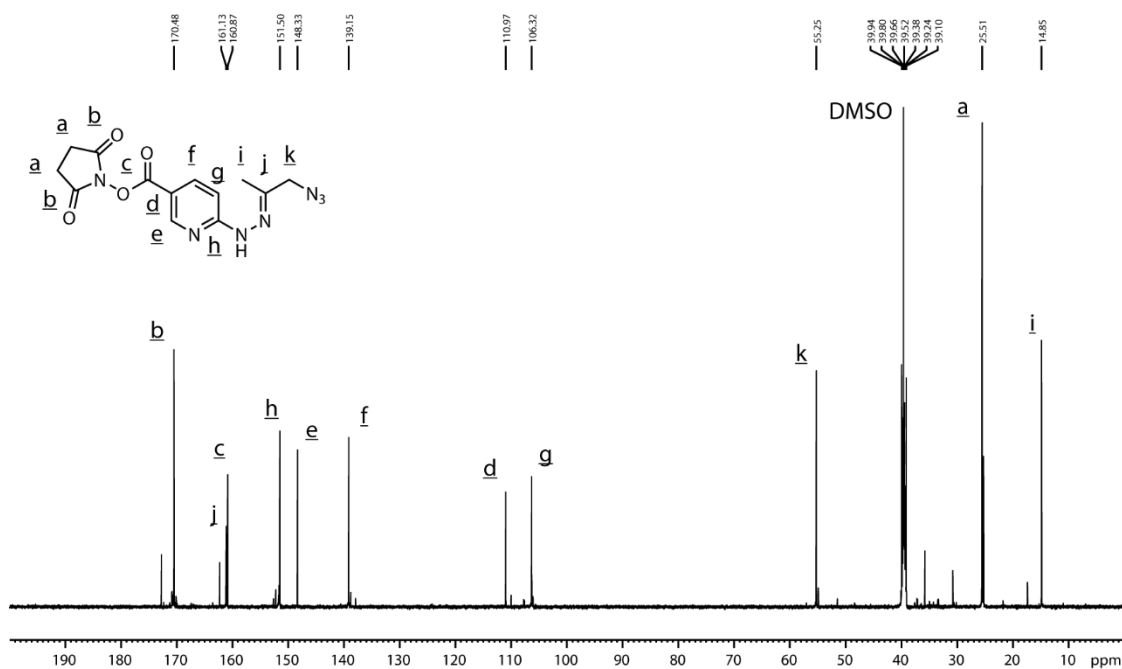


Figure A8. ^{13}C NMR spectrum of 2,5-dioxopyrrolodin-1-yl 6-(2-(1-azidopropan-2-ylidene)hydrazinyl)nicotinate.

Synthesis of 5-Azidopentan-2-one

5-Chloropentan-2-one (4.0 g, 33.2 mmol), and NaN_3 (6.469 g, 99.5 mmol) were stirred in DMF (50 mL) at 60 °C, 24 h. Upon cooling the reaction to RT, H_2O (20 mL) and EtOAc (40 mL) were added to the reaction mixture and stirred. The organic fraction was isolated and dried with MgSO_4 . The solvent was removed under reduced pressure to yield a black liquid. ^1H NMR (600 MHz, CDCl_3) δ ppm 1.82 (quint, $J = 6.7$ Hz, 2 H) 2.12 (s, 3 H) 2.51 (t, $J = 7.0$ Hz, 2 H) 3.28 (t, $J = 6.5$ Hz, 2 H).

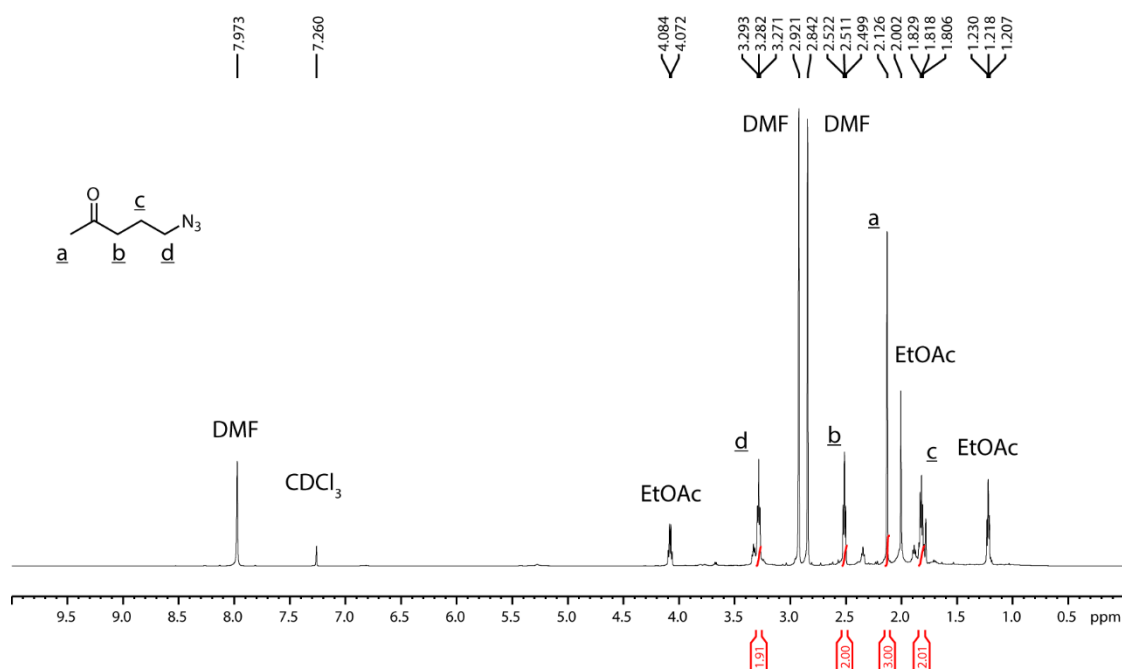


Figure A9. ¹H NMR spectrum of 5-azidopentan-2-one.

Synthesis of 2,5-Dioxopyrrolodin-1-yl 6-(2-(5-azidopentan-2-ylidene)hydrazinyl)nicotinate

6-Hydrazinyl nicotinic acid HCl (0.5 g, 2.6 mmol), 5-azidopentan-2-one (4 g, 31.5 mmol), and triethylamine (TEA) (0.25 g, 2.5 mmol) were dissolved in dry (need not be anhydrous) DMF (10 mL). Potassium carbonate (0.729 g, 5.3 mmol) was added and the mixture was stirred at RT overnight. NHS (0.910 g, 7.9 mmol) and EDC (1.228 g, 7.9 mmol) were dissolved in the reaction mixture and the mixture was stirred at RT overnight. Some of the solvent was removed under reduced pressure. CHCl₃ (30 mL) was added and the reaction mixture was washed with H₂O (3×25 mL). The aqueous layer was extracted with CHCl₃ (2×25 mL) and the organic layers were combined. The organic layer was washed with H₂O (3×20 mL), saturated brine (3×20 mL), and dried with MgSO₄. The solvent was removed under reduced pressure to yield the crude product. The crude product was further purified via column chromatography (silica gel) with DCM:MeOH

(100:0-90:10). The fractions corresponding to the product were combined and the solvent was removed under reduced pressure. The resulting product was redissolved in DCM (30 mL), washed with saturated brine (3×20 mL), and dried with MgSO₄. The solvent was removed under reduced pressure to yield the product as a thick brown liquid. ¹H NMR (600 MHz, DMSO) δ ppm 1.83 (quint, J = 6.7 Hz, 2 H) 1.99 (s, 3 H) 2.36 (t, J = 6.7 Hz, 2 H) 2.89 (s, 4 H) 3.39 (t, J = 5.3 Hz, 2 H) 7.18 (d, J = 8.9 Hz, 1 H) 8.13 (d, J = 8.7 Hz, 1 H) 8.78 (s, 1 H). ¹³C NMR (150 MHz, DMSO) δ ppm 16.38, 25.26, 35.41, 50.36, 54.86, 106.16, 110.26, 138.82, 151.63, 153.58, 160.96, 161.23, 170.50, 172.75.

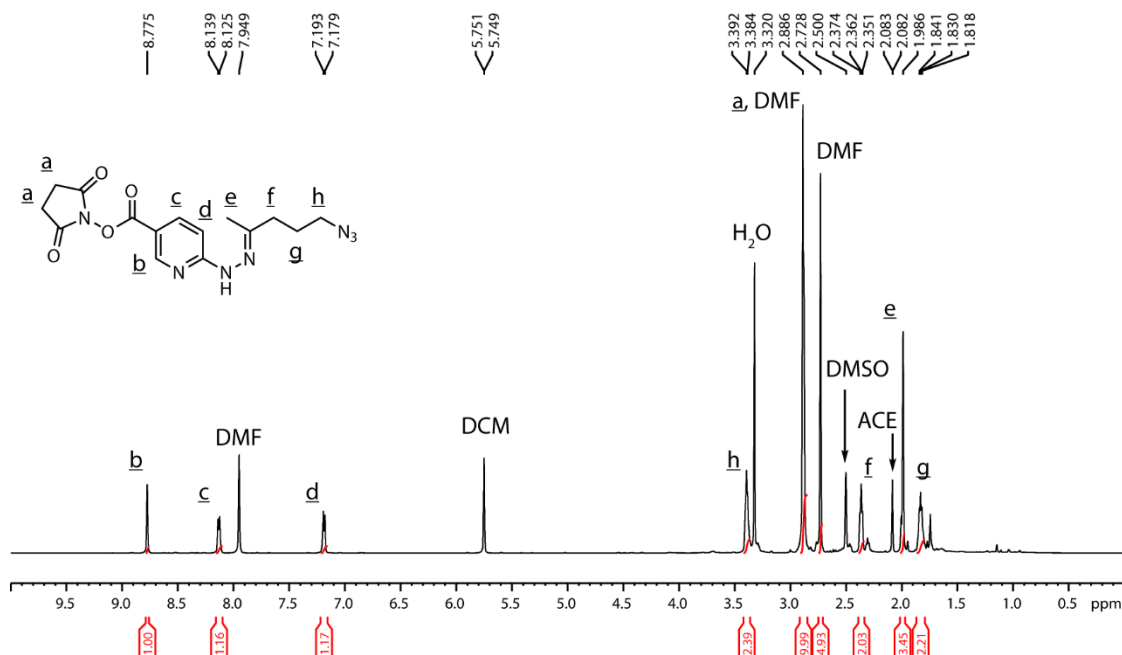


Figure A10. ¹H NMR spectrum of 2,5-dioxopyrrolidin-1-yl 6-(2-(5-azidopentan-2-ylidene)hydrazinyl)nicotinate.

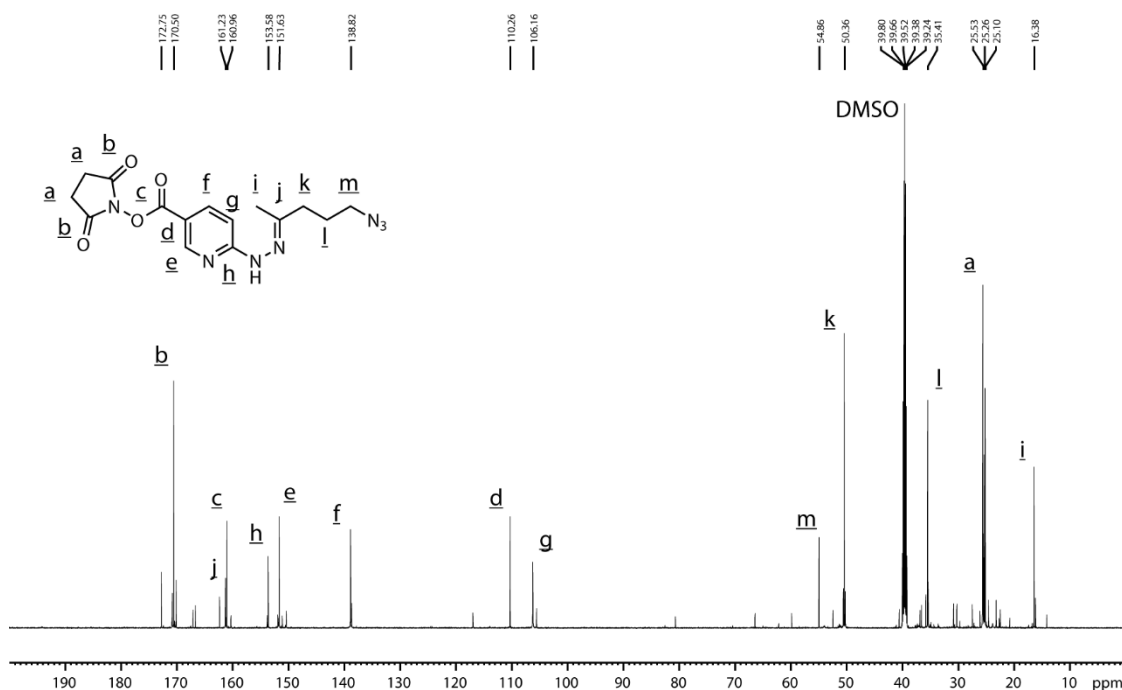


Figure A11. ^{13}C NMR spectrum of 2,5-dioxopyrrolidin-1-yl 6-(2-(5-azidopentan-2-ylidene)hydrazinyl)nicotinate.

PROTOCOL FOR EXPRESSION OF Q β

Plasmids containing the vectors for the expression of Q β were donated by Dr. M.G. Finn of the Georgia Institute of Technology. A starter culture (5 mL) of *E. coli* BL21 cells containing the plasmid for Q β expression was amplified to 1 L of SOB media (100 $\mu\text{g/mL}$ kanamycin) at 310 K until the OD_{600} reached 0.9-1.0. Isopropyl β -D-1-thiogalactopyranoside (IPTG) (1 mM final concentration) was then added to the media to induce the expression of Q β . Q β expression was carried out at 37 $^{\circ}\text{C}$ overnight. The cells were centrifuged using a Thermo Sorvall Lynx 4000 centrifuge and ThermoFisher Fiberlite F10-4 \times 1000 LEX rotor (19,510 $\times g$, 4 $^{\circ}\text{C}$, 1 h). The resulting pellet was resuspended in KP buffer (0.1 M, 50 mL, pH 7.4) and the cells were lysed using a cell homogenizer. The lysate was centrifuged using a Thermo Sorvall Lynx 4000 centrifuge and

ThermoFisher Fiberlite F10-4×1000 LEX rotor (19,510 ×g, 4 °C, 1 h). The resulting supernatant was collected and ammonium sulfate (2 M final concentration) was added. The resulting suspension was shaken (4 °C, >1 h) and centrifuged using a Thermo Sorvall Lynx 4000 centrifuge and ThermoFisher Fiberlite F10-4×1000 LEX rotor (19,510 ×g, 4 °C, 1 h). The resulting pellet was resuspended in KP buffer (0.1 M, 10 mL, pH 7.4), and a solution of 1:1 chloroform:*n*-butanol (10 mL) was added. The resulting suspension was centrifuged using a Thermo Sorvall Lynx 4000 centrifuge and ThermoFisher Fiberlite F10-4×1000 LEX rotor (19,510 ×g, 4 °C, 30 min). The aqueous layer was collected and purified via a sucrose gradient (10-40%) using a ThermoFisher Sorvall wX+ Ultra Series centrifuge and a Beckman Coulter SW 28 Ti rotor (73,078 ×g, 4 °C, 16 h). The resulting band containing Q β particles was observed by shining white light from the bottom of the tube and collected. The suspension was centrifuged using a ThermoFisher Sorvall wX+ Ultra Series centrifuge and a Beckman Coulter Type 70 Ti rotor (504,000 ×g, 4 °C, 3 h). The resulting pellet was collected and resuspended in the desired buffer.

BIOCONJUGATION OF Q β

Synthesis of Q β -6X

2,5-Dioxopyrrolidin-1-yl 6-azidohexanoate (5.4 mg, 21.2 μ mol) was dissolved in DMSO (1 mL). Cold (4 °C) KP buffer (0.1 M, 3 mL, pH 7.4) was added to the resulting solution of 2,5-dioxopyrrolidin-1-yl 6-azidohexanoate and mixed well. 6-(Prop-2-yn-1-yloxy)hexanoic acid (7.2 mg, 42.5 μ mol) was added to the resulting solution and mixed well. An aqueous solution of copper sulfate pentahydrate (0.1 M, 10 μ L) was added to the resulting solution and mixed well. An aqueous solution of sodium ascorbate (0.2 M, 10 μ L) was added to the resulting solution and mixed

well. A cold (4 °C) solution of Q β (5 mg/mL, 1 mL, 2 nmol) KP buffer (0.1 M, pH 7.4) was added to the solution and mixed well. The reaction was left to proceed at RT for 24 h. The resulting product was purified via either size exclusion chromatography using a GE Healthcare PD-10 Desalting Column or centrifuge filtration using an EMD Millipore Amicon Ultra Centrifugal Filter Unit (4,303 $\times g$).

Synthesis of Q β -Trim

Tris(2,5-dioxopyrrolidin-1-yl) benzene-1,3,5-tricarboxylate (10.65 mg, 21.2 μ mol) was dissolved in DMSO (1 mL). Cold (4 °C) KP buffer (0.1 M, 3 mL, pH 7.4) was added to the resulting solution of tris(2,5-dioxopyrrolidin-1-yl) benzene-1,3,5-tricarboxylate and mixed well. A cold (4 °C) solution of Q β (5 mg/mL, 1 mL, 2 nmol) KP buffer (0.1 M, pH 7.4) was added to the solution and mixed well. The reaction was left to proceed at RT for 24 h. The resulting product was purified via either size exclusion chromatography using a GE Healthcare PD-10 Desalting Column or centrifuge filtration using an EMD Millipore Amicon Ultra Centrifugal Filter Unit (4,303 $\times g$).

Synthesis of Q β -ZX

2,5-Dioxopyrrolodin-1-yl 6-(2-(1-azidopropan-2-ylidene)hydrazinyl)nicotinate (4.7 mg, 14.2 μ mol) was dissolved in DMSO (1 mL). Cold (4 °C) KP buffer (0.1 M, 3 mL, pH 7.4) was added to the resulting solution of 2,5-dioxopyrrolodin-1-yl 6-(2-(1-azidopropan-2-ylidene)hydrazinyl)nicotinate and mixed well. 6-(Prop-2-yn-1-yloxy)hexanoic acid (4.8 mg, 28.4 μ mol) was added to the resulting solution and mixed well. An aqueous solution of copper sulfate pentahydrate (0.1 M, 10 μ L) was added to the resulting solution and mixed well. An aqueous

solution of sodium ascorbate (0.2 M, 10 μ L) was added to the resulting solution and mixed well. A cold (4 $^{\circ}$ C) solution of Q β (5 mg/mL, 1 mL, 2 nmol) KP buffer (0.1 M, pH 7.4) was added to the solution and mixed well. The reaction was left to proceed at RT for 24 h. The resulting product was purified via either size exclusion chromatography using a GE Healthcare PD-10 Desalting Column or centrifuge filtration using an EMD Millipore Amicon Ultra Centrifugal Filter Unit (4,303 $\times g$).

Synthesis of Q β -ZX2

2,5-Dioxopyrrolodin-1-yl 6-(2-(5-azidopentan-2-ylidene)hydrazinyl)nicotinate (5.1 mg, 14.2 μ mol) was dissolved in DMSO (1 mL). Cold (4 $^{\circ}$ C) KP buffer (0.1 M, 3 mL, pH 7.4) was added to the resulting solution of 2,5-dioxopyrrolodin-1-yl 6-(2-(5-azidopentan-2-ylidene)hydrazinyl)nicotinate and mixed well. 6-(Prop-2-yn-1-yloxy)hexanoic acid (4.8 mg, 28.4 μ mol) was added to the resulting solution and mixed well. An aqueous solution of copper sulfate pentahydrate (0.1 M, 10 μ L) was added to the resulting solution and mixed well. An aqueous solution of sodium ascorbate (0.2 M, 10 μ L) was added to the resulting solution and mixed well. A cold (4 $^{\circ}$ C) solution of Q β (5 mg/mL, 1 mL, 2 nmol) KP buffer (0.1 M, pH 7.4) was added to the solution and mixed well. The reaction was left to proceed at RT for 24 h. The resulting product was purified via either size exclusion chromatography using a GE Healthcare PD-10 Desalting Column or centrifuge filtration using an EMD Millipore Amicon Ultra Centrifugal Filter Unit (4,303 $\times g$).

MALDI-TOF MS

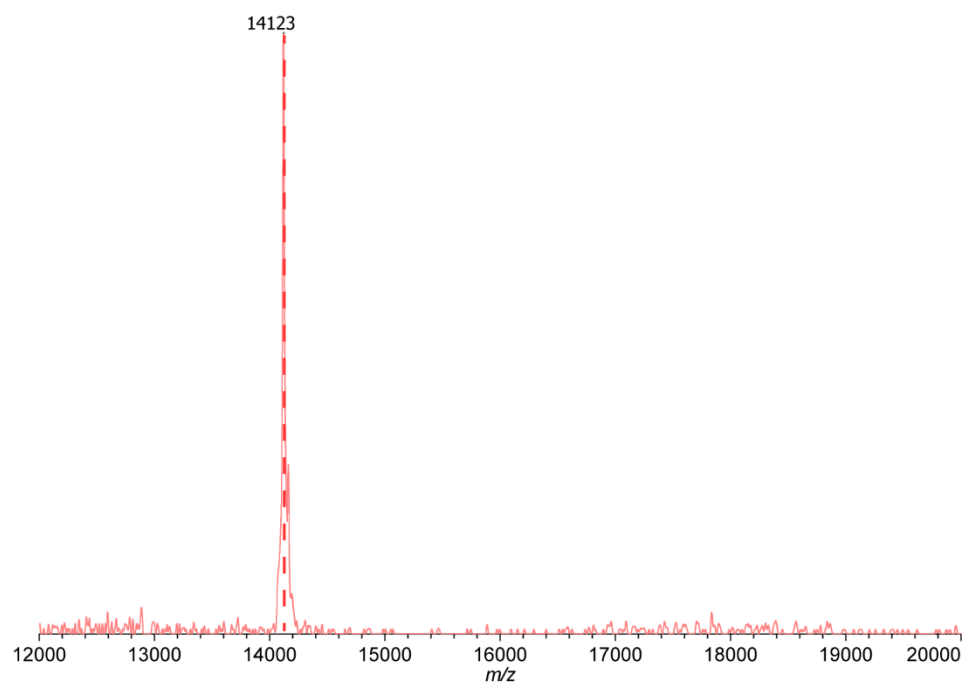


Figure A12. MALDI-TOF MS spectrum of native Q β coat protein. Theoretical mass indicated by the dotted red line.

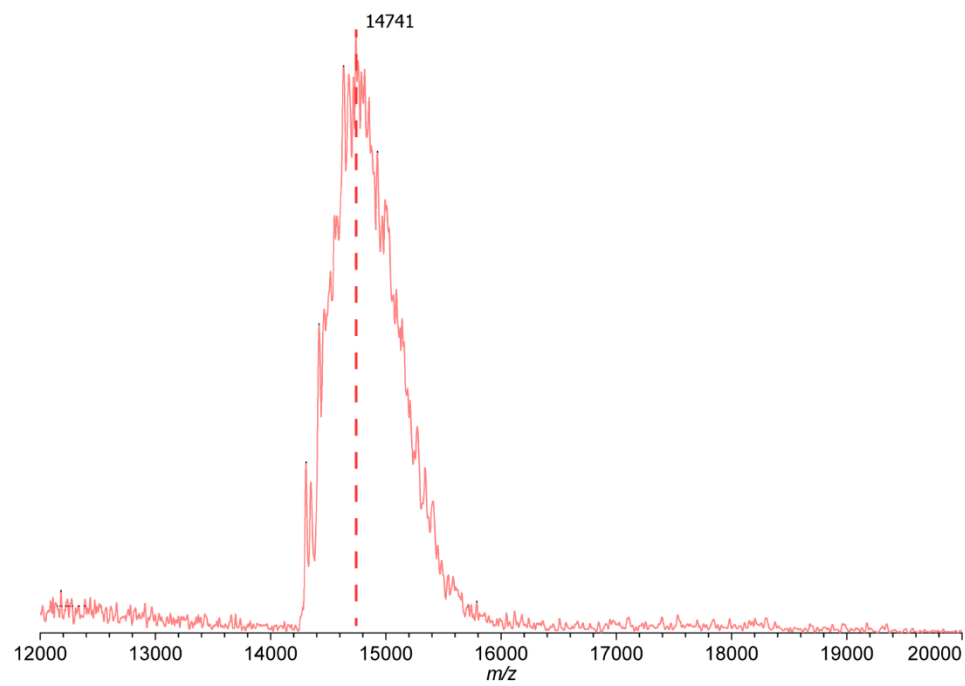


Figure A13. MALDI-TOF MS spectrum of Q β -6X coat protein. Theoretical mass indicated by the dotted red line.

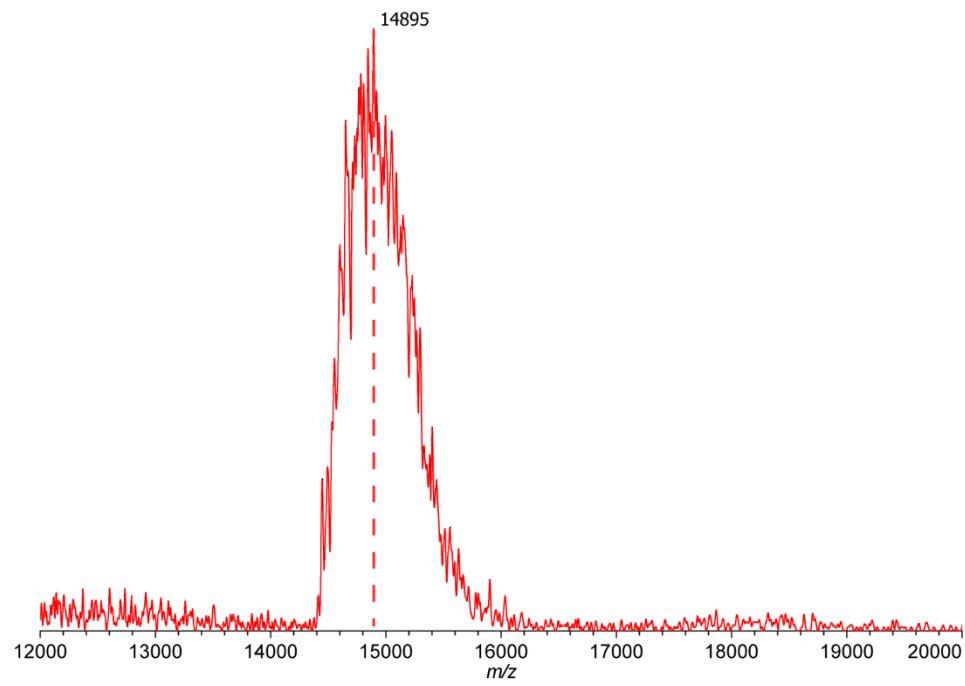


Figure A14. MALDI-TOF MS spectrum of Q β -ZX coat protein. Theoretical mass indicated by the dotted red line.

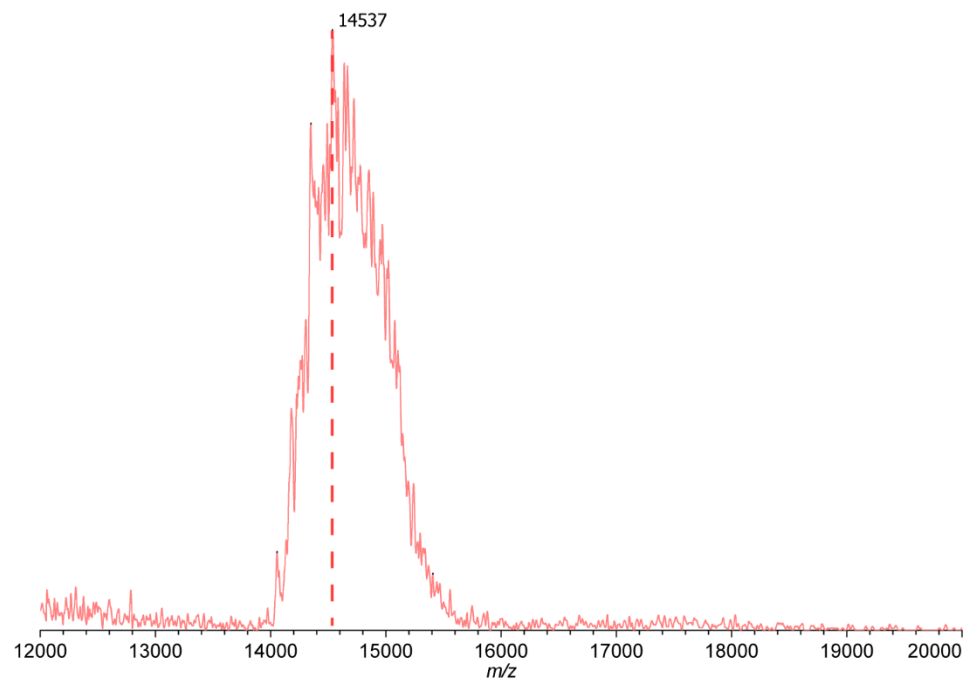


Figure A15. MALDI-TOF MS spectrum of Q β -ZX2 coat protein. Theoretical mass indicated by the dotted red line.

ESI-TOF MS

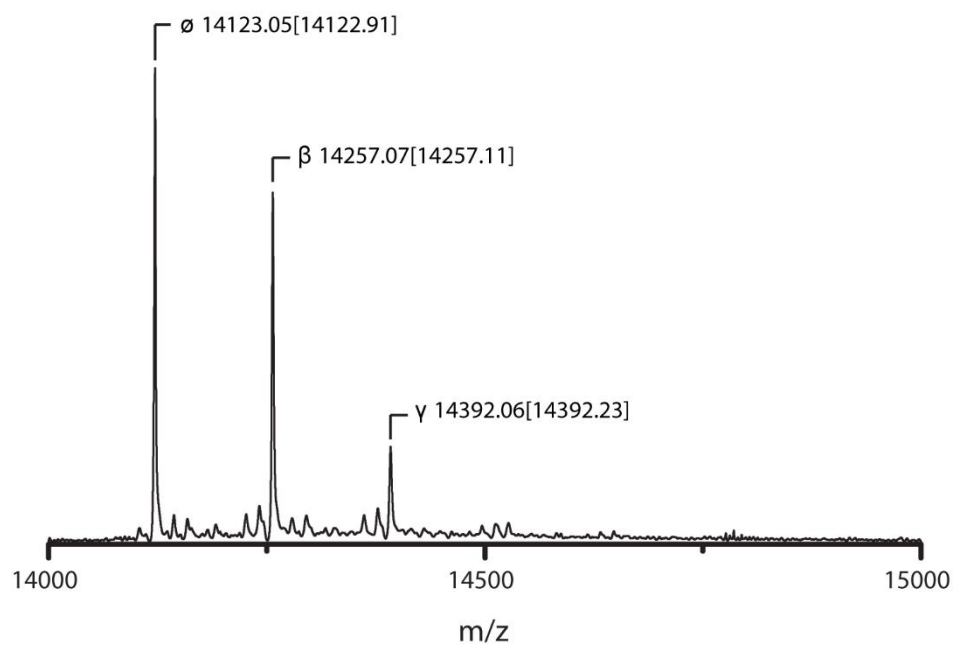


Figure A16. ESI-TOF MS spectrum of Q β -ZX-Hyd coat protein. Theoretical mass is quoted in brackets for unmodified coat protein (\emptyset), coat protein with one (β), and two (γ) functionalized residues.

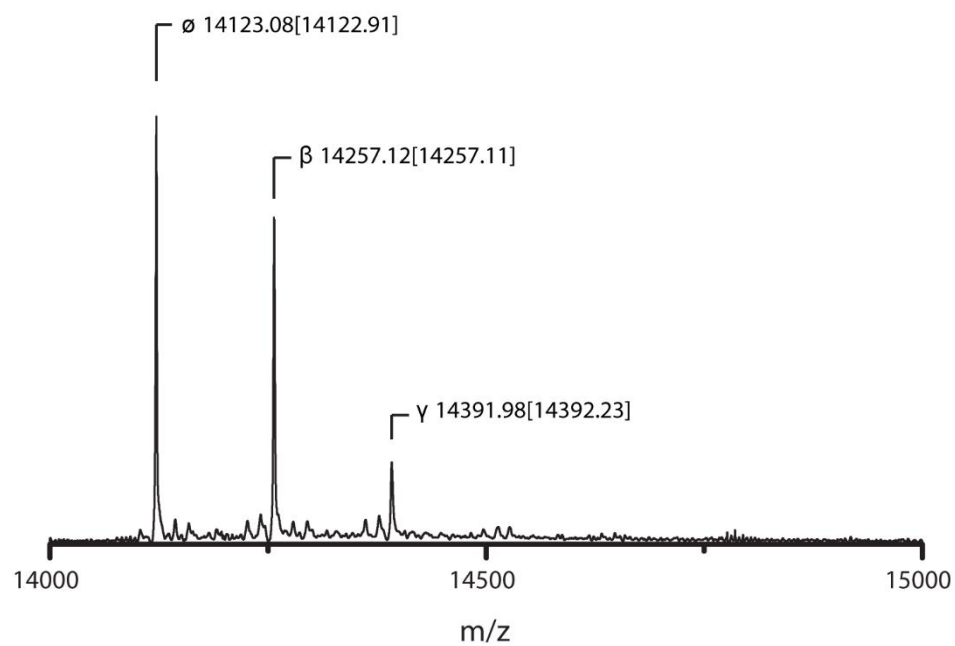


Figure A17. ESI-TOF MS spectrum of Qβ-ZX2-Hyd coat protein. Theoretical mass is quoted in brackets for unmodified coat protein (Ø), coat protein with one (β), and two (γ) functionalized residues.

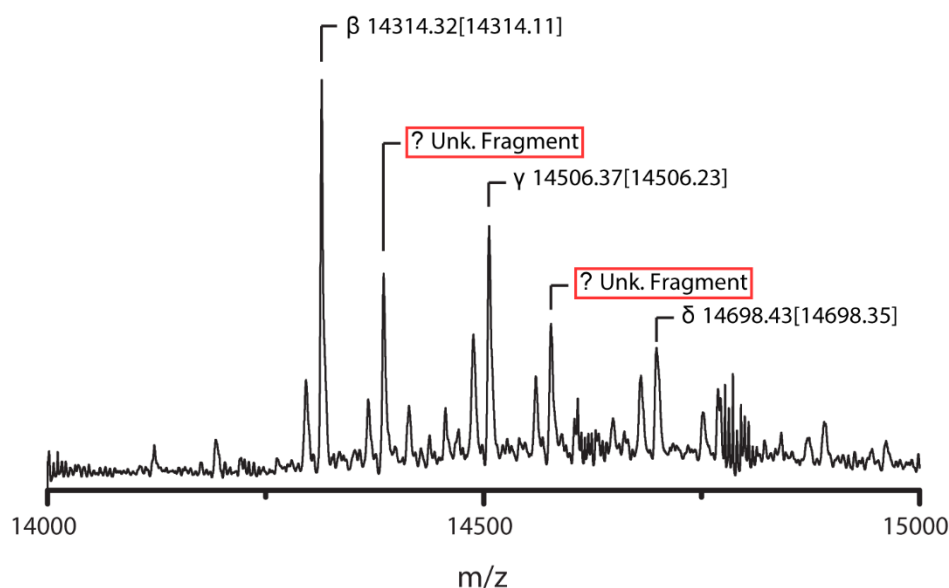


Figure A18. ESI-TOF MS spectrum of Qβ-Trim coat protein. Theoretical mass is quoted in brackets for coat protein with one (β), two (γ), and three (δ) functionalized residues. No peaks corresponding to Qβ-Trim coat proteins where the NHS moieties of trimesic acid are still attached were observed. Peaks with labels outlined in red do not correspond to any known conjugates or fragments, including conjugates in which the unused NHS moieties are still attached.

TRANSMISSION ELECTRON MICROSCOPY

Transmission electron micrographs were taken on a JEOL JEM-1400+ transmission electron microscope at 120 kV with a Gatan 4k × 4k CCD camera. 5 μL of the ~0.1 mg/mL desalted sample was placed on a 300 mesh Formvar/carbon-coated copper grid (Electron Microscopy Sciences, Hatfield, PA, USA), allowed to stand for 30 seconds, and wicked off with Whatman #1 filter paper. 5 μL of 2% uranyl acetate (SPI Supplies, West Chester, PA, USA) was placed on the grid, allowed to stand for 30 seconds, wicked off as before, and the grid allowed to dry completely in air.

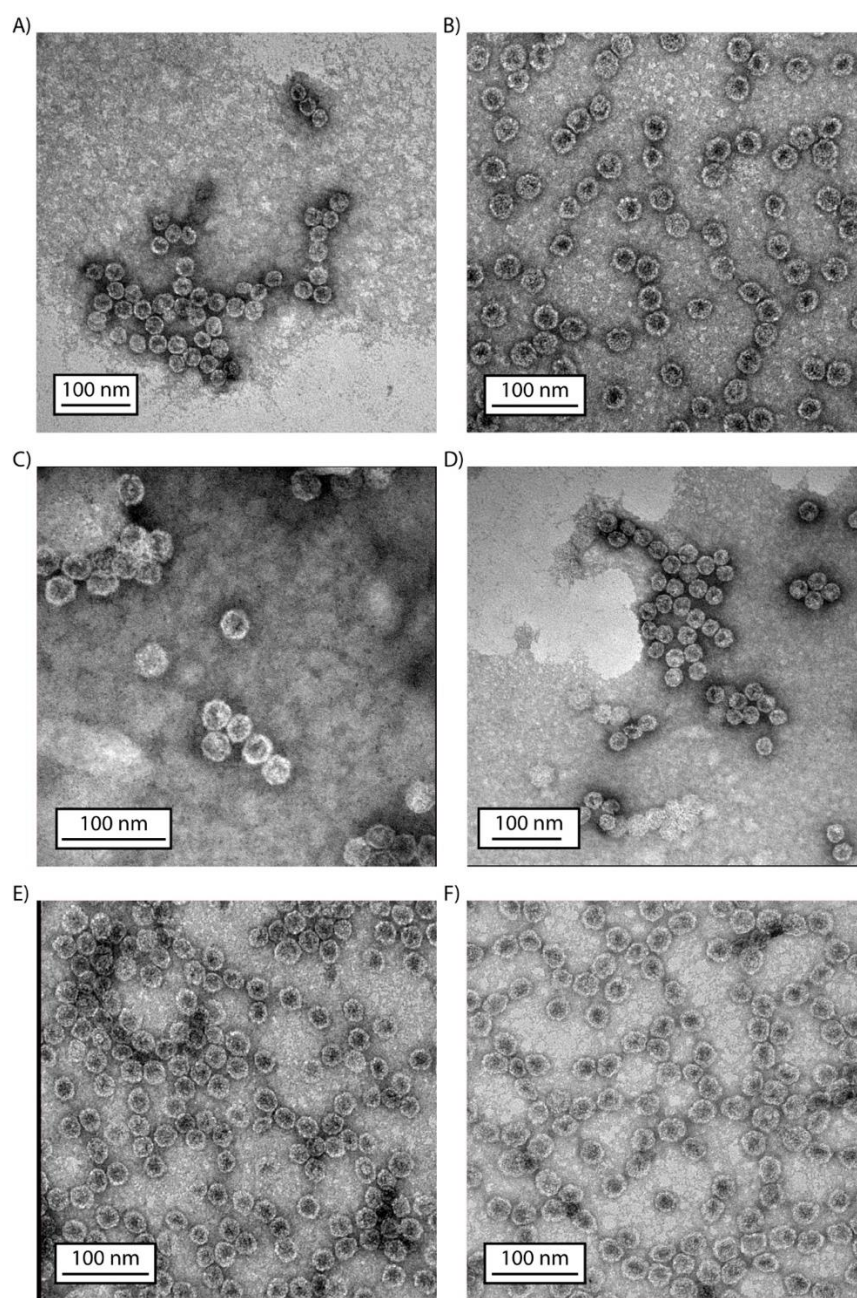


Figure A19. TEM images of A) Native Q β , B) Q β -6X, C) Q β -ZX, D) Q β -ZX-Hyd, E) Q β -ZX2, F) Q β -ZX2-Hyd.

DYNAMIC LIGHT SCATTERING

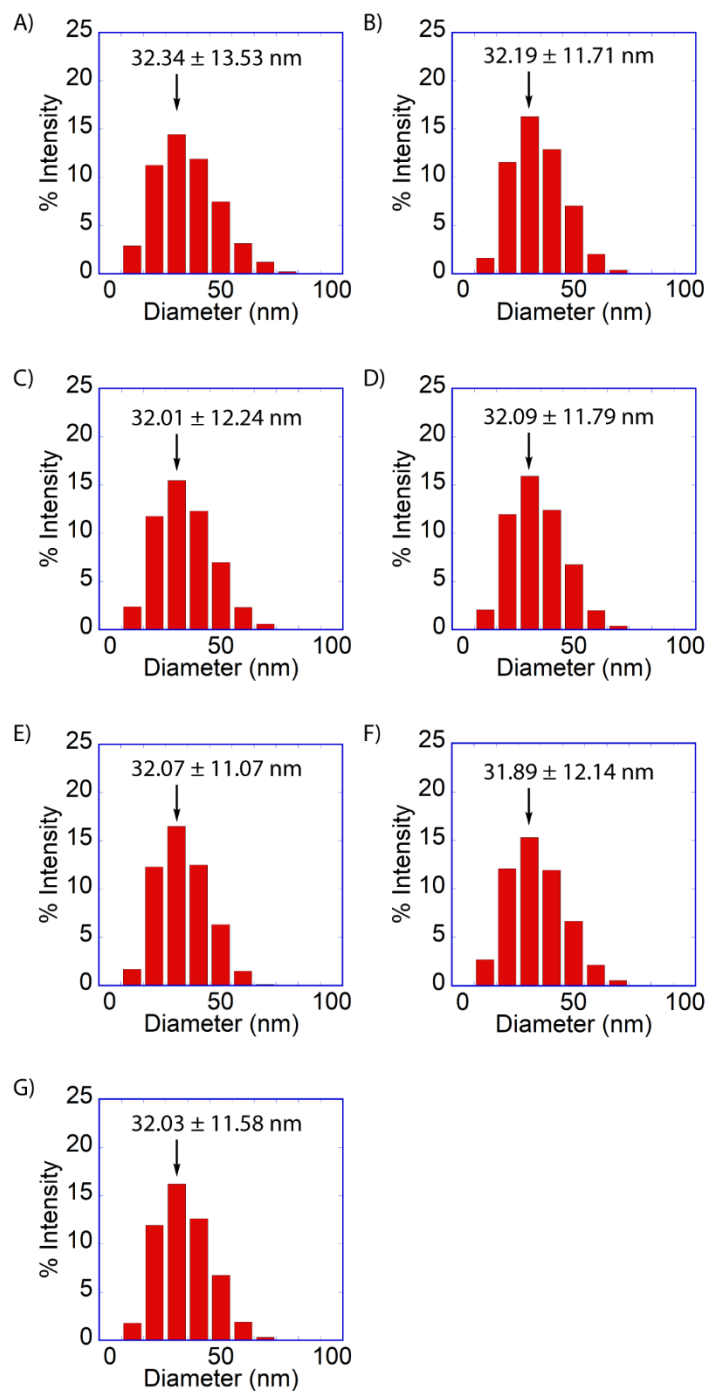


Figure A20. DLS data of A) Native Qβ, B) Qβ-6X, C) Qβ-ZX, D) Qβ-ZX-Hyd, E) Qβ-ZX2, F) Qβ-ZX2-Hyd, G) Qβ-Trim.

NATIVE AGAROSE GEL ELECTROPHORESIS

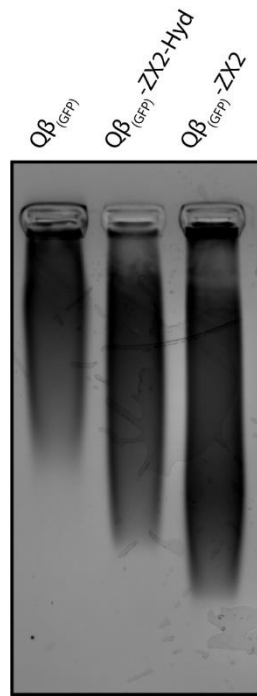


Figure A21. Native agarose gel electrophoresis of Q β , Q β -ZX2, and Q β -ZX2-Hyd.

CELL CULTURES

RAW 264.7 macrophage and HeLa cell lines were cultured in Dulbecco's Modified Eagle's Medium (DMEM) (Sigma-Aldrich, with 4500 mg/L glucose, L-glutamine, sodium pyruvate, and sodium bicarbonate) culture media supplemented with 10% FB Essence (VWR Life Sciences Seradigm) and 1% Pen-Strep (Sigma-Aldrich), and the cultured cells were maintained in a 37 °C incubator with 5% CO₂. Approximately 1.0×10^5 cells were seeded on glass coverslips in a 24-well cell culture plate and were incubated for at least 24 hours prior to incubation with Q β conjugates.

EPIFLUORESCENCE MICROSCOPY

RAW 264.7 macrophages and HeLa cells were treated with various concentrations (10, 30 or 50 μ M) of native Q β , Q $\beta_{(GFP)}$, and Q β conjugates and incubated at 37 °C for 4 hours. Cells were then washed 3 \times with PBS (1 \times , pH 7.4) (Sigma-Aldrich) and fixed with 4% paraformaldehyde in PBS. The cells were again washed 3 \times with PBS and stained with 300 nM DAPI and 100 nM Wheat Germ Agglutinin, Alexa Fluor® 555 Conjugate (Thermo-Fisher Scientific), washing 3 \times with PBS in between. The coverslips were mounted on glass slides and imaged on a Life Technologies EVOS FL Auto Epifluorescence microscope with a 60 \times objective. (LED Cubes: DAPI, RFP and GFP).

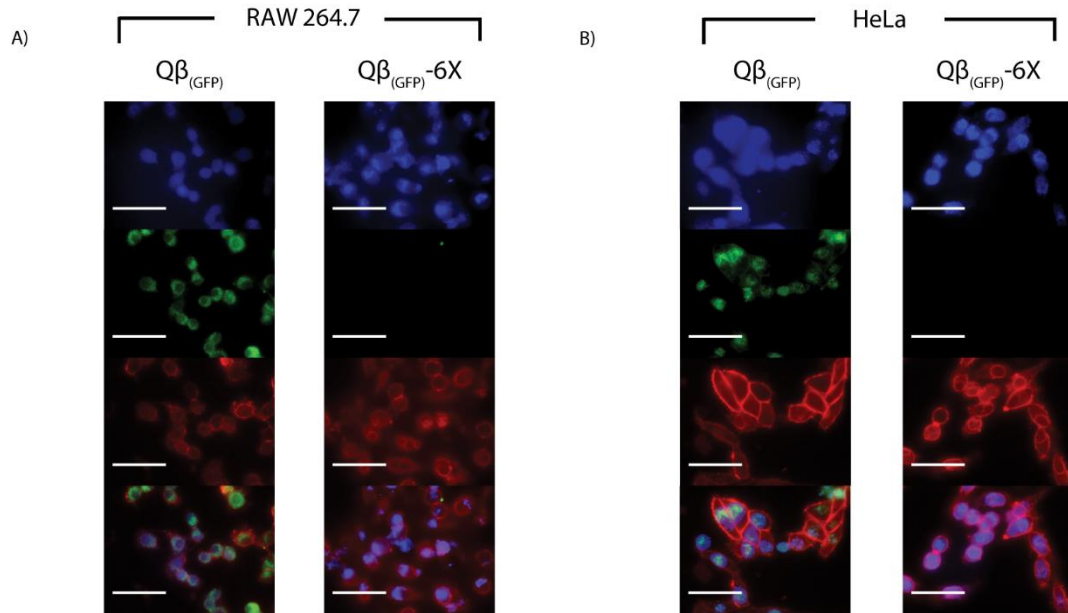


Figure A22. Epifluorescence microscope images of A) RAW 264.7 macrophages and B) HeLa cells incubated with their respective Q β samples (50 μ M). Blue: DAPI, Red: WGA-AlexaFluor 555, and Green: GFP. Scale bar represents 50 μ m.

FLOW CYTOMETRY

For each cell line, approximately 1.0×10^5 cells were harvested and resuspended in 500 μ L PBS (1 \times , pH 7.4) per sample. 10,000-50,000 (SSC-W vs. SSC-A)-gated events per sample were collected using a BD LSRFortessa™ flow cytometer. GFP fluorescence was detected using a 488 nm laser for excitation and emission was measured with 515/20 nm band-pass filter. Raw data were processed and analyzed using FlowJo® software. Histogram overlays were normalized to mode to compare samples that vary in number of recorded events. A fluorescence intensity value of 1.0×10^3 was set as a threshold for a significant increase in signal.

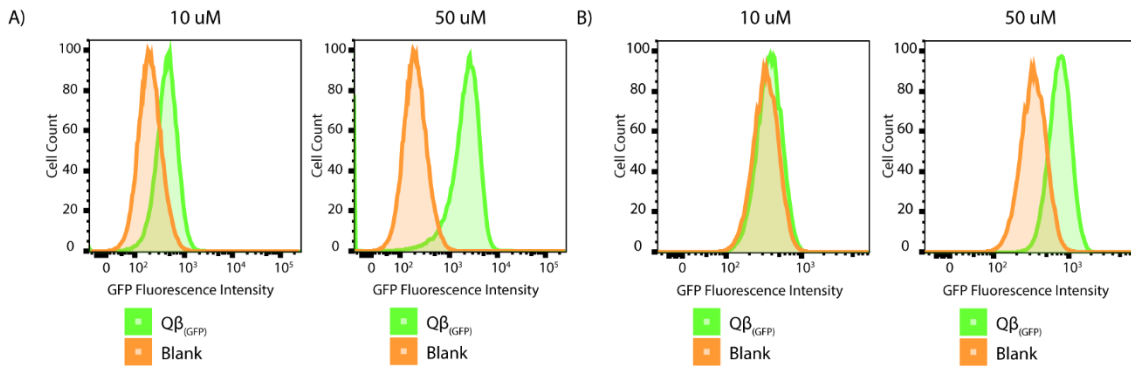


Figure A23. Representative histograms from flow cytometry studies corresponding to A) RAW 264.7 macrophages and B) HeLa cells incubated with PBS buffer and Q $\beta_{(GFP)}$. All cells were incubated with their respective samples for 4 h at 37 °C.

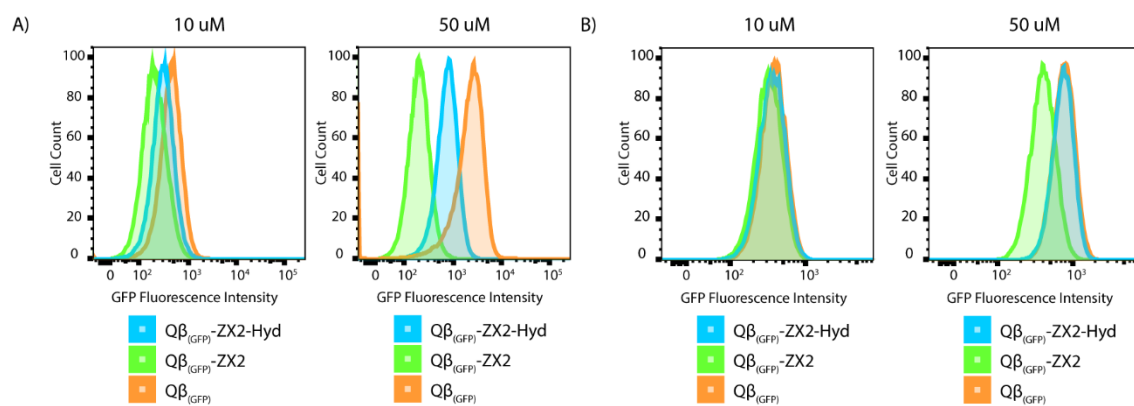


Figure A24. Representative histograms from flow cytometry studies corresponding to A) RAW 264.7 macrophages and B) HeLa cells incubated with their respective Q β samples. All cells were incubated with the Q β conjugates for 4 h at 37 °C.

APPENDIX B

SUPPORTING INFORMATION FOR CHAPTER 3

MATERIALS

All chemicals were purchased from Sigma-Aldrich (St. Louis, MO), ThermoFisher Scientific (Pittsburgh, PA), Alfa Aesar (Ward Hill, MA), TCI America (Portland, OR), VWR International (Radnor, PA), and used without further purification.

INSTRUMENTATION

^1H and ^{13}C NMR spectra were obtained using a 600 MHz Bruker Avance NMR spectrometer with residual solvent peaks as a reference for all NMR spectra. ESI-MS were acquired using a Waters M-class UPLC with a RP C4 BEH column for separation and a Waters Synapt G2-Si for detection. Size exclusion chromatography (SEC) was conducted using an Agilent 1100 HPLC with a Phenomenex PolySep-GFC-P Linear 300×7.8 mm column. Isothermal titration calorimetry (ITC) was conducted using a Malvern Microcal iTC200. Transmission electron microscopy (TEM) was conducted using a JEOL JEM-1400Plus transmission electron microscope. Fluorescence data were obtained using a BioTek Synergy H4 Hybrid microplate reader. EPR spectroscopy was performed using a Bruker EMX ER041XG X-band spectrometer with a Bruker ER 4119HS resonator. NMR relaxometry experiments were performed with a 43 MHz Magritek Spinsolve NMR operating with a magnetic field strength of 1 T.

SYNTHESIS

Synthesis of Imidazole-1-sulfonyl azide hydrogen sulfate

NaN_3 (10 g, 154 mmol) was stirred in dry EtOAc (150 mL) at 0 °C, 0.5 h. Sulfuryl chloride (20.7g, 12.4 mL, 153 mmol) was added dropwise while stirring was maintained. The resulting mixture was stirred at RT, 24 h. The reaction mixture was cooled to 0 °C in an ice bath. Imidazole (20 g, 294 mmol) was slowly added over 5 min. The resulting mixture was stirred at 0 °C, 5 h. A saturated NaHCO_3 solution (aq.) (300 mL) was added to the reaction mixture. The organic fraction was isolated, washed with H_2O (3×100 mL) and dried with MgSO_4 . The organic fraction was filtered and the filtrate was collected. The resulting solution was cooled to 0 °C in an ice bath while stirring was maintained. H_2SO_4 (18 M, 8.4 mL, 151 mmol) was added dropwise over 5 min while vigorous stirring was maintained. The resulting solution was stirred vigorously at RT until colorless or white precipitate was formed. The reaction mixture was filtered and the feed was washed with EtOAc (0 °C). The feed was collected and solvent was removed under reduced pressure to yield the product as a white solid.

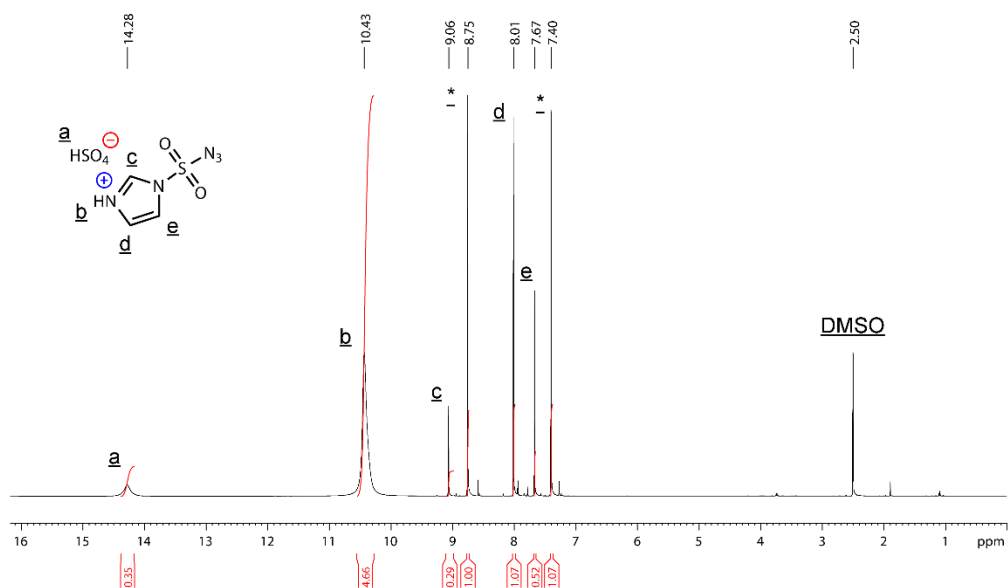


Figure B1. ¹H NMR spectrum of imidazole-1-sulfonyl azide hydrogen sulfate.

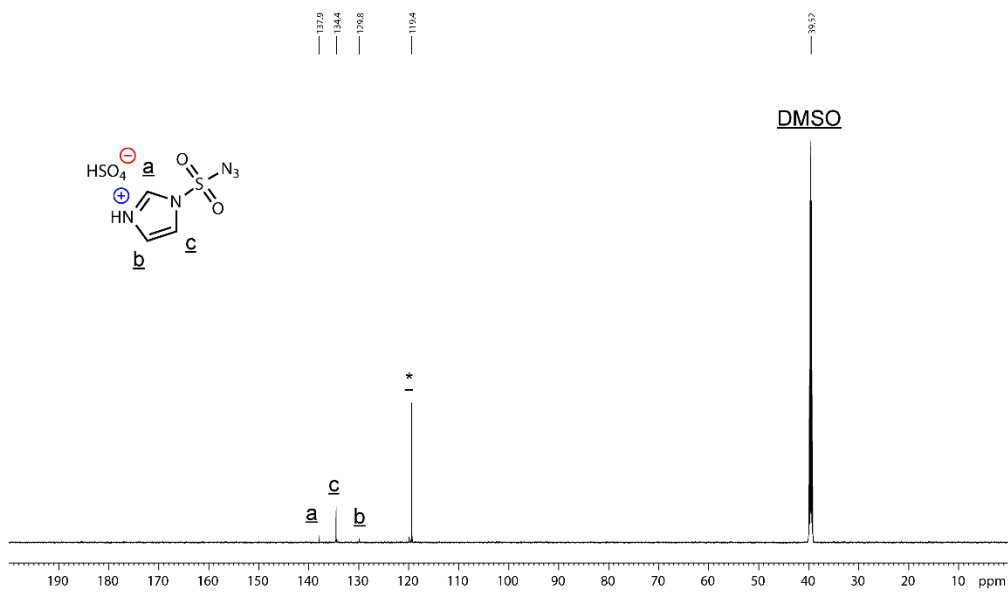


Figure B2. ¹³C NMR spectrum of imidazole-1-sulfonyl azide hydrogen sulfate.

Synthesis of 6-Azidohexanoic acid (**2**)

Compound **1** (5.0 g, 25.6 mmol), and NaN₃ (4.998 g, 76.9 mmol) were stirred in DMF (20 mL) at 85 °C overnight. Upon cooling the reaction to RT, DCM (40 mL) was added to the reaction mixture and stirred. The reaction mixture was then washed with aqueous HCl (0.1 M, 3×20 mL) and dried with MgSO₄. The organic fraction was isolated and the solvent was removed under reduced pressure to yield the product as a clear pale yellow oil. ¹H NMR (600 MHz, CDCl₃) δ ppm 1.43 (quint, J = 7.2 Hz, 2 H) 1.61 (quint, J = 7.2 Hz, 2 H) 1.67 (t, J = 7.2 Hz, 2H) 2.37 (quint, J = 7.2 Hz, 2H) 3.27 (t, J = 6.4 Hz, 2 H).

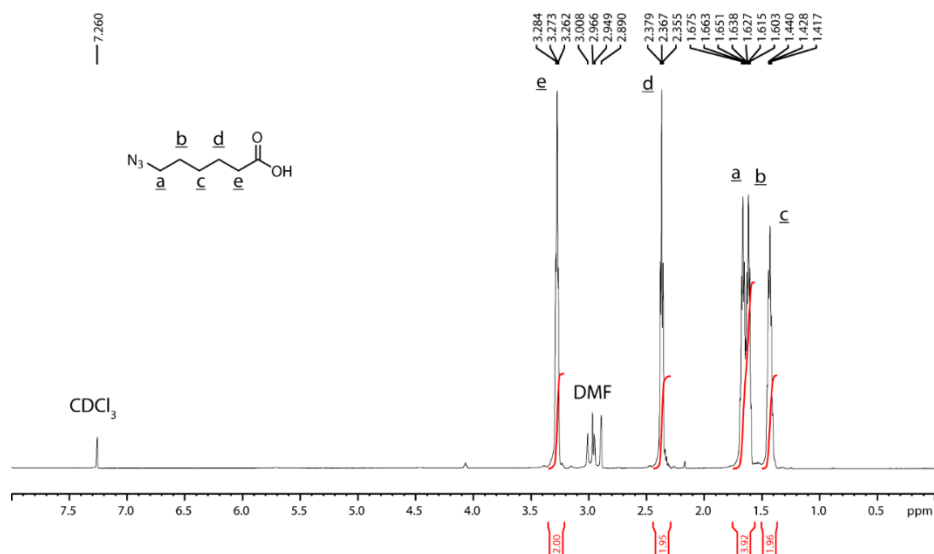


Figure B3. ¹H NMR spectrum of **2**.

Synthesis of 2,5-Dioxopyrrolidin-1-yl 6-azidohexanoate (**3**)

Compound **2** (2.0 g, 12.7 mmol), *N*-hydroxysuccinimide (NHS) (4.395 g, 38.2 mmol), and 1-ethyl-3-(3-dimethylaminopropyl)carbodiimide (EDC) (5.929 g, 38.2 mmol) were dissolved in DMF (15

mL) and stirred at RT, 48 h. DMF was then removed under reduced pressure. The remaining residue was dissolved in ethyl acetate (EtOAc) (25 mL). The organic layer was washed with H₂O (3×40 mL), saturated brine (3×40 mL), and dried with MgSO₄. The solvent was removed under reduced pressure to yield the crude product. The crude product was further purified via column chromatography (silica gel) with Hexanes:EtOAc (100:0-0:100). The fractions corresponding to the product were combined and the solvent was removed under reduced pressure to yield the product as a clear pale yellow oil. ¹H NMR (600 MHz, CDCl₃) δ ppm 1.49 (quint, J = 6.8 Hz, 2 H) 1.63 (quint, J = 7.1 Hz, 2 H) 1.77 (t, J = 7.0 Hz, 2 H) 2.61 (quint, J = 7.1 Hz, 2 H) 2.82 (s, 4 H) 3.28 (t, J = 6.4 Hz, 2 H).

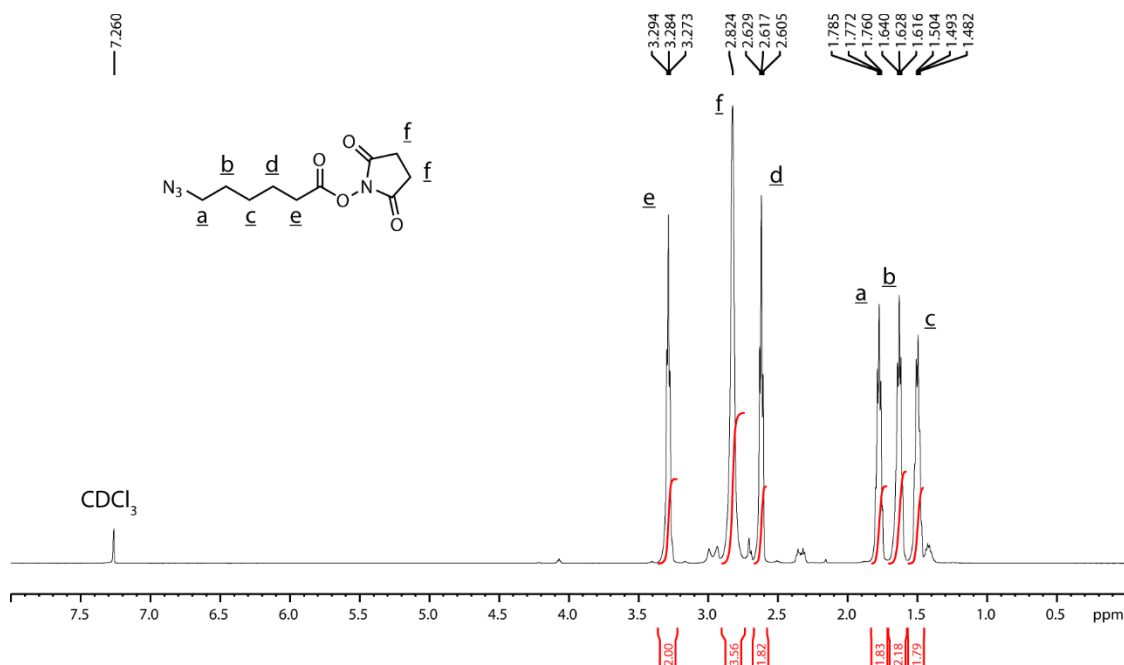


Figure B4. ¹H NMR spectrum of **3**.

Synthesis of 6-Azido-N-(1-oxyl-2,2,6,6-tetramethylpiperidin-4-yl)hexanamide (4)

4-Amino-2,2,6,6-tetramethylpiperidine-1-oxyl (2.0 g, 11.7 mmol), **3** (5.94 g, 23.3 mmol), and TEA (1.18 g, 11.7 mmol) were dissolved in dry (need not be anhydrous) DMF (25 mL). Potassium carbonate (1.61 g, 11.7 mmol) was added and the mixture was stirred at RT, OVN. DCM (50 mL) and H₂O (20 mL) were added and the reaction mixture was washed with H₂O (3×50 mL). The aqueous fraction was extracted with DCM (2×25 mL) and the organic fractions were combined. The organic fraction was washed with H₂O (3×50 mL) and dried with MgSO₄. The solvent was removed under reduced pressure. The crude product was further purified via column chromatography (silica) with DCM:MeOH (100:0 - 90:10). The solvent was removed under reduced pressure to yield the product as a red liquid.

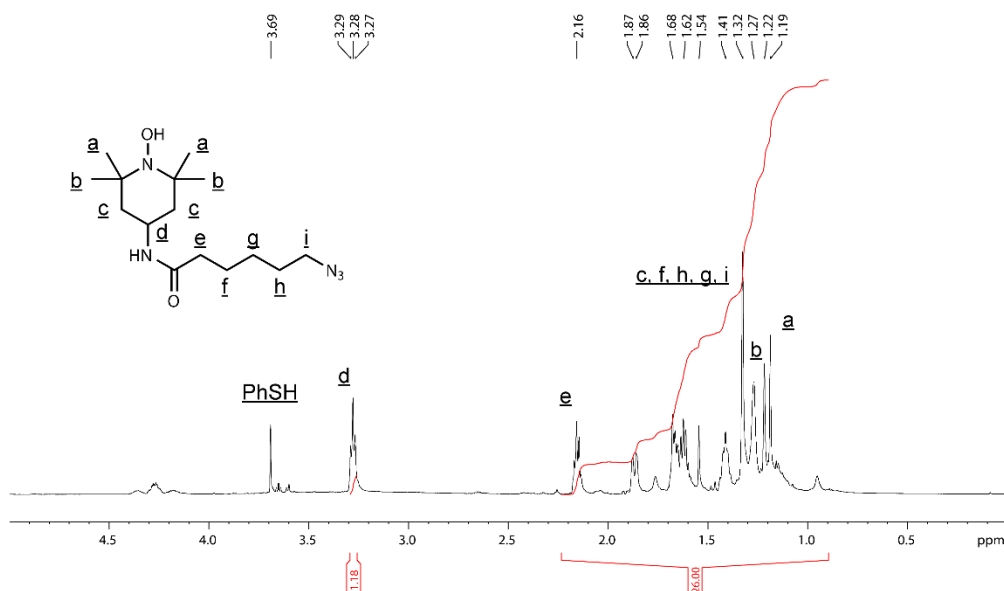


Figure B5. ¹H NMR spectrum of **4**.

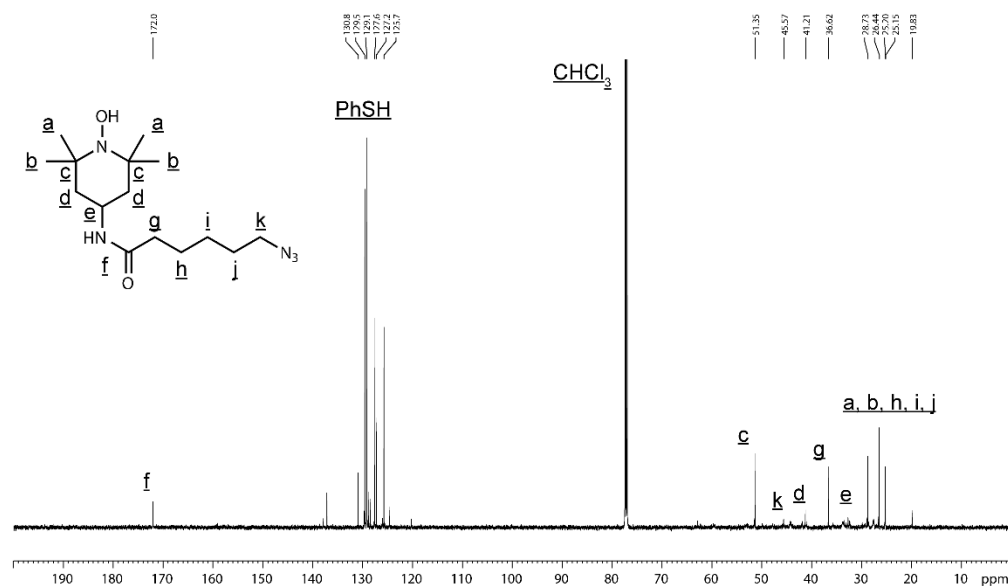


Figure B6. ^{13}C NMR spectrum of **4**.

*Synthesis of 4-((6-Aminohexyl)amino)-2,2,6,6-tetramethylpiperidin-1-oxyl (**5**)*

6-Azido-N-(1-oxyl-2,2,6,6-tetramethylpiperidin-4-yl)hexanamide (2.0 g, 6.4 mmol) was dissolved in Et_2O (100 mL) and LiAlH_4 (2.45 g, 64 mmol) was slowly added portionwise to the reaction solution. The reaction mixture was stirred at RT, OVN. The reaction mixture was cooled to 4 °C in an ice bath. H_2O (1.22 mL), followed by an aqueous NaOH solution (15% w/v, 1.22 mL), followed by H_2O (3.66 mL) were slowly added to the reaction mixture under stirring. Stirring was continued for 15 min. The reaction mixture was dried with MgSO_4 and stirred for 15 min. The resulting mixture was filtered and the feed was washed with Et_2O (100 mL). The organic fractions were combined. The solvent was removed under reduced pressure. The crude product was further purified via column chromatography (alumina) with $\text{DCM}:\text{MeOH}$ (100:0 - 90:10). The solvent was removed under reduced pressure to yield the product as a light orange liquid.

Synthesis of 4-((6-Azidohexyl)amino)-2,2,6,6-tetramethylpiperidin-1-oxyl (6)

4-((6-Aminohexyl)amino)-2,2,6,6-tetramethylpiperidin-1-oxyl (2.0 g, 7.4 mmol) was dissolved in MeOH (50 mL) and the reaction solution was cooled to 4 °C in an ice bath. 1*H*-Imidazole-1-sulfonyl azide hydrogen sulfate (2.21 g, 8.1 mmol), CuSO₄ · 5H₂O (0.02 g, 0.074 mmol), and K₂CO₃ (2.04 g, 14.8 mmol) were added and the reaction mixture was stirred at RT, OVN. The solvent was removed under reduced pressure. H₂O (25 mL) was added to the remaining residue and the resulting mixture was filtered. The feed was washed with H₂O (25 mL) and EtOAc (25 mL). The filtrate was collected and H₂O (25 mL) was added. The organic fraction was collected. The aqueous fraction was extracted w/ EtOAc (2×25 mL) and the organic fractions were combined. The combined organic fraction was washed with NaHCO₃ (aq.) (4% w/v, 2×30 mL), and saturated brine (2×30 mL). The organic fraction was collected and dried with MgSO₄. The solvent was removed under reduced pressure to yield the crude product. The crude product was further purified via column chromatography (alumina) with DCM:MeOH (100:0 - 90:10). The solvent was removed under reduced pressure to yield the product as a red liquid.

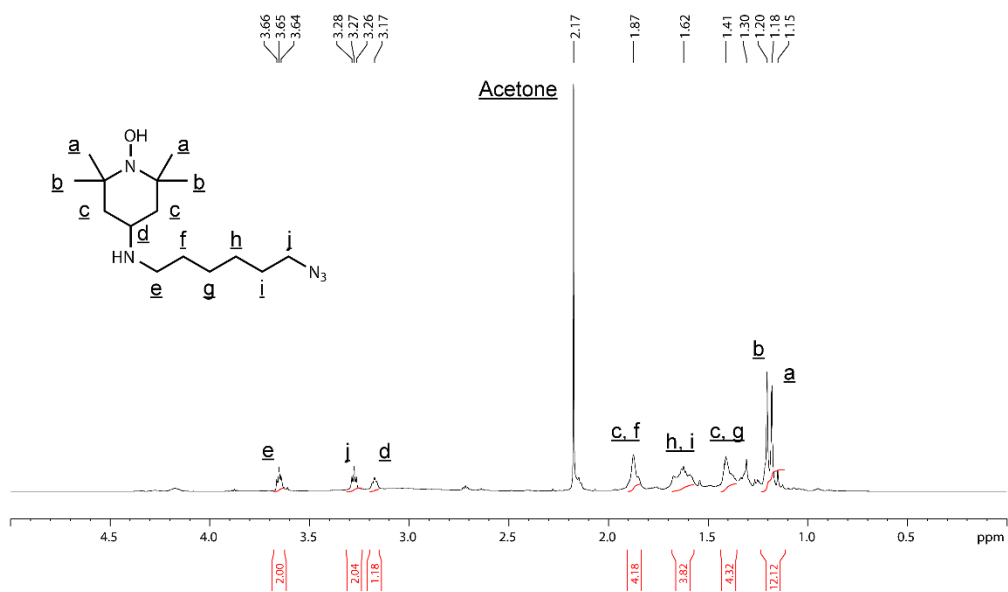


Figure B7. ¹H NMR spectrum of **6**.

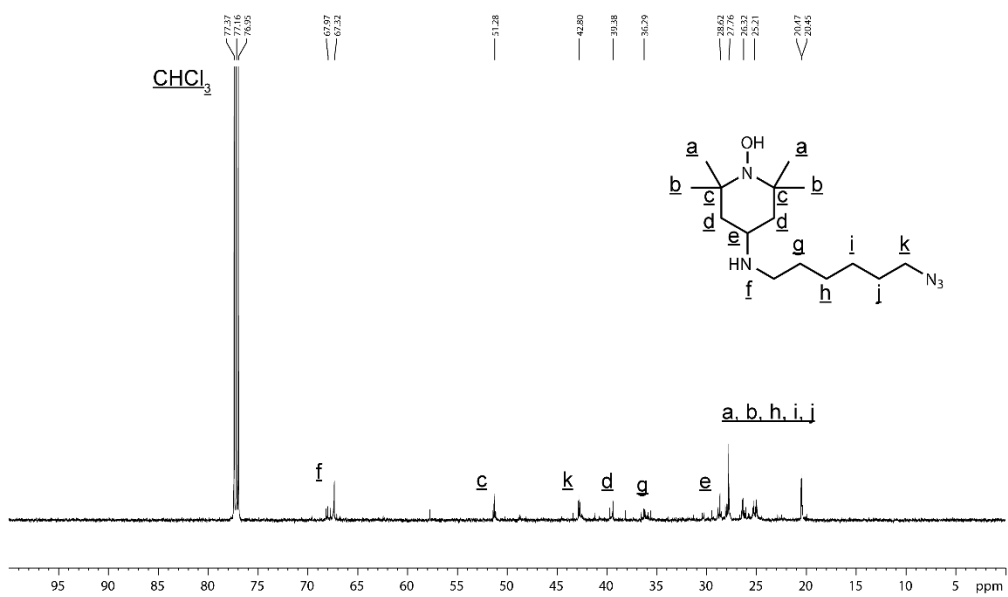


Figure B8. ¹³C NMR spectrum of **6**.

PROTOCOL FOR EXPRESSION OF TMV

TMV particles were isolated from *Nicotiana benthamiana* plants. Tobacco plants were grown, infected with a solution of TMV from a stock source, collected (~10 d after infection), and stored at -80 °C until needed. The leaves (~100 g) were blended with cold (4 °C) extraction buffer (KP buffer (0.1 M, 1000 mL, pH 7.4) with 2-mercaptoethanol (0.2% (v/v))), followed by thorough grinding with a mortar and pestle. The mixture was filtered through cheesecloth to remove the plant solids, and the filtrate centrifuged at 11,000 $\times g$ (4 °C, 20 min). The supernatant was filtered through cheesecloth again, and an equal volume of 1:1 chloroform/1-butanol mixture was added and stirred (4 °C, 30 min). The mixture was centrifuged at 4500 $\times g$ for 10 min. The aqueous phase was collected, followed by the addition of NaCl (final concentration of 0.2 M), PEG 8000 (8% (w/w)), and Triton X-100 surfactant (1% (w/w)). The mixture was stirred on ice for 30 min and stored (4 °C, 1 h). The solution was centrifuged at 22,000 $\times g$ (4 °C, 15 min). The supernatant was discarded, and the pellet resuspended in KP buffer (0.1 M, pH 7.4) (4 °C, OVN). The supernatant was carefully layered on a 40% (w/v) sucrose gradient in KP buffer (0.01 M, pH 7.4) (with at least one freeze-thaw cycle) in ultracentrifuge tubes and centrifuged in a swing bucket rotor for 2 h at 96,000 $\times g$. The light-scattering region was collected and centrifuged at 360,562 $\times g$ for 1.5 h. The supernatant was discarded, and the pellet resuspended in KP buffer (0.01 M, pH 7.4) (4 °C, OVN). The solution was portioned equally into microcentrifuge tubes and centrifuged at 15,513 $\times g$ for 15 min. The supernatant was collected as the final TMV solution. UV-Vis measurements were taken at 260 nm (RNA) and 280 nm (protein). A ratio of A₂₆₀/A₂₈₀ around 1.23 indicates intact TMV. Using the Beer-Lambert Law with $\epsilon = 3$ the concentration of the solution was determined.

BIOCONJUGATION OF TMV

Synthesis of TMV-Aky

Solutions of 3-ethynylaniline in acetonitrile (0.68 M, 75 μ L) and NaNO₂ (aq.) (3.0 M, 25 μ L) were added to a cold (4 °C) solution of p-toluenesulfonic acid (0.3 M, 400 μ L) and mixed well. The resulting solution was mixed in light-free conditions (4 °C, 1 h) to form the diazonium salt. A solution of TMV (20 mg/mL, 100 μ L, 0.1 μ mol) was diluted in borate buffer (0.1 M, pH 8.8, 862 μ L) and the resulting solution was chilled to 4 °C. The diazonium salt solution (70 eq per coat protein of TMV, 76 μ L) was added to the solution of TMV and the resulting solution was mixed in light-free conditions (4 °C, 45 min). The resulting product was purified via either size exclusion chromatography using a GE Healthcare PD-10 Desalting Column or centrifuge filtration using an EMD Millipore Amicon Ultra Centrifugal Filter Unit (4,303 $\times g$).

Synthesis of TMV-6

Compound **6** (1.7 mg, 5.7 μ mol) was dissolved in DMSO (1 mL). Cold (4 °C) KP buffer (0.1 M, 3 mL, pH 7.4) was added to the resulting solution and mixed well. A cold (4 °C) solution of TMV-Aky (20 mg/mL, 100 μ L, 0.1 μ mol) in KP buffer (0.1 M, pH 7.4) was added to the resulting solution and mixed well. An aqueous solution of copper sulfate pentahydrate (0.1 M, 10 μ L) was added to the resulting solution and mixed well. An aqueous solution of sodium ascorbate (0.2 M, 10 μ L) was added to the resulting solution and mixed well. The reaction was left to proceed at RT for 24 h. The resulting product was purified via either size exclusion chromatography using a GE Healthcare PD-10 Desalting Column or centrifuge filtration using an EMD Millipore Amicon Ultra Centrifugal Filter Unit (4,303 $\times g$).

FLUORESCENCE TITRATIONS

Fluorescence titrations of TMV-**6** into CB[8]⊃PF were performed using Greiner 384-well, black, flat-bottomed plates. Solutions of TMV-**6** were prepared by serial dilutions of a stock solution of TMV-**6** (200 μ M in terms of TEMPO) in sodium phosphate buffer (0.01 M, pH 7.0). TMV-**6**+CB[8]⊃PF solutions were prepared by mixing the appropriate TMV-**6** (20 μ L) solution with the solution of CB[8]⊃PF (0.6 μ M, 10 μ L). This resulted in solutions with final TMV-**6** concentrations from 0-20 μ M and a final CB[8]⊃PF concentration of 0.2 μ M. The solutions were mixed by pipetting before reading the fluorescence intensities on the plate reader (top reading mode; 400 nm excitation, 10 nm bandwidth; 510 nm emission, 20 nm bandwidth). Z-depth and gain were optimized on the first scan and then exact values were used in subsequent scans. For the titrations of native TMV (nTMV) into CB[8]⊃PF, all methods and parameters were identical to the titrations of TMV-**6** into CB[8]⊃PF, except for the use of nTMV instead of TMV-**6**. For the titrations of TMV-**6** into PF, all methods and parameters were identical to the titrations of TMV-**6** into CB[8]⊃PF, except for the use of PF instead of CB[8]⊃PF.

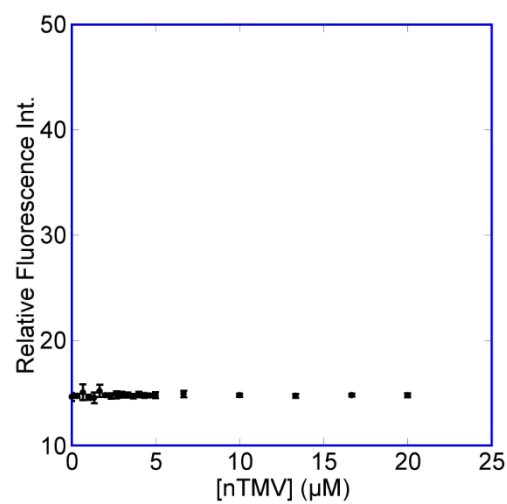


Figure B9. Fluorescence titration data for nTMV and CB[8]⊃PF. nTMV (0-20 μM in terms of TMV coat protein) was titrated into solutions of CB[8]⊃PF (0.2 μM).

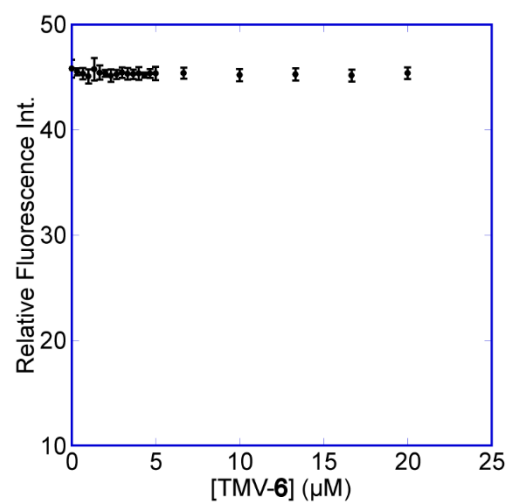


Figure B10. Fluorescence titration data for TMV-6 and PF. TMV-6 (0-20 μM in terms of TEMPO) was titrated into solutions of PF (0.2 μM).

EPR SPECTROSCOPY

All EPR measurements were obtained using the following instrumental conditions:

- Microwave Power: 4.54 mW
- Microwave Frequency: 9.38 GHz
- Modulation Frequency: 100 kHz
- Modulation Amplitude: 0.4 mT (4 G)
- Temperature: 298 K
- Center Field: 334 mT (3340 G)
- Sweep Range: 8 mT (80 G)

Samples were prepared by filling a double-ended glass capillary tube (1 mm internal diameter) with the appropriate solution, sealing the capillary tube with laboratory film, and then placing the capillary tube in a quartz EPR tube (4 mm internal diameter).

APPENDIX C

SUPPORTING INFORMATION FOR CHAPTER 4

MATERIALS

All chemicals were purchased from Sigma-Aldrich (St. Louis, MO), ThermoFisher Scientific (Pittsburgh, PA), Alfa Aesar (Ward Hill, MA), TCI America (Portland, OR), VWR International (Radnor, PA), and used without further purification.

INSTRUMENTATION

^1H and ^{13}C NMR spectra were obtained using a 600 MHz Bruker Avance NMR spectrometer with residual solvent peaks as a reference for all NMR spectra. ESI-MS were acquired using a Waters M-class UPLC with a RP C4 BEH column for separation and a Waters Synapt G2-Si for detection. Size exclusion chromatography (SEC) was conducted using an Agilent 1100 HPLC with a Phenomenex PolySep-GFC-P Linear 300×7.8 mm column. Isothermal titration calorimetry (ITC) was conducted using a Malvern Microcal iTC200. Transmission electron microscopy (TEM) was conducted using a JEOL JEM-1400Plus transmission electron microscope. Fluorescence data were obtained using a BioTek Synergy H4 Hybrid microplate reader. EPR spectroscopy was performed using a Bruker EMX ER041XG X-band spectrometer with a Bruker ER 4119HS resonator. NMR relaxometry experiments were performed with a 43 MHz Magritek Spinsolve NMR operating with a magnetic field strength of 1 T.

SYNTHESIS

Synthesis of 1-Oxyl-2,2,5,5-tetramethyl-2,5-dihydro-1H-pyrrole-3-carbonitrile (2)

Compound **1** (2.0 g, 10.9 mmol) and pyridine (1.73 g, 21.8 mmol) were added to THF (20 mL) and stirred at 0 °C. TFAA (10 mL) was added slowly added dropwise over 30 min and the reaction mixture was stirred at RT, OVN. The reaction mixture was filtered and the filtrate was collected. The filtrate was diluted with DCM (20 mL), washed with H₂O (2×10 mL), saturated brine (2×10 mL), and dried with MgSO₄. The solvent was removed under reduced pressure to yield the product as an orange solid.

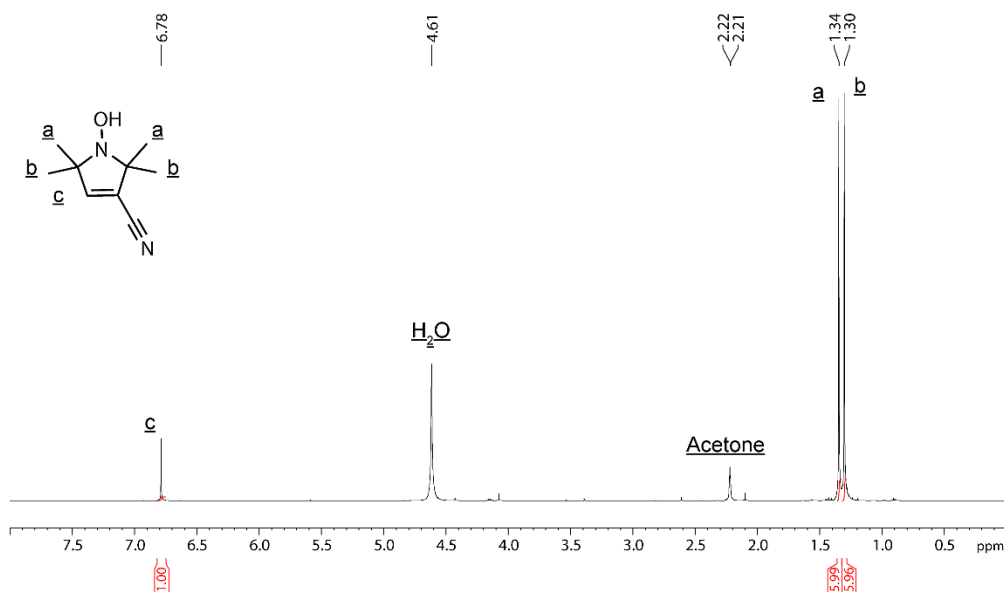


Figure C1. ¹H NMR spectrum of **2**.

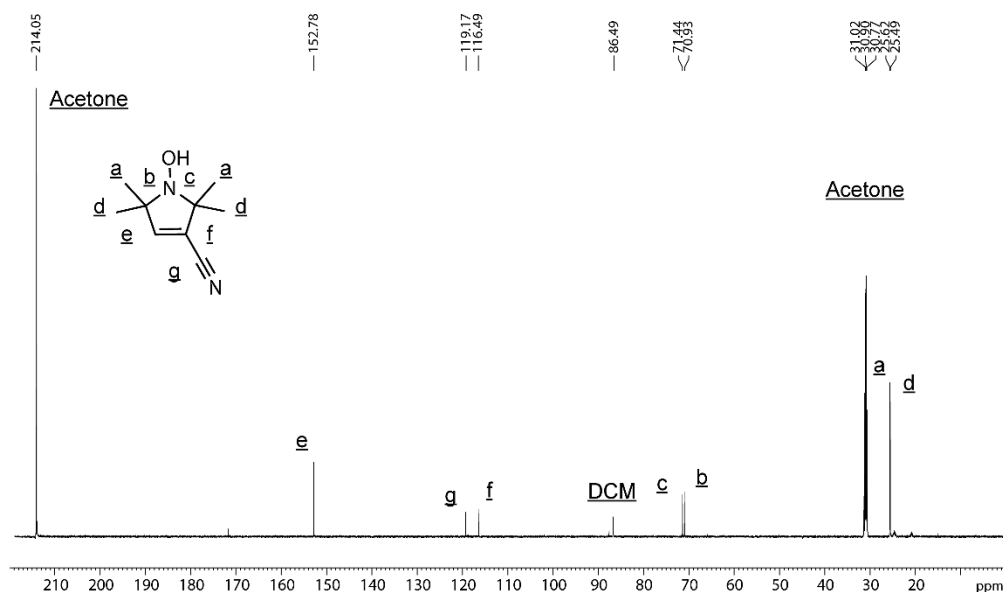


Figure C2. ¹³C NMR spectrum of **2**.

*Synthesis of (3R,4R)-1-Oxyl-2,2,5,5-tetramethylpyrrolidine-3,4-dicarbonitrile (**3**)*

Compound **2** (2.0 g, 12.1 mmol), NaCN (3.0 g, 60.5 mmol), and NH₄Cl (3.2 g, 60.5 mmol) were dissolved in a 75:25 solution of IPA:H₂O (100 mL) and stirred at 80 °C, OVN. Upon cooling, the reaction mixture was saturated with NaCl and extracted with Et₂O (5×100 mL). The solvent was removed under reduced pressure. The crude product was further purified via column chromatography (silica) with Hexanes:EtOAc (100:0 - 75:25). The fractions corresponding to the product were combined and the solvent was removed under reduced pressure to yield the product as an orange solid.

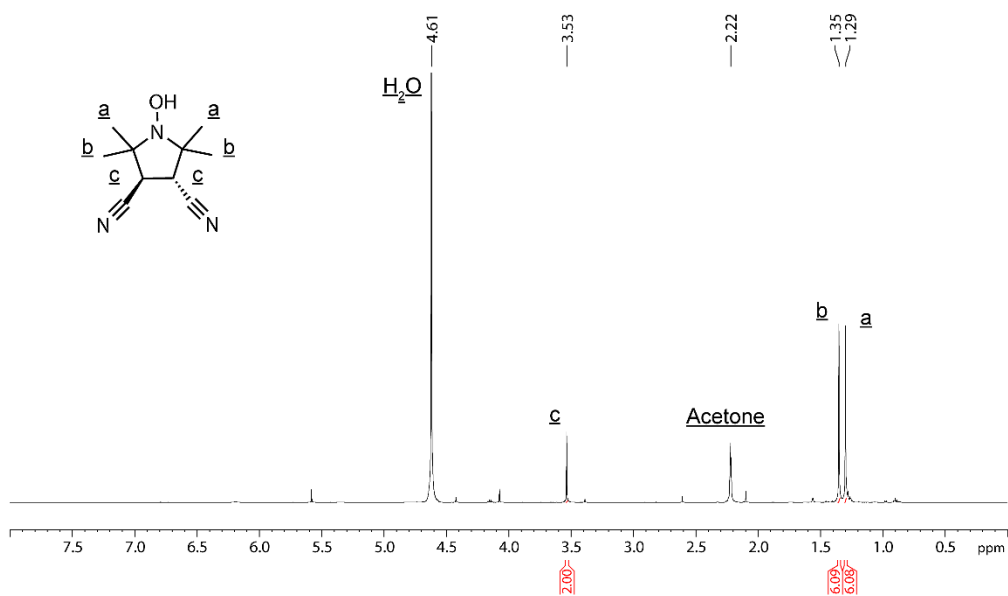


Figure C3. ¹H NMR spectrum of **3**.

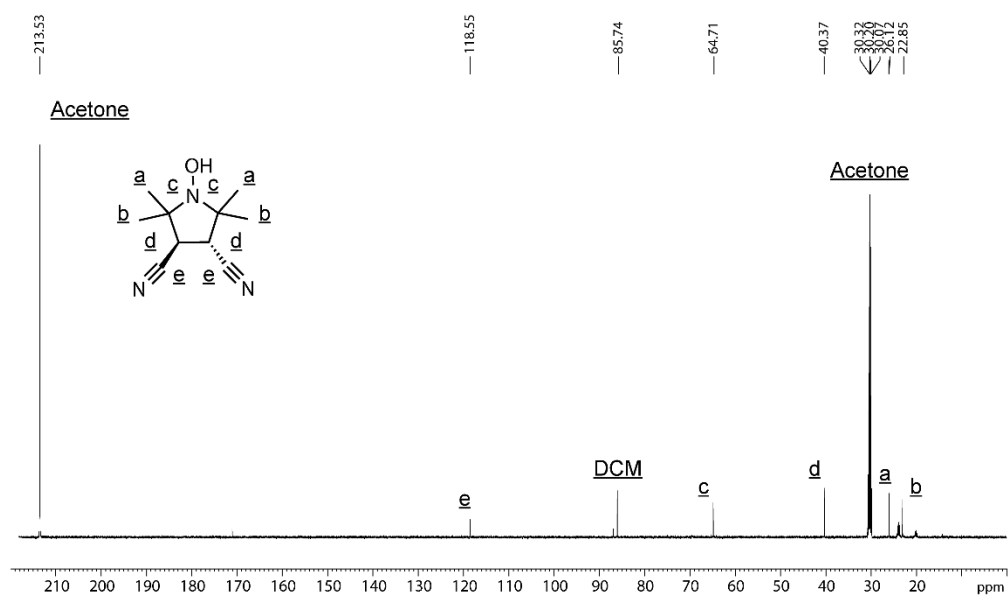


Figure C4. ¹³C NMR spectrum of **3**.

Synthesis of (3R,4R)-1-Oxyl-2,2,5,5-tetramethylpyrrolidine-3,4-dicarboxylic acid (4)

Compound **3** (2.0 g, 10.4 mmol) was stirred in NaOH (aq.) (2 M, 150 mL) at 90 °C, 96 h. The reaction vessel was kept open, and water was added to the reaction solution as needed. Upon cooling the reaction to RT, the reaction mixture was washed with Et₂O (2×100 mL). The organic fractions were combined and discarded. HCl was added until the reaction mixture reached pH 1. The reaction mixture was extracted with Et₂O (5×100 mL). The organic fractions were combined and dried with MgSO₄. The solvent was removed under reduced pressure to yield the product as a pale yellow solid.

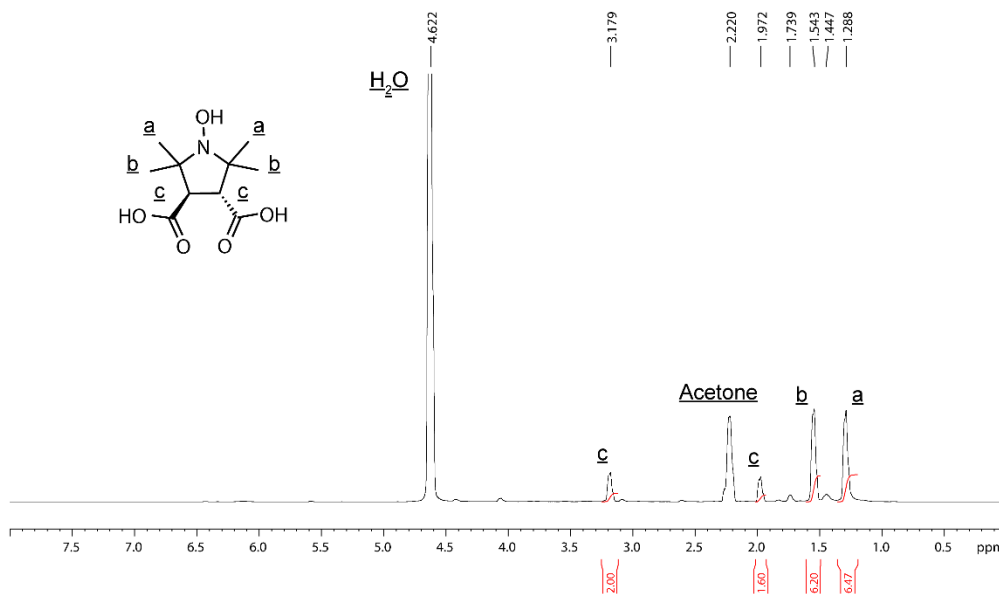


Figure C5. ¹H NMR spectrum of **4**.

Synthesis of (3R,4R)-N³,N⁴-Bis(6-azidohexyl)-1-oxyl-2,2,5,5-tetramethylpyrrolidine-3,4-dicarboxamide (5)

Compound **4** (2 g, 8.7 mmol), 6-azidohexan-1-amine (2.47 g, 17.4 mmol), TEA (1.84 g, 18.2 mmol), HOBT (2.46 g, 18.2 mmol), and DCC (3.76 g, 18.2 mmol) were dissolved in DCM (100 mL) at 0 °C. The resulting solution was stirred at RT, OVN. The solvent was removed under reduced pressure. EtOAc (100 mL) was added to the remaining residue. The reaction mixture was filtered and the filtrate was collected. The filtrate was washed with citric acid (aq.) (4% w/v, 2×30 mL), NaHCO₃ (aq.) (4% w/v, 2×30 mL), and saturated brine (4% w/v, 2×30 mL). The organic fraction was collected and dried with MgSO₄. The solvent was removed under pressure to yield the crude product. The crude product was further purified via column chromatography (silica gel) with DCM:MeOH (100:0 – 90:10). The solvent was removed under pressure to yield the product as a pale yellow liquid.

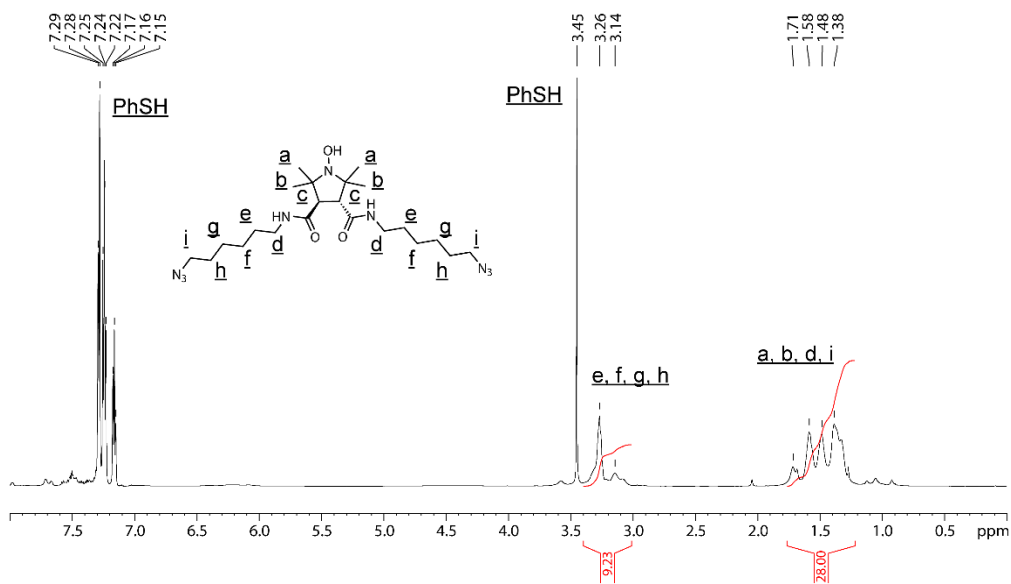


Figure C6. ¹H NMR spectrum of **5**.

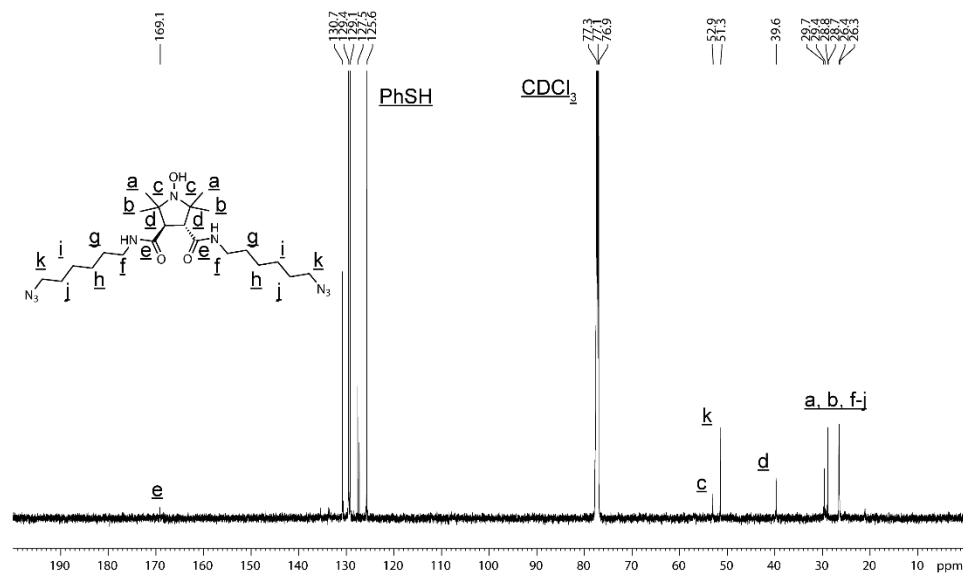


Figure C7. ^{13}C NMR spectrum of **5**.

REFERENCES

1. *Materials Design Inspired by Nature: Function Through Inner Architecture*. Royal Society of Chemistry: Cambridge, 2013.
2. Bengisu, M.; Ferrara, M., *Materials that Move*. Springer International Publishing: Cham, 2018.
3. *Biointerfaces: Where Material Meets Biology*. Royal Society of Chemistry: Cambridge, 2014.
4. Brun, M. J.; Gomez, E. J.; Suh, J., Stimulus-responsive viral vectors for controlled delivery of therapeutics. *J Control Release* **2017**, *267*, 80-89.
5. Roy, D.; Cambre, J. N.; Sumerlin, B. S., Future perspectives and recent advances in stimuli-responsive materials. *Progress in Polymer Science* **2010**, *35*, 278-301.
6. *Electrochromic Smart Materials: Fabrication and Applications*. Royal Society of Chemistry: Cambridge, 2019.
7. *Smart Membranes*. Royal Society of Chemistry: Cambridge, 2019.
8. *Supramolecular Materials for Opto-Electronics*. Royal Society of Chemistry: Cambridge, 2014.
9. *Layered Materials for Energy Storage and Conversion*. Royal Society of Chemistry: Cambridge, 2019.
10. Wei, M.; Gao, Y.; Li, X.; Serpe, M. J., Stimuli-responsive polymers and their applications. *Polymer Chemistry* **2017**, *8*, 127-143.
11. Chen, Z.; Li, N.; Chen, L.; Lee, J.; Gassensmith, J. J., Dual Functionalized Bacteriophage Qbeta as a Photocaged Drug Carrier. *Small* **2016**, *12* (33), 4563-71.
12. Chou, L. Y. T.; Ming, K.; Chan, W. C. W., Strategies for the intracellular delivery of nanoparticles. *Chem. Soc. Rev.* **2011**, *40*, 233-245.
13. Oster, G.; Wang, H., Rotary protein motors. *Trends in Cell Biology* **2003**, *13*, 114-121.
14. Maton, A., *Human biology and health*. Prentice Hall: Englewood Cliffs, N.J., 1993.
15. Meldrum, N. U.; Roughton, F. J. W., Carbonic anhydrase. Its preparation and properties. *The Journal of Physiology* **1933**, *80*, 113-142.

16. Heinemann, H. O.; Goldring, R. M., Bicarbonate and the regulation of ventilation. *The American Journal of Medicine* **1974**, *57*, 361-370.
17. Kato, Y.; Ozawa, S.; Miyamoto, C.; Maehata, Y.; Suzuki, A.; Maeda, T.; Baba, Y., Acidic extracellular microenvironment and cancer. *Cancer Cell International* **2013**, *13*, 89.
18. Wojtkowiak, J. W.; Verduzco, D.; Schramm, K. J.; Gillies, R. J., Drug Resistance and Cellular Adaptation to Tumor Acidic pH Microenvironment. *Molecular Pharmaceutics* **2011**, *8*, 2032-2038.
19. Wojtkowiak, J. W.; Rothberg, J. M.; Kumar, V.; Schramm, K. J.; Haller, E.; Proemsey, J. B.; Lloyd, M. C.; Sloane, B. F.; Gillies, R. J., Chronic Autophagy Is a Cellular Adaptation to Tumor Acidic pH Microenvironments. *Cancer Research* **2012**, *72*, 3938-3947.
20. Hjelmeland, A. B.; Wu, Q.; Heddlestone, J. M.; Choudhary, G. S.; MacSwords, J.; Lathia, J. D.; McLendon, R.; Lindner, D.; Sloan, A.; Rich, J. N., Acidic stress promotes a glioma stem cell phenotype. *Cell Death & Differentiation* **2011**, *18*, 829-840.
21. Li, H.-J.; Du, J.-Z.; Liu, J.; Du, X.-J.; Shen, S.; Zhu, Y.-H.; Wang, X.; Ye, X.; Nie, S.; Wang, J., Smart Superstructures with Ultrahigh pH-Sensitivity for Targeting Acidic Tumor Microenvironment: Instantaneous Size Switching and Improved Tumor Penetration. *ACS Nano* **2016**, *10*, 6753-6761.
22. Du, J.-Z.; Sun, T.-M.; Song, W.-J.; Wu, J.; Wang, J., A Tumor-Acidity-Activated Charge-Conversional Nanogel as an Intelligent Vehicle for Promoted Tumoral-Cell Uptake and Drug Delivery. *Angewandte Chemie International Edition* **2010**, *49*, 3621-3626.
23. Jiang, T.; Zhang, Z.; Zhang, Y.; Lv, H.; Zhou, J.; Li, C.; Hou, L.; Zhang, Q., Dual-functional liposomes based on pH-responsive cell-penetrating peptide and hyaluronic acid for tumor-targeted anticancer drug delivery. *Biomaterials* **2012**, *33*, 9246-9258.
24. Liu, J.; Huang, Y.; Kumar, A.; Tan, A.; Jin, S.; Mozhi, A.; Liang, X.-J., pH-Sensitive nano-systems for drug delivery in cancer therapy. *Biotechnology Advances* **2014**, *32*, 693-710.
25. Liu, J.; Luo, Z.; Zhang, J.; Luo, T.; Zhou, J.; Zhao, X.; Cai, K., Hollow mesoporous silica nanoparticles facilitated drug delivery via cascade pH stimuli in tumor microenvironment for tumor therapy. *Biomaterials* **2016**, *83*, 51-65.
26. Kruse, C. R.; Singh, M.; Targosinski, S.; Sinha, I.; Sorensen, J. A.; Eriksson, E.; Nuutila, K., The effect of pH on cell viability, cell migration, cell proliferation, wound closure, and wound reepithelialization: In vitro and in vivo study. *Wound Repair Regen* **2017**, *25* (2), 260-269.

27. Percival, S. L.; McCarty, S.; Hunt, J. A.; Woods, E. J., The effects of pH on wound healing, biofilms, and antimicrobial efficacy. *Wound Repair Regen* **2014**, *22* (2), 174-86.
28. Gethin, G., The significance of surface pH in chronic wounds. *Wound Healing Science* **2007**, *3* (3), 52-56.
29. Ma, W.; Sung, H. J.; Park, J. Y.; Matoba, S.; Hwang, P. M., A pivotal role for p53: balancing aerobic respiration and glycolysis. *Journal of Bioenergetics and Biomembranes* **2007**, *39*, 243-246.
30. Blake, R. C.; Shute, E. A.; Greenwood, M. M.; Spencer, G. H.; Ingledew, W. J., Enzymes of aerobic respiration on iron. *FEMS Microbiology Reviews* **1993**, *11*, 9-18.
31. Hinkle, P. C., P/O ratios of mitochondrial oxidative phosphorylation. *Biochimica et Biophysica Acta (BBA) - Bioenergetics* **2005**, *1706*, 1-11.
32. Lehnert, N.; Dong, H. T.; Harland, J. B.; Hunt, A. P.; White, C. J., Reversing nitrogen fixation. *Nature Reviews Chemistry* **2018**, *2*, 278-289.
33. Buick, R., When did oxygenic photosynthesis evolve? *Philosophical Transactions of the Royal Society B: Biological Sciences* **2008**, *363*, 2731-2743.
34. Bryant, D. A.; Frigaard, N.-U., Prokaryotic photosynthesis and phototrophy illuminated. *Trends in Microbiology* **2006**, *14*, 488-496.
35. Huang, W.-Y.; Davis, J. J., Multimodality and nanoparticles in medical imaging. *Dalton Transactions* **2011**, *40* (23), 6087.
36. Naik, N.; Braslau, R., Synthesis and applications of optically active nitroxides. *Tetrahedron* **1998**, *54*, 667-696.
37. Barriga, S., 2,2,6,6-Tetramethylpiperidin-1-oxyl (TEMPO). *Synlett* **2001**, *2001*, 0563.
38. Fontmorin, J. M.; Burgos Castillo, R. C.; Tang, W. Z.; Sillanpää, M., Stability of 5,5-dimethyl-1-pyrroline- N -oxide as a spin-trap for quantification of hydroxyl radicals in processes based on Fenton reaction. *Water Research* **2016**, *99*, 24-32.
39. Caravan, P.; Ellison, J. J.; McMurry, T. J.; Lauffer, R. B., Gadolinium(III) Chelates as MRI Contrast Agents: Structure, Dynamics, and Applications. *Chemical Reviews* **1999**, *99*, 2293-2352.
40. Werner, E. J.; Datta, A.; Jocher, C. J.; Raymond, K. N., High-Relaxivity MRI Contrast Agents: Where Coordination Chemistry Meets Medical Imaging. *Angewandte Chemie International Edition* **2008**, *47*, 8568-8580.

41. Garmendia, S.; Mantione, D.; Alonso-de Castro, S.; Jehanno, C.; Lezama, L.; Hedrick, J. L.; Mecerreyes, D.; Salassa, L.; Sardon, H., Polyurethane based organic macromolecular contrast agents (PU-ORCAs) for magnetic resonance imaging. *Polymer Chemistry* **2017**, *8*, 2693-2701.
42. Mauri, E.; Micotti, E.; Rossetti, A.; Melone, L.; Papa, S.; Azzolini, G.; Rimondo, S.; Veglianesi, P.; Punta, C.; Rossi, F.; Sacchetti, A., Microwave-assisted synthesis of TEMPO-labeled hydrogels traceable with MRI. *Soft Matter* **2018**, *14*, 558-565.
43. Sowers, M. A.; McCombs, J. R.; Wang, Y.; Paletta, J. T.; Morton, S. W.; Dreaden, E. C.; Boska, M. D.; Ottaviani, M. F.; Hammond, P. T.; Rajca, A.; Johnson, J. A., Redox-responsive branched-bottlebrush polymers for in vivo MRI and fluorescence imaging. *Nature Communications* **2014**, *5*.
44. Nguyen, H. V.-T.; Chen, Q.; Paletta, J. T.; Harvey, P.; Jiang, Y.; Zhang, H.; Boska, M. D.; Ottaviani, M. F.; Jasanoff, A.; Rajca, A.; Johnson, J. A., Nitroxide-Based Macromolecular Contrast Agents with Unprecedented Transverse Relaxivity and Stability for Magnetic Resonance Imaging of Tumors. *ACS Central Science* **2017**, *3*, 800-811.
45. Warren, J. J.; Mayer, J. M., Tuning of the Thermochemical and Kinetic Properties of Ascorbate by Its Local Environment: Solution Chemistry and Biochemical Implications. *Journal of the American Chemical Society* **2010**, *132*, 7784-7793.
46. Shiga, M.; Miyazono, Y.; Ishiyama, M.; Sasamoto, K.; Ueno, K., 4-Hydroxy-2,2,6,6-tetramethyl-1-piperidinyloxy Free Radical as a Novel Ascorbic Acid Quencher. *Analytical Communications* **1997**, *34*, 115-118.
47. Paletta, J. T.; Pink, M.; Foley, B.; Rajca, S.; Rajca, A., Synthesis and Reduction Kinetics of Sterically Shielded Pyrrolidine Nitroxides. *Organic Letters* **2012**, *14*, 5322-5325.
48. Wang, Y.; Paletta, J. T.; Berg, K.; Reinhart, E.; Rajca, S.; Rajca, A., Synthesis of Unnatural Amino Acids Functionalized with Sterically Shielded Pyrroline Nitroxides. *Organic Letters* **2014**, *16*, 5298-5300.
49. Rajca, A.; Wang, Y.; Boska, M.; Paletta, J. T.; Olankitwanit, A.; Swanson, M. A.; Mitchell, D. G.; Eaton, S. S.; Eaton, G. R.; Rajca, S., Organic Radical Contrast Agents for Magnetic Resonance Imaging. *Journal of the American Chemical Society* **2012**, *134*, 15724-15727.
50. Pokorski, J. K.; Breitenkamp, K.; Liepold, L. O.; Qazi, S.; Finn, M. G., Functional virus-based polymer-protein nanoparticles by atom transfer radical polymerization. *J Am Chem Soc* **2011**, *133* (24), 9242-5.
51. Wen, A. M.; Steinmetz, N. F., Design of Virus-based Nanomaterials for Medicine, Biotechnology, and Energy. *Chem. Soc. Rev.* **2016**, *45* (15), 4074-4126.

52. Chen, Z.; Li, N.; Li, S.; Dharmarwardana, M.; Schlimme, A.; Gassensmith, J. J., Viral chemistry: the chemical functionalization of viral architectures to create new technology. *Wiley Interdisciplinary Reviews: Nanomedicine and Nanobiotechnology* **2016**, 8, 512-534.
53. Yildiz, I.; Shukla, S.; Steinmetz, N. F., Applications of Viral Nanoparticles in Medicine. *Curr. Opin. Biotechnol.* **2011**, 22 (6), 901–908.
54. Koudelka, K. J.; Pitek, A. S.; Manchester, M.; Steinmetz, N. F., Virus-Based Nanoparticles as Versatile Nanomachines. *Annu. Rev. Virol.* **2015**, 2 (1), 379–401.
55. Lee, K. L., Shukla, S., Wu, M., Ayat, N. R., El Sanadi, C. E., Wen, A. M., Edelbrock, J. F., Pokorski, J. K., Commandeur, U., Dubyak, G. R., Steinmetz, N. F., Stealth Filaments: Polymer Chain Length and Conformation Affect the in vivo Fate of PEGylated Potato Virus X. *Acta Biomater.* **2015**, 19, 166–179.
56. Longmire, M.; Choyke, P. L.; Kobayashi, H., Clearance Properties of Nano-sized Particles and Molecules as Imaging Agents: Considerations and Caveats. *Nanomedicine* **2008**, 3 (5), 703-717.
57. Zeltins, A., Construction and Characterization of Virus-Like Particles: A Review. *Mol. Biotechnol.* **2013**, 53 (1), 92–107.
58. Grayson, E. J., Bernardes, G. J. L., Chalker, J. M., Boutureira, O., Koeppe, J. R., Davis, B. G., A Coordinated Synthesis and Conjugation Strategy for the Preparation of Homogeneous Glycoconjugate Vaccine Candidates. *Angew. Chem. Int. Ed.* **2011**, 50 (18), 4127-4132.
59. Jin, A. J.; Mertz, D.; Liao, H.-S.; Johri, A.; Torres, L.; Wu, Y.; Narum, D., Quantifying Nanoscale Properties of Engineered Virus Capsids for Malaria Vaccines. *Biophysical Journal* **2016**, 110 (3).
60. Golmohammadi, R., Fridborg, K., Bundule, M., Valegård, K., Liljas, L., The crystal structure of bacteriophage Q β at 3.5 Å resolution. *Structure* **1996**, 4 (5), 543-554.
61. Scholthof, K.-B. G.; Adkins, S.; Czosnek, H.; Palukaitis, P.; Jacquot, E.; Hohn, T.; Hohn, B.; Saunders, K.; Candresse, T.; Ahlquist, P.; Hemenway, C.; Foster, G. D., Top 10 plant viruses in molecular plant pathology: Top 10 plant viruses. *Molecular Plant Pathology* **2011**, 12, 938-954.
62. Harrison, B. D.; Wilson, T. M. A., Milestones in research on tobacco mosaic virus. *Philosophical Transactions of the Royal Society of London. Series B: Biological Sciences* **1999**, 354, 521-529.

63. Klug, A., The tobacco mosaic virus particle: structure and assembly. *Philosophical Transactions of the Royal Society of London. Series B: Biological Sciences* **1999**, 354, 531-535.
64. Sitasuwan, P.; Lee, L. A.; Li, K.; Nguyen, H. G.; Wang, Q., RGD-conjugated rod-like viral nanoparticles on 2D scaffold improve bone differentiation of mesenchymal stem cells. *Frontiers in Chemistry* **2014**, 2.
65. Schlick, T. L.; Ding, Z.; Kovacs, E. W.; Francis, M. B., Dual-Surface Modification of the Tobacco Mosaic Virus. *Journal of the American Chemical Society* **2005**, 127, 3718-3723.
66. Li, S.; Dharmarwardana, M.; Welch, R. P.; Ren, Y.; Thompson, C. M.; Smaldone, R. A.; Gassensmith, J. J., Template-Directed Synthesis of Porous and Protective Core-Shell Bionanoparticles. *Angew Chem Int Ed Engl* **2016**, 55 (36), 10691-6.
67. Li, S.; Dharmarwardana, M.; Welch, R. P.; Benjamin, C. E.; Shamir, A. M.; Nielsen, S. O.; Gassensmith, J. J., Investigation of Controlled Growth of Metal–Organic Frameworks on Anisotropic Virus Particles. *ACS Applied Materials & Interfaces* **2018**, 10, 18161-18169.
68. Elsabahy, M.; Wooley, K. L., Nanoparticles for Biomedical Delivery Applications. *Chem. Soc. Rev.* **2012**, 41 (7), 2545–2561.
69. Yoon, H. Y.; Jeon, S.; You, D. G.; Park, J. H.; Kwon, I. C.; Koo, H.; Kim, K., Inorganic Nanoparticles for Image-Guided Therapy. *Bioconjugate Chem.* **2017**, 28 (1), 124–134.
70. Zhang, N.; Zhao, F.; Zou, Q.; Li, Y.; Ma, G.; Yan, X., Multitriggered Tumor-Responsive Drug Delivery Vehicles Based on Protein and Polypeptide Coassembly for Enhanced Photodynamic Tumor Ablation. *Small* **2016**, 12 (43), 5936–5943.
71. Abbas, M.; Zou, Q.; Li, S.; Yan, X., Self-Assembled Peptide- and Protein-Based Nanomaterials for Antitumor Photodynamic and Photothermal Therapy. *Adv. Mater.* **2017**, 29 (12), 1605021.
72. Li, X., Che, Z., Mazhar, K., Price, T. J., Qin, Z., Ultrafast Near-Infrared Light-Triggered Intracellular Uncaging to Probe Cell Signaling. *Adv. Funct. Mater.* **2017**, 27 (11), 1605778.
73. Salatin, S.; Maleki Dizaj, S.; Yari Khosroushahi, A., Effect of the surface modification, size, and shape on cellular uptake of nanoparticles. *Cell Biol Int* **2015**, 39 (8), 881-90.
74. Frohlich, E., The role of surface charge in cellular uptake and cytotoxicity of medical nanoparticles. *International Journal of Nanomedicine* **2012**, 7, 5577-91.
75. Blanco, E.; Shen, H.; Ferrari, M., Principles of nanoparticle design for overcoming biological barriers to drug delivery. *Nature Biotechnology* **2015**, 33 (9), 941–951.

76. Walkey, C. D.; Olsen, J. B.; Guo, H.; Emili, A.; Chan, W. C., Nanoparticle size and surface chemistry determine serum protein adsorption and macrophage uptake. *J Am Chem Soc* **2012**, *134* (4), 2139-47.
77. Lesniak, A.; Salvati, A.; Santos-Martinez, M. J.; Radomski, M. W.; Dawson, K. A.; Aberg, C., Nanoparticle adhesion to the cell membrane and its effect on nanoparticle uptake efficiency. *J Am Chem Soc* **2013**, *135* (4), 1438-44.
78. He, C.; Hu, Y.; Yin, L.; Tang, C.; Yin, C., Effects of particle size and surface charge on cellular uptake and biodistribution of polymeric nanoparticles. *Biomaterials* **2010**, *31* (13), 3657-66.
79. Cheng, X.; Tian, X.; Wu, A.; Li, J.; Tian, J.; Chong, Y.; Chai, Z.; Zhao, Y.; Chen, C.; Ge, C., Protein Corona Influences Cellular Uptake of Gold Nanoparticles by Phagocytic and Nonphagocytic Cells in a Size-Dependent Manner. *ACS Appl Mater Interfaces* **2015**, *7* (37), 20568-75.
80. Sanchez-Moreno, P.; Buzon, P.; Boulaiz, H.; Peula-Garcia, J. M.; Ortega-Vinuesa, J. L.; Luque, I.; Salvati, A.; Marchal, J. A., Balancing the effect of corona on therapeutic efficacy and macrophage uptake of lipid nanocapsules. *Biomaterials* **2015**, *61*, 266-278.
81. Key, J.; Palange, A. L.; Gentile, F.; Aryal, S.; Stigliano, C.; Mascolo, D. D.; Rosa, E. D.; Cho, M.; Lee, Y.; Singh, J.; Decuzzi, P., Soft Discoidal Polymeric Nanoconstructs Resist Macrophage Uptake and Enhance Vascular Targeting in Tumors. *ACS Nano* **2015**, *9* (12), 11628–11641.
82. Orellana-Tavra, C.; Haddad, S.; Marshall, R. J.; Lazaro, I. A.; Boix, G.; Imaz, I.; Maspoch, D.; Forgan, R. S.; Fairen-Jimenez, D., Tuning the Endocytosis Mechanism of Zr-Based Metal–Organic Frameworks through Linker Functionalization. *ACS Appl. Mater. Interfaces* **2017**, *9* (41), 35516–35525.
83. Nel, A. E.; Madler, L.; Velegol, D.; Xia, T.; Hoek, E. M.; Somasundaran, P.; Klaessig, F.; Castranova, V.; Thompson, M., Understanding biophysicochemical interactions at the nano-bio interface. *Nat Mater* **2009**, *8* (7), 543-57.
84. Lee, C. H.; Cheng, S. H.; Huang, I. P.; Souris, J. S.; Yang, C. S.; Mou, C. Y.; Lo, L. W., Intracellular pH-responsive mesoporous silica nanoparticles for the controlled release of anticancer chemotherapeutics. *Angew Chem Int Ed Engl* **2010**, *49* (44), 8214-9.
85. Zhang, F.; Correia, A.; Makila, E.; Li, W.; Salonen, J.; Hirvonen, J. J.; Zhang, H.; Santos, H. A., Receptor-Mediated Surface Charge Inversion Platform Based on Porous Silicon Nanoparticles for Efficient Cancer Cell Recognition and Combination Therapy. *ACS Appl Mater Interfaces* **2017**, *9* (11), 10034-10046.

86. Mosquera, J.; Henriksen-Lacey, M.; Garcia, I.; Martinez-Calvo, M.; Rodriguez, J.; Mascarenas, J. L.; Liz-Marzan, L. M., Cellular Uptake of Gold Nanoparticles Triggered by Host-Guest Interactions. *J Am Chem Soc* **2018**.
87. Dempsey, C.; Lee, I.; Cowan, K. R.; Suh, J., Coating barium titanate nanoparticles with polyethylenimine improves cellular uptake and allows for coupled imaging and gene delivery. *Colloids and Surfaces B: Biointerfaces* **2013**, *112*, 108-112.
88. Suk, J. S., Suh, J., Choy, K., Lai, S. K., Fu, J., Hanes, J., Gene delivery to differentiated neurotypic cells with RGD and HIV Tat peptide functionalized polymeric nanoparticles. *Biomaterials* **2006**, *27* (29), 5143-5150.
89. Yue, Z.-G.; Wei, W.; Lv, P.-P.; Yue, H.; Wang, L.-Y.; Su, Z.-G.; Ma, G.-H., Surface Charge Affects Cellular Uptake and Intracellular Trafficking of Chitosan-Based Nanoparticles. *Biomacromolecules* **2011**, *12* (7), 2440-2446.
90. Corpe, W. A., Attachment of Marine Bacteria to Solid Surfaces. In *Adhesion in Biological Systems*, Manly, R., Ed. Academic Press: New York, 1970.
91. Brown, M. S.; Basu, S. K.; Falck, J. R.; Ho, Y. K.; Goldstein, J. L., The scavenger cell pathway for lipoprotein degradation: Specificity of the binding site that mediates the uptake of negatively-charged LDL by macrophages. *Journal of Cellular Biochemistry* **1980**, *13* (1), 67-81.
92. Gustafson, H. H., Holt-Casper, D., Grainger, D. W., Ghandehari, H., Nanoparticle uptake: The phagocyte problem. *Nano Today* **2015**, *10* (4), 487-510.
93. Salis, A.; Fanti, M.; Medda, L.; Nairi, V.; Cugia, F.; Piludu, M.; Sogos, V.; Monduzzi, M., Mesoporous Silica Nanoparticles Functionalized with Hyaluronic Acid and Chitosan Biopolymers. Effect of Functionalization on Cell Internalization. *ACS Biomaterials Science & Engineering* **2016**, *2* (5), 741-751.
94. Chen, Z., Li, N., Li, S., Dharmarwardana, M., Schlimme, A., Gassensmith, J. J., Viral Chemistry: The Chemical Functionalization of Viral Architectures to Create New Technology. *WIREs Nanomed. Nanobiotechnol.* **2016**, *8* (4), 512–534.
95. Rhee, J.-K.; Hovlid, M.; Fiedler, J. D.; Brown, S. D.; Manzenrieder, F.; Kitagishi, H.; Nycholat, C.; Paulson, J., C.; Finn, M. G., Colorful Virus-Like Particles: Fluorescent Protein Packaging by the Q β Capsid. *Biomacromolecules* **2011**, *12* (11), 3977-3981.
96. Mayumi Sato, K. S., Akiyoshi Hiragun, Functional studies of newly synthesized benzoic acid derivatives: Identification of highly potent retinoid-like activity. *Journal of Cellular Physiology* **1988**, *135* (2), 179-188.

97. Xu, C.; Tian, H.; Sun, H.; Jiao, Z.; Zhang, Y.; Chen, X., A pH sensitive co-delivery system of siRNA and doxorubicin for pulmonary administration to B16F10 metastatic lung cancer. *RSC Advances* **2015**, 5 (125), 103380-103385.
98. Kalia, J.; Raines, R. T., Hydrolytic stability of hydrazones and oximes. *Angew Chem Int Ed Engl* **2008**, 47 (39), 7523-6.
99. Wallat, J. D.; Harrison, J. K.; Pokorski, J. K., pH Responsive Doxorubicin Delivery by Fluorous Polymers for Cancer Treatment. *Mol Pharm* **2018**.
100. Jończyk, E.; Kłak, M.; Międzybrodzki, R.; Górski, A., The influence of external factors on bacteriophages—review. *Folia Microbiol* **2011**, 56 (3), 191-200.
101. Sato, D.; Kato, T., Novel fluorescent substrates for detection of trypsin activity and inhibitor screening by self-quenching. *Bioorg Med Chem Lett* **2016**, 26 (23), 5736-5740.
102. Munkholm, C.; Parkinson, D. R.; Walt, D. R., Intramolecular Fluorescence Self-Quenching of Fluoresceinamine. *J Am Chem Soc* **1990**, 112 (7), 2608-2612.
103. Olsson, M.; Nilsson, A.; Oldenborg, P. A., Dose-dependent inhibitory effect of CD47 in macrophage uptake of IgG-opsonized murine erythrocytes. *Biochem Biophys Res Commun* **2007**, 352 (1), 193-7.
104. Okazawa, H.; Motegi, S.; Ohyama, N.; Ohnishi, H.; Tomizawa, T.; Kaneko, Y.; Oldenborg, P. A.; Ishikawa, O.; Matozaki, T., Negative regulation of phagocytosis in macrophages by the CD47-SHPS-1 system. *J. Immunol.* **2005**, 174 (4), 2004-11.
105. Caravan, P., Strategies for increasing the sensitivity of gadolinium based MRI contrast agents. *Chemical Society Reviews* **2006**, 35, 512.
106. Corr, S. A.; Byrne, S. J.; Tekoriute, R.; Meledandri, C. J.; Brougham, D. F.; Lynch, M.; Kerskens, C.; O'Dwyer, L.; Gun'ko, Y. K., Linear Assemblies of Magnetic Nanoparticles as MRI Contrast Agents. *Journal of the American Chemical Society* **2008**, 130, 4214-4215.
107. Davies, G.-L.; Corr, S. A.; Meledandri, C. J.; Briode, L.; Brougham, D. F.; Gun'ko, Y. K., NMR Relaxation of Water in Nanostructures: Analysis of Ferromagnetic Cobalt-Ferrite Polyelectrolyte Nanocomposites. *ChemPhysChem* **2011**, 12, 772-776.
108. Hermann, P.; Kotek, J.; Kubicek, V.; Lukes, I., Gadolinium(iii) complexes as MRI contrast agents: ligand design and properties of the complexes. *Dalton Transactions* **2008**, 3027.
109. Zhou, Z.; Lu, Z.-R., Gadolinium-based contrast agents for magnetic resonance cancer imaging. *Wiley Interdisciplinary Reviews: Nanomedicine and Nanobiotechnology* **2012**, 5, 1-18.

110. Li, Y.; Beija, M.; Laurent, S.; Elst, L. v.; Muller, R. N.; Duong, H. T. T.; Lowe, A. B.; Davis, T. P.; Boyer, C., Macromolecular Ligands for Gadolinium MRI Contrast Agents. *Macromolecules* **2012**, *45*, 4196-4204.
111. Davies, G.-L.; Kramberger, I.; Davis, J. J., Environmentally responsive MRI contrast agents. *Chemical Communications* **2013**, *49*, 9704.
112. Mendichovszky, I. A.; Marks, S. D.; Simcock, C. M.; Olsen, O. E., Gadolinium and nephrogenic systemic fibrosis: time to tighten practice. *Pediatric Radiology* **2007**, *38*, 489-496.
113. Shellock, F. G.; Kanal, E., Safety of magnetic resonance imaging contrast agents. *Journal of Magnetic Resonance Imaging* **1999**, *10*, 477-484.
114. Swaminathan, S.; Horn, T. D.; Pellowski, D.; Abul-Ezz, S.; Bornhorst, J. A.; Viswamitra, S.; Shah, S. V., Nephrogenic Systemic Fibrosis, Gadolinium, and Iron Mobilization. *New England Journal of Medicine* **2007**, *357*, 720-722.
115. Shin, T.-H.; Choi, Y.; Kim, S.; Cheon, J., Recent advances in magnetic nanoparticle-based multi-modal imaging. *Chemical Society Reviews* **2015**, *44*, 4501-4516.
116. Verwilt, P.; Park, S.; Yoon, B.; Kim, J. S., Recent advances in Gd-chelate based bimodal optical/MRI contrast agents. *Chemical Society Reviews* **2015**, *44*, 1791-1806.
117. Terreno, E.; Castelli, D. D.; Viale, A.; Aime, S., Challenges for Molecular Magnetic Resonance Imaging. *Chemical Reviews* **2010**, *110*, 3019-3042.
118. Glunde, K.; Artemov, D.; Penet, M.-F.; Jacobs, M. A.; Bhujwala, Z. M., Magnetic Resonance Spectroscopy in Metabolic and Molecular Imaging and Diagnosis of Cancer. *Chemical Reviews* **2010**, *110*, 3043-3059.
119. Smith, B. R.; Gambhir, S. S., Nanomaterials for In Vivo Imaging. *Chemical Reviews* **2017**, *117*, 901-986.
120. Harvey, P.; Kuprov, I.; Parker, D., Lanthanide Complexes as Paramagnetic Probes for ^{19}F Magnetic Resonance. *European Journal of Inorganic Chemistry* **2012**, *2012*, 2015-2022.
121. Boase, N. R. B.; Blakey, I.; Thurecht, K. J., Molecular imaging with polymers. *Polymer Chemistry* **2012**, *3*, 1384.
122. Tirotta, I.; Dichiarante, V.; Pigliacelli, C.; Cavallo, G.; Terraneo, G.; Bombelli, F. B.; Metrangolo, P.; Resnati, G., ^{19}F Magnetic Resonance Imaging (MRI): From Design of Materials to Clinical Applications. *Chemical Reviews* **2015**, *115*, 1106-1129.

123. Aime, S.; Castelli, D. D.; Crich, S. G.; Gianolio, E.; Terreno, E., Pushing the Sensitivity Envelope of Lanthanide-Based Magnetic Resonance Imaging (MRI) Contrast Agents for Molecular Imaging Applications. *Accounts of Chemical Research* **2009**, *42*, 822-831.
124. Liu, G.; Song, X.; Chan, K. W. Y.; McMahon, M. T., Nuts and bolts of chemical exchange saturation transfer MRI: REVIEW OF CEST IMAGING. *NMR in Biomedicine* **2013**, *26*, 810-828.
125. Dharmarwardana, M.; Martins, A. F.; Chen, Z.; Palacios, P. M.; Nowak, C. M.; Welch, R. P.; Li, S.; Luzuriaga, M. A.; Bleris, L.; Pierce, B. S.; Sherry, A. D.; Gassensmith, J. J., Nitroxyl Modified Tobacco Mosaic Virus as a Metal-Free High-Relaxivity MRI and EPR Active Superoxide Sensor. *Molecular Pharmaceutics* **2018**, *15*, 2973-2983.
126. Anderson, E. A.; Isaacman, S.; Peabody, D. S.; Wang, E. Y.; Canary, J. W.; Kirshenbaum, K., Viral Nanoparticles Donning a Paramagnetic Coat: Conjugation of MRI Contrast Agents to the MS2 Capsid. *Nano Letters* **2006**, *6*, 1160-1164.
127. Datta, A.; Hooker, J. M.; Botta, M.; Francis, M. B.; Aime, S.; Raymond, K. N., High Relaxivity Gadolinium Hydroxypyridonate–Viral Capsid Conjugates: Nanosized MRI Contrast Agents. *Journal of the American Chemical Society* **2008**, *130*, 2546-2552.
128. Bruckman, M. A.; Randolph, L. N.; Gulati, N. M.; Stewart, P. L.; Steinmetz, N. F., Silica-coated Gd(DOTA)-loaded protein nanoparticles enable magnetic resonance imaging of macrophages. *Journal of Materials Chemistry B* **2015**, *3*, 7503-7510.
129. Bye, N.; Hutt, O. E.; Hinton, T. M.; Acharya, D. P.; Waddington, L. J.; Moffat, B. A.; Wright, D. K.; Wang, H. X.; Mulet, X.; Muir, B. W., Nitroxide-Loaded Hexosomes Provide MRI Contrast in Vivo. *Langmuir* **2014**, *30*, 8898-8906.
130. Hu, H.; Zhang, Y.; Shukla, S.; Gu, Y.; Yu, X.; Steinmetz, N. F., Dysprosium-Modified Tobacco Mosaic Virus Nanoparticles for Ultra-High-Field Magnetic Resonance and Near-Infrared Fluorescence Imaging of Prostate Cancer. *ACS Nano* **2017**, *11*, 9249-9258.
131. Bruckman, M. A.; Hern, S.; Jiang, K.; Flask, C. A.; Yu, X.; Steinmetz, N. F., Tobacco mosaic virus rods and spheres as supramolecular high-relaxivity MRI contrast agents. *Journal of Materials Chemistry B* **2013**, *1*, 1482.
132. Bruckman, M. A.; Jiang, K.; Simpson, E. J.; Randolph, L. N.; Luyt, L. G.; Yu, X.; Steinmetz, N. F., Dual-Modal Magnetic Resonance and Fluorescence Imaging of Atherosclerotic Plaques in Vivo Using VCAM-1 Targeted Tobacco Mosaic Virus. *Nano Letters* **2014**, *14*, 1551-1558.

133. Prasuhn, J., Duane E.; Yeh, R. M.; Obenaus, A.; Manchester, M.; Finn, M. G., Viral MRI contrast agents: coordination of Gd by native virions and attachment of Gd complexes by azide–alkyne cycloaddition. *Chem. Commun.* **2007**, 1269-1271.
134. Liepold, L.; Anderson, S.; Willits, D.; Oltrogge, L.; Frank, J. A.; Douglas, T.; Young, M., Viral capsids as MRI contrast agents. *Magnetic Resonance in Medicine* **2007**, *58*, 871-879.
135. Garimella, P. D.; Datta, A.; Romanini, D. W.; Raymond, K. N.; Francis, M. B., Multivalent, High-Relaxivity MRI Contrast Agents Using Rigid Cysteine-Reactive Gadolinium Complexes. *Journal of the American Chemical Society* **2011**, *133*, 14704-14709.
136. Hooker, J. M.; Datta, A.; Botta, M.; Raymond, K. N.; Francis, M. B., Magnetic Resonance Contrast Agents from Viral Capsid Shells: A Comparison of Exterior and Interior Cargo Strategies. *Nano Letters* **2007**, *7*, 2207-2210.
137. Raymond, K. N.; Pierre, V. C., Next Generation, High Relaxivity Gadolinium MRI Agents. *Bioconjugate Chemistry* **2005**, *16*, 3-8.
138. Allen, M.; Bulte, J. W. M.; Liepold, L.; Basu, G.; Zywicke, H. A.; Frank, J. A.; Young, M.; Douglas, T., Paramagnetic viral nanoparticles as potential high-relaxivity magnetic resonance contrast agents. *Magnetic Resonance in Medicine* **2005**, *54*, 807-812.
139. Qazi, S.; Liepold, L. O.; Abedin, M. J.; Johnson, B.; Prevelige, P.; Frank, J. A.; Douglas, T., P22 Viral Capsids as Nanocomposite High-Relaxivity MRI Contrast Agents. *Molecular Pharmaceutics* **2013**, *10*, 11-17.
140. Jayaraj, N.; Porel, M.; Ottaviani, M. F.; Maddipatla, M. V. S. N.; Modelli, A.; Da Silva, J. P.; Bhogala, B. R.; Captain, B.; Jockusch, S.; Turro, N. J.; Ramamurthy, V., Self Aggregation of Supramolecules of Nitroxides@Cucurbit[8]uril Revealed by EPR Spectra. *Langmuir* **2009**, *25*, 13820-13832.
141. Mileo, E.; Mezzina, E.; Grepioni, F.; Pedulli, G. F.; Lucarini, M., Preparation and Characterisation of a New Inclusion Compound of Cucurbit[8]uril with a Nitroxide Radical. *Chemistry - A European Journal* **2009**, *15*, 7859-7862.
142. Peresypkina, E. V.; Fedin, V. P.; Maurel, V.; Grand, A.; Rey, P.; Vostrikova, K. E., Inclusion of a Nitronyl Nitroxyl Radical and Its Hydrochloride in Cucurbit[8]uril. *Chemistry – A European Journal* **2010**, *16*, 12481-12487.
143. Rinkevicius, Z.; Frecuş, B.; Murugan, N. A.; Vahtras, O.; Kongsted, J.; Ågren, H., Encapsulation Influence on EPR Parameters of Spin-Labels: 2,2,6,6-Tetramethyl-4-methoxypiperidine-1-oxyl in Cucurbit[8]uril. *Journal of Chemical Theory and Computation* **2012**, *8*, 257-263.

144. Yi, S.; Captain, B.; Ottaviani, M. F.; Kaifer, A. E., Controlling the Extent of Spin Exchange Coupling in 2,2,6,6-Tetramethylpiperidine-1-oxyl (TEMPO) Biradicals via Molecular Recognition with Cucurbit[*n*]uril Hosts. *Langmuir* **2011**, *27*, 5624-5632.
145. Kemp, S.; Wheate, N. J.; Stootman, F. H.; Aldrich-Wright, J. R., The Host-Guest Chemistry of Proflavine with Cucurbit[6,7,8]urils. *Supramolecular Chemistry* **2007**, *19*, 475-484.
146. Dsouza, R. N.; Pischel, U.; Nau, W. M., Fluorescent Dyes and Their Supramolecular Host/Guest Complexes with Macrocycles in Aqueous Solution. *Chemical Reviews* **2011**, *111*, 7941-7980.
147. Xue, M.; Yang, Y.; Chi, X.; Yan, X.; Huang, F., Development of Pseudorotaxanes and Rotaxanes: From Synthesis to Stimuli-Responsive Motions to Applications. *Chemical Reviews* **2015**, *115*, 7398-7501.
148. Vohlřdal, J.; Wilks, E. S.; Yerin, A.; Fradet, A.; Hellwich, K.-H.; Hodge, P.; Kahovec, J.; Mormann, W.; Stepto, R. F. T., Terminology and nomenclature for macromolecular rotaxanes and pseudorotaxanes (IUPAC Recommendations 2012). *Pure and Applied Chemistry* **2012**, *84*, 2135-2165.

BIOGRAPHICAL SKETCH

Hamilton Lee was born in 1993 in Taipei, Taiwan and moved to Richardson, Texas within two weeks. He then moved to Ardmore, Oklahoma in 1996, and to Rio Rancho, New Mexico in 2001. After graduation from Rio Rancho High School in 2011, Hamilton enrolled at Trinity University in San Antonio, Texas. In May 2015, he received a Bachelor of Science in Chemistry. Hamilton then joined the PhD program of the Department of Chemistry and Biochemistry at The University of Texas at Dallas in August 2015.

CURRICULUM VITAE

EDUCATION

Candidate for Doctor of Philosophy in Chemistry (Expected August 2019)

University of Texas at Dallas, Richardson, TX, USA

“Regulating Stimulus Responses of Functional Materials”

Advisor: Professor Jeremiah J. Gassensmith

Bachelor of Science in Chemistry (2015)

Trinity University, San Antonio, TX, USA

“Co-Host Mediated Divalent Recognition of Peptides”

Advisor: Professor Adam R. Urbach

RESEARCH EXPERIENCE

University of Texas at Dallas, Aug 2015 – Present

Department of Chemistry and Biochemistry; Research Advisor: Dr. Jeremiah J. Gassensmith

Synthesis of small molecules; Small molecule purification, isolation, and analysis; Synthesis consultant; Bioconjugation; Protein purification and isolation; Biomaterials preparation and analysis; Characterization of small molecules and biomolecules via chromatography and mass spectrometry; Instrument consultant; Inventory management; Lab accountant

Trinity University, May 2013 – May 2015

Department of Chemistry; Research Advisor: Dr. Adam R. Urbach

Synthesis of peptides and supramolecular complexes; Characterization of peptides and supramolecular complexes via chromatography and mass spectrometry

PEER-REVIEWED PUBLICATIONS

1. **Hamilton Lee**, Candace E. Benjamin, Chance M. Nowak, Lana H. Tuong, Raymond P. Welch, Zhuo Chen, Madushani Dharmarwardana, Kyle W. Murray, Leonidis Bleris, Sheena D’Arcy, Jeremiah J. Gassensmith*, “Regulating the Uptake of Viral Nanoparticles in Macrophage and Cancer Cells via a pH Switch.” *Molecular Pharmaceutics*, **2018**, *15*, 2984-2990.
2. Madushani Dharmarwardana, Bhargav S. Arimilli, Michael A. Luzuriaga, Sunah Kwon, **Hamilton Lee**, Gayan A. Appuhamillage, Gregory T. McCandless, Ronald A. Smaldone, Jeremiah J. Gassensmith*, “The Thermo-Responsive Behavior in Molecular Crystals of Naphthalene Diimides and Their 3D Printed Thermochromic Composites.” *CrystEngComm*, **2018**, *20*, 6054-6060.
3. Raymond P. Welch, **Hamilton Lee**, Michael A. Luzuriaga, Olivia R. Brohlin, Jeremiah J. Gassensmith*, “Protein-Polymer Delivery: Chemistry from the Cold Chain to the Clinic.” *Bioconjugate Chemistry*, **2018**, *29*, 2867-2883.

4. Michael A. Luzuriaga, Candace E. Benjamin, Michael W. Gaertner, **Hamilton Lee**, Fabian C. Herbert, Snipta Mallick, Jeremiah J. Gassensmith*, “ZIF-8 Degrades in Cell Media, Serum, and Some—but not all—Common Laboratory Buffers.” *Supramolecular Chemistry*, **2019**, 1-6.

MEETINGS AND CONFERENCES

1. 26th AIRC Annual Symposium, Dallas, Texas, *Jan. 30, 2019*
2. 51st ACS Regional Meeting, Dallas, Texas, *Apr. 21, 2018*
3. FNANO Annual Meeting, Snowbird, Utah, *Apr. 18, 2018*
4. 249th ACS National Meeting, Denver, Colorado, *Mar. 24, 2015*
5. Gulf Coast Undergraduate Research Symposium, Houston, Texas, *Oct. 25, 2014*
6. 30th Trinity University Department of Chemistry Research Symposium, San Antonio, Texas, *Jul. 24, 2014*
7. 247th ACS National Meeting, Dallas, Texas, *Mar. 17, 2014*
8. Rice University Regional Undergraduate Symposium, Houston, Texas, *Oct. 26, 2013*
9. 29th Trinity University Department of Chemistry Research Symposium, San Antonio, Texas, *Jul. 25, 2013*

AWARDS AND HONORS

1. ACS DFW MiM Best Presentation, Organic Division (2018)
2. Eric Moore Chemistry Graduate Student Scholarship (2016)
3. UTD Graduate Studies Scholarship (2015)
4. Trinity University President’s Academic Scholarship (2011)
5. Imogene and Harold Herndon Endowed Scholarship Fund Award for Studies in Science (2011)

PROFESSIONAL MEMBERSHIPS

American Chemical Society
CompTIA

TECHNICAL PROFICIENCIES

Chemical Methods

Organic synthesis; Bioconjugation; Protein expression, purification, and isolation; Protein assays; Chromatography; Mass spectrometry; Spectroscopy

Instrumentation

Atomic Force Microscopy; Differential Scanning Calorimetry; Electron Paramagnetic Resonance Spectroscopy; Electrospray Ionization Mass Spectroscopy; Fluorescence Spectroscopy; Fourier Transform Infrared Spectroscopy; High Pressure Liquid Chromatography; Matrix-Assisted Laser Desorption Ionization Mass Spectroscopy; Nuclear Magnetic Resonance Spectroscopy; UV-Vis Spectroscopy

Computer Software

Adobe Creative Suite, ChemDraw, Kaleidagraph, Microsoft Office, Microsoft Visual Basic, Origin, MATLAB, Python, Topspin

Computer Certifications

CompTIA A+ Certified Professional IT Technician